Measurements of Two-Proton Correlations in Ultra-Relativistic Heavy-Ion Collisions

A Dissertation Presented

by

Sergei Y. Panitkin

to

The Graduate School

in Partial Fulfillment of the Requirements

for the Degree of

Doctor of Philosophy

in

Physics

State University of New York
at
Stony Brook

May 1997

State University of New York
at Stony Brook

The Graduate School

Sergei Y. Panitkin

We, the dissertation committee for the above candidate for the Doctor of Philosophy degree, hereby recommend acceptance of the dissertation.

Peter Braun-Munzinger (Advisor)
Professor of Physics

Gerald E. Brown (Chair)
Distinguished Professor of Physics

Thomas K. Hemmick
Professor of Physics

Edward O'Brien
Physicist, Brookhaven National Laboratory

This dissertation is accepted by the Graduate School.

Graduate School

Abstract of the Dissertation

Measurements of Two-Proton Correlations in Ultra-Relativistic Heavy-Ion Collisions

by

Sergei Y. Panitkin

Doctor of Philosophy

in

Physics

State University of New York at Stony Brook

1997

Two-proton correlation functions were measured in heavy-ion collisions at AGS BNL. Correlation functions were obtained for Si+Pb collisions at 14.6 AGeV/c and, for the first time, in Au+Au collisions at 10.8 AGeV/c and 11.5 AGeV/c. Also, first measurements of proton-deuteron correlations in Au+Au collisions were performed. Experimental data are compared with calculations based on the cascade model RQMD(1.08) and Koonin-Pratt formalism. The centrality dependence of the correlation function was studied in central Au+Au reactions at 11.5 AGeV/c. First measurements of the dependence of the two-proton correlation function

on the orientation of the proton pair relative to the reaction plane were performed. A statistically significant difference between the correlation functions with and without cuts on the orientation of the pairs relative to the reaction plane was observed. We also found that the two-proton correlation function does not exhibit significant differences when the proton source is viewed from different sides of the reaction plane, a possible indication of the azimuthal symmetry of the source.

To my parents and grand mother.

Contents

List of Figures

List of Tables

Acknowledgements

Well, it's time to look back and say "Thank you" to all the people without whose help and support this thesis would have never happened. There were so many that I am in real danger of missing someone, so I ask your forgiveness for any omissions.

This thesis would have never happened without Lucy Fortson, who I met back in Russia and who "smuggled" my papers to the West (the Iron Curtain stood high then !) and showed them to Gerry Brown. Luckily, Gerry didn't throw my papers in the garbage can and decided to give them to my future boss - Peter Braun-Munzinger. And, as if he didn't have any other problems, Peter decided to become my advisor. Only due to his patience and support was I able to stay at Stony Brook and, quite possibly, in physics at all. He introduced me to the exciting field of relativistic heavy ion collisions and provided much needed advise and encouragement for this work.

The Stony Brook Relativistic Heavy Ion Group was an exiting, ever changing and stimulating environment in which to work. Professors Johanna Stachel and Tom Hemmick were examples of professionalism and undying enthusiasm for physics; I have learned a great deal from both of them. Johanna was demanding but fair. Her utmost attention to details, without loosing a general view of a problem, impressed me from the beginning. Tom is one of the finest experimentalists I've ever met and a great teacher. Many times during writing this thesis I wished I had his ability to explain apparently complicated phenomena in a simple and clear way.

The postdocs of the RHIC group I had a privilege to work with, Nu Xu, Hannes Wessels, Sergei Sedykh, Dariusz Miskowiec and Martin Trzaska, have all worked tirelessly and deserve special thanks. Each of them, in his own way, has enhanced and sometimes changed my understanding of experimental nuclear physics.

From the start I have been impressed with the quality and enthusiasm of the Stony Brook students. The atmosphere of friendship and mutual support was a hallmark of the group. Bill Llope, Gabor David, Moorthy Muthuswami, Jimmy Dee, Yingchao Zhang, Byungsik Hong, Chuanming Zou, Rich Bersch, Youngil Kwon, Tim Piazza, Mark Pollack, Steve Johnson, Thongbay Vongpaseuth - they were the most worthy team to work with. All contributed, in one way or another, to this thesis. It's been a pleasure to work with them and most of the time it was fun too.

Steve and Thongbay shouldered the burden of proofreading my thesis and they have my special thanks.

The experiment wouldn't have been such a success without the hard work of the whole E814/E877 Collaboration. I owe my gratitude to the entire Collaboration and consider it my privilege to have been a part this effort.

I would like to express my gratitude to the theorists Dr. Richard Lednicky, Dr. Raffaele Mattiello, Prof. Scott Pratt and Dr. Heinz Sorge, who kindly permitted the use of their codes in my analysis and help with advise. Enlightening discussions with Prof. Sergei Voloshin are also gratefully acknowledged.

I am forever indebted to my parents Yuri and Zinaida for their constant support and motivation. I dedicate this thesis to them.

Chapter 1

Introduction

1.1 Physics of Heavy-Ion Collisions

Relativistic Heavy-Ion Collisions (RHIC) provide physicists with a unique opportunity to study matter under extreme conditions. The principal motivations to use high-energy heavy-ion collisions are to explore the transition from hadronic to quark-gluon degrees of freedom, the order of such a transition and the nature of quark confinement. It is expected that during the collision a region of hot and dense hadronic matter is formed [1]. In this region individual hadrons are likely to lose their identity and, for a period of time, form a new state of matter - the Quark Gluon Plasma (QGP). The properties or even the order of such transition are not well understood yet. It is not clear which experimentally measurable observables can serve as an unambiguous signal of the QGP creation; many QGP signatures have been suggested. So far, despite all efforts, most[1] of the QGP searches yielded a negative or ambiguous results [2]. The observed effects can be explained by conventional hadron scenarios. Most likely this implies that the phase transition is not reached at currently accessible energies in present day laboratories (see Table 1.1 for a list of existing and future experimental facilities involved in the relativistic heavy-ion research). The study of the QGP may require new, more powerful accelerators and more sophisticated detectors. Such projects are currently under construction [3].

What has become clear, after years of experiments, is that the horizon of relativistic heavy-ion physics is much broader than previously expected. The spectrum of the scientific possibilities and applications is significantly richer than was initially expected. Even at densities and temperatures less than that required for a phase transition, many exotic and exciting phenomena have been predicted to occur.

By varying beam energies one can probe the nuclear matter equation of state at different temperatures and densities.

Properties of the vacuum and the existence of chirality restoration can be investigated using RHIC.

Baryon density dependent effects [4], like particle mass shifts, can be studied in the laboratory only by using heavy ion collisions.

---

[1] Data on J/ψ and ψ' suppression relative to Drell-Yan continuum reported by NA50 collaboration and the shape of the low mass dilepton spectrum measured by CERES/NA45 are currently notable exceptions and the jury is still out.

Table 1.1: The machines of the relativistic heavy ion physics.

Accelerator	Laboratory	Heaviest Beam	Momentum ($A \cdot GeV/c$)	Available
SIS	GSI	^{197}Au	1	1982
BEVALAC	LBL	^{57}La	2.1	1982
AGS	BNL	^{28}Si	14.6	1986
		^{197}Au	11.5	1992
SPS	CERN	^{32}S	200	1986
		^{208}Pb	160	1994
RHIC	BNL	^{197}Au	100×100	1999
LHC	CERN	^{208}Pb	3150×3150	~ 2005

Properties of the hadronization processes or transition from the quark-gluon to hadron degrees of freedom still remain unclear and can be studied using RHIC.

Heavy-ion collisions allow us to take a peek at the conditions and processes which most likely occured only in the early Universe, a few microseconds after the 'Big Bang'.

Unusual, under normal Earth conditions, forms of matter such as strangelets are thought to be created in high-energy collisions as well as strange dibaryons.

These are only a few examples; for recent reviews of the experimental and theoretical situation in relativistic-heavy ion collisions see References [5, 6].

1.2 Intensity Interferometry

One of the predicted signatures of QGP formation is an anomalously large production of entropy in the collision, resulting from a phase transition of hadrons to quark-gluon degrees of freedom, leading to a long lived fireball. Such a source can manifest itself in the shape of measured two-particle correlation functions. Measurements of the two-particle small relative momentum correlations [7, 8] are widely used in relativistic heavy-ion physics as a tool for extracting information about the spatial and temporal extent of the system at freeze-out. The complexity of heavy-ion reactions demands utilization of different particles as probes of the reaction zone in order to obtain a reliable picture of the collision. Most of the published experimental data are measurements using two-meson (π or K) [9, 10, 11, 12, 13, 14, 15] correlation functions. Information concerning baryon freeze-out configurations is far more sparse. Several methods have been suggested to address this problem: two-proton interferometry [23, 24], analysis of the deuteron to proton yield ratios [25] and deuteron-proton interferometry [26, 27]. In this thesis we present measurements, made by the E814/E877 collaboration at the BNL AGS, of two-proton correlation functions in Si+Pb 14.6 AGeV/c and Au+Au 10.8 AGeV/c collisions. The results of the two-pion correlation analysis for these systems were published in [13, 28, 29, 30].

Two-proton correlations are due to the attractive strong and repulsive Coulomb final state interactions. Coulomb repulsion, together with the quantum mechanical requirement of antisymmetrization of the pair wave function, decreases the probability of detection of pairs with relative momenta close to zero; on the other the hand, the strong interaction increases such probability. The interplay of these effects leads to a characteristic "dip+bump" shape of the correlation function. Thus the interpretation of the proton correlation data necessarily involves calculations of the final state interactions. The height of the peak of the correlation function can be related to the space-time parameters of the emitting source. It has been shown [23, 24] that, for simple static sources, it scales approximately inversely proportional to the source volume. However, in heavy-ion collisions, a direct determination of the source parameters from the proton correlation function is far from straightforward. The existence of collective effects [13, 31, 32], which lead to dynamical correlations between the momentum and position of the emitted hadrons , may create a situation in which the correlation function does not reflect the actual size of the source [13, 33]. Under these conditions using a static source model [34] to generate the correlation and extract source parameters can be misleading. It seems to be necessary to utilize approaches such as hydro-dynamical or transport models, which are constructed to describe collective effects, for the interpretation of the proton correlation functions. In order to obtain information on source parameters from the measured proton correlation functions, a transport model was used in the analysis.

In the next chapter we will discuss the theoretical background involved in the two-proton correlation analysis. Only in order to illustrate the sensitivity of the correlation function to the source parameters will we utilize the static model.

1.3 Organization of the Thesis

In this work we present our analysis of two-proton correlation functions measured in Si+Pb collisions and Au+Au collisions. Also, measurements of the proton-deuteron correlation function in Au+Au collisions are presented. The analysis is based on the data taken by the E814/E877 Collaborations at the AGS at BNL with 14.6 AGeV/c Si and 10.8 AGeV/c and 11.5 AGeV/c Au beams.

Chapter 2 is viewed as a continuation of the introduction and briefly discusses the theoretical formalism which is usually involved in calculations of the two-proton correlation function. We also will illustrate the application of this formalism to the calculation of the proton correlation function within a framework of a simple source model.

Chapter 3 offers a sketch of the E814/E877 experimental setups including descriptions of the forward spectrometer and calorimeters.

Chapter 4 presents details on the selection of good events.

In Chapter 5 we discuss issues involved in track reconstruction and selection. Details of particle identification and momentum resolution of the forward spectrometer are discussed there as well.

Chapter 6 discusses specifics of the two-proton correlation analysis. Two-track reconstruction inefficiencies are also discussed there.

Chapter 7 presents results of the analysis of the two-proton correlation functions measured by the E814 Collaboration in 14.6 A·GeV/c Si+Pb collisions at AGS BNL.

Chapter 8 presents the results of the analysis of the two-proton correlation functions in 10.8 A·GeV/c Au+Au collisions.

In Chapter 9 we compare and discuss the measurements of the two-proton correlation functions in Si+Pb at 14.6 AGeV/c and Au+Au at 10.8 AGeV/c reactions. Comparisons with the cascade model RQMD are also presented. Data summarized in this Chapter were the primary objective of this thesis.

Chapter 10 is based on the the results of the analysis of the two-proton correlation functions, measured by the E877 Collaboration in 11.5 A·GeV/c Au+Au collisions at AGS BNL. Analysis of the centrality dependence of the correlation function is presented. First measurements of the dependence of the correlation function on the orientation of the pair relative to the reaction plane is also discussed.

Chapter 11 presents the analysis of the proton-deuteron correlations in Au+Au collisions and briefly describes the model calculations based on RQMD with a coalescence after-burner.

Chapter 12 offers some conclusions and outlook.

Some results of various projects in which I have been involved during this thesis work are collected in the various Appendices.

That's about it. Good luck with the reading!

Chapter 2

Two-Proton Correlations: Formalism and Models

In this chapter we will discuss the theoretical formalism usually involved in calculations of the two-proton correlation function. We also will illustrate the application of this formalism to the calculation of the proton correlation function within a framework of a simple source model. This model will be used to illustrate generic dependences of the correlation function on the source parameters such as source size, duration of emission and temperature. It will essentially serve as a "calibration" of the method.

2.1 Preliminary Remarks

The process of extracting meaningful data from the two-particle correlation measurements is, unfortunately, model dependent. This dependence comes from two sources. First, one has to use some assumptions about the properties of the source which emits particles. We will briefly discuss the current situation with models in section 2.2. Second, it is necessary to take into account interactions between particles and that involves certain approximations. Related issues will be presented in section 2.3

2.2 Models, Models...

The present situation on theoretical descriptions of relativistic heavy ion collisions is somewhat ambiguous. There are two main approaches. On one hand there are attempts to describe the nucleus-nucleus collisions as a superposition of nucleon-nucleon and hadron-hadron collisions. Transport models or "hadron cascades", such as ARC [16], HIJING [17], FRITIOF [18], RQMD [20], VENUS [19], etc., are examples of this approach. They prove to be fairly successful in the description of heavy-ion collisions. On the other hand there are attempts to apply proven methods of statistical mechanics by assuming that the system created after the collision achieves complete thermalization. The so called thermal and hydrodynamical models are examples of this approach.

In principle the second approach is more appealing than the first. Presently, the important details involved in the transport models such as nucleon structure, particle and resonant creation in hadron-nucleus collisions, etc., are poorly understood. The assumption of thermalization allows us to bypass the details and uncertainties of the reaction dynamics and use powerful methods of statistical mechanics[1]. It also seems more natural to assume that in high energy nucleus-nucleus reactions, where hundreds (at AGS) and thousands (at SPS) of hadrons are produced, thermalization may be reached. And indeed there are convincing experimental evidences that thermalization has been reached, see for example [31].

The problem is that the time needed for the system created in a collision to reach thermal equilibrium is unknown. And presently, reliable estimates of the thermalization time can be achived only by simulating microscopic dynamics of the reaction. But such simulations require knowledge of in-medium and free-space interaction cross sections for various particles, densities achieved in collisions, etc. - quantities which are not very well known.

2.3 Correlation Function Formalism

To perform actual calculations of the correlation function one should be able to take into account effects of quantum statistics and final state interactions between two particles. The first attempt of numerical calculation of the two-proton correlation function was made in the pioneering paper of Koonin [23]. Later, several authors [24, 59] suggested refined techniques for calculations of model correlation functions of interacting particles, which were subsequently widely used for comparison with experimental data. In our study we mostly used computer code developed by Scott Pratt [59] which is espe-

[1]Fermi was the first one who suggested [21, 22] the idea of considering the collision process at very high energies by the use of thermodynamic methods.

cially suitable for calculations involving phase space produced by Monte-Carlo event generators. A detailed description of the method and its applications can be found elsewhere [60]. As a cross-check, for some calculations we also used code based on the Lyuboshits-Lednicky [24] approach. We conclude that both codes generate similar results within our set of the source parameters.

We will follow [46] in the description of the basic ideas in calculation of the correlation function. Experimentally a correlation function can be obtained[2] from the ratio of coincidence yields $Y_{12}(\mathbf{p_1}, \mathbf{p_2})$ to the single proton yields $Y_1(\mathbf{p_1})$, $Y_2(\mathbf{p_2})$.

$$Y_{12}(\mathbf{p_1}, \mathbf{p_2}) = N_{12}\left[1 + R(q)\right] \sum Y_1(\mathbf{p_1}) Y_2(\mathbf{p_2})$$

Here p_1 and p_2 are measured momenta of the particles and $q = \frac{1}{2}\left|\mathbf{p_1} - \mathbf{p_2}\right|$ is the relative momentum of the pair. Note that we use the notation $C2 \equiv 1 + R(q)$ on the figures in this paper. The normalization constant N_{12} is usually determined by the requirement that $R(q) = 0$ for sufficiently high values of q, typically $q > 50$ MeV .

$$C2 = 1 + R(\mathbf{p}, q) = \frac{P(\mathbf{p_1}, \mathbf{p_2})}{P(\mathbf{p_1}) P(\mathbf{p_2})}$$

where $P(\mathbf{p_1}, \mathbf{p_2})$ is a probability of two-particle emission and $P(\mathbf{p_1})$ is a single-particle emission probability.

One can write the probability of creating two particles with momenta

[2] In Chapter 6 we will discuss a slightly different notation for the correlation function.

$\mathbf{p_1}, \mathbf{p_2}$ at space-time points x_1, x_2 while the rest of the system is in some state labeled f as:

$$P(\mathbf{p_1}, \mathbf{p_2}) = \sum_f \left| \int d^4x_1 d^4x_2 \; T_f(x_1, x_2) U(x_1, x_2, \mathbf{p_1}, \mathbf{p_2}) \right|^2 . \tag{2.1}$$

The matrix T_f describes the creation of two particles at x_1, x_2 with the rest of the system in some final state, which do not further interact with the two particles[3]. The matrix U describes the evolution of particles created at x_1, x_2 to their asymptotic momentum states $\mathbf{p_1}, \mathbf{p_2}$. An assumption of independent emission leads to factorization of matrix $T(x_1, x_2) = T(x_1)T(x_2)$. After transformation to the new coordinates and squaring of the matrix elements one can rewrite 2.1 as:

$$P(\mathbf{p_1}, \mathbf{p_2}) = \int d^4x_1 d^4\delta x_1 d^4x_2 d^4\delta x_2 \; S_1(x_1, \delta x_1) S_2(x_2, \delta x_2) W_{p1,p2}(x_1, \delta x_1, x_2, \delta x_2). \tag{2.2}$$

Here x_i is the mean and δx_i the relative positions of a pair. We used notation

$$S_i(x_i, \delta x_i) = T_i^\dagger(x_i + \delta x_i/2) T_i(x_i - \delta x_i/2)$$

and

$$W_{p1,p2}(x_1, \delta x_1, x_2, \delta x_2) = U^\dagger(x_1 + \delta x_1/2, x_2 + \delta x_2/2, \mathbf{p_1}, \mathbf{p_2}) U(x_1 - \delta x_1/2, x_2 - \delta x_2/2, \mathbf{p_1}, \mathbf{p_2}).$$

The four-dimensional Wigner transform introduces a momentum dependence of the source function instead of a dependence on δx. Transforming the source

[3] **To make notation shorter we will assume only one possible state of the system and will drop the summation over index *f*.**

function

$$\tilde{S}_i(x,k) = \int d^4\delta x\ S_i(x,\delta x) e^{i\delta x k}$$

and evolution operator

$$\widetilde{W}_{p1,p2}(x_1,k_1,x_2,k_2) = \int d^4\delta x_1 d^4\delta x_2\ W_{p1,p2}(x_1,\delta x_1,x_2,\delta x_2)\ e^{-i\delta x_1 k_1 - i\delta x_2 k_2}$$

we rewrite 2.2 as

$$P(\mathbf{p_1},\mathbf{p_2}) = \int d^4x_1 d^4k_1 d^4x_2 d^4k_2\ \tilde{S}_1(x_1,k_1)\tilde{S}_2(x_2,k_2)\widetilde{W}_{p1,p2}(x_1,k_1,x_2,k_2). \tag{2.3}$$

Assuming that $\tilde{S}(x,E,(\mathbf{k_1}+\mathbf{k_2})/2) \approx \tilde{S}(x,E,\mathbf{k}_i/2)$ and taking into account that the evolution matrix factorizes into a phase factor part and a part which depends only on the relative coordinates, one can finally (after performing some algebra) write (1) as:

$$P(\mathbf{p_1},\mathbf{p_2}) = \int d^4x_1 d^4x_2\ g(\mathbf{P}/2,x_1)g(\mathbf{P}/2,x_2)|\phi(\mathbf{q},\mathbf{x_1}-\mathbf{x_2}-(t_2-t_1)\mathbf{P}/2m)|^2 \tag{2.4}$$

Here $g(\mathbf{P}/2,x_i)$ is a single-particle emission probability and $\phi(\mathbf{q},\mathbf{r})$ is the relative wave function of the two emitted particles. $\mathbf{P}$ denotes the total momentum of the pair and $\mathbf{q}$ is their relative momentum.

Sometimes it's more convinient to rewrite the correlation function in a slightly different form :

$$C2 = 1 + R(\mathbf{P},q) = \int d^3r\ F_{\mathbf{P}}(\mathbf{r})|\phi(\mathbf{q},\mathbf{r})|^2$$

where $\mathbf{r} = \mathbf{r_1} - \mathbf{r_2}$ is a relative coordinate of a pair. $F_{\mathbf{P}}(\mathbf{r})$ is defined as

$$F_{\mathbf{P}}(\mathbf{r}) = \frac{\int d^3\mathbf{R}\ f(\mathbf{P}/2, \mathbf{R} + \mathbf{r}/2, t_>) f(\mathbf{P}/2, \mathbf{R} - \mathbf{r}/2, t_>)}{\left|\int d^3r'\ f(\mathbf{P}/2, \mathbf{r}', t_>)\right|^2}$$

where $\mathbf{R} = (\mathbf{r_1} + \mathbf{r_2})/2$ is the coordinate of the pair's center of mass. The Wigner function $f(\mathbf{p}, \mathbf{r}, t_>)$ is a phase-space density of protons with momentum $\mathbf{p}$, position $\mathbf{r}$ at some time $t_>$ after emission. It may be obtained from the source emission function:

$$f(\mathbf{p}, \mathbf{r}, t_>) = \int_{-\infty}^{t_>} dt\ g(\mathbf{p}, \mathbf{r} - \mathbf{p}(t_> - t)/m, t).$$

If a particle stops to interact at a time earlier than $t_>$, then the relative Wigner function $f(\mathbf{p}, \mathbf{r}, t_>)$ is independent of the choice of $t_>$. This particular form shows more clearly effects related to the source lifetime as well as dependence of the correlation function on the pair momentum.

The outlined formalism is convenient for Monte Carlo calculations [60]. Using a phase space distribution, obtained from any suitable model, as an input for generation of the sample pairs, one can calculate relative coordinates and momentum in the rest frame of the pair and use squared wave function as a weight of a pair. The relative wave function $\phi(\mathbf{q}, \mathbf{r})$ influences correlations via strong and Coulomb interactions. Also one should take into account the antisymmetrization requirement imposed by Fermi statistics of protons [4].

[4] For noninteracting identical particles with nonzero mass, the squared relative wave function has the form $|\phi(\mathbf{q}, \mathbf{r})|^2 \approx 1 + \frac{(-1)^{2S}}{(2S+1)} \cos(2\mathbf{qr})$ where S denotes the spin of the particle.

Independent emission of particles was assumed in derivation of the above formulas as well as a condition of a small relative momenta of pairs, i.e., $\mathbf{q}$ is required to be much less than the characteristic momentum in $g(\mathbf{P}/2, x)$. Which in case of a thermal system is $|p| \approx \sqrt{3mT}$, where T is source temperature and m is particle mass. The latter requirement is explicitly satisfied in our analysis.

2.4 Static Source Model

In this section we will describe the so called static Gaussian model- a simplified approach to the generation of a phase space distribution. Let us start with some general remarks concerning this method.

Some variations of this model were used in the past in a the number of studies (for an extensive review see [7]) predominantly for the analysis of the two proton correlations at low energy (order of several hundred MeV) nucleus nucleus collisions. In a recent paper [34] this type of model was used for a p-p correlation analysis by the WA80 collaboration at SPS energies. It is also a standard parametrization in studies of two-pion correlations. The simplicity of the model has its advantages and its drawbacks. Among those advantages are: (1) a clear insight of the basic dependencies of the p-p correlation function on relevant parameters of the system; (2) a model phase space can be generated in a straightforward and CPU nonintensive way which allows high statistics data sets within a reasonable period of time (usually not the case with cascade type event generators such as RQMD); (3) it is an excellent tool for testing the software involved in calculations of the proton-proton correlation function.

The main flaw of this model is that, physics-wise, it is oversimplified and naive. It omits, intentionally though, many important features of nucleus-nucleus collisions such as radial expansion and resonance production to mention a few. Furthermore, although it is sometimes used in the literature [34, 48], a zero life time approximation can hardly be considered realistic for nucleus-nucleus reactions.

We feel that this approach can be justified in situations when there is no reliable and detailed information about the investigated system and one is forced to use some crude assumptions. In our opinion modern cascade generators provide a more powerful and insightful tool for the study of ultra-relativistic nuclear collisions in general and two-particle correlations in particular. Nevertheless it is useful and instructive to perform calculations using simple methods. Keeping all that in mind we will proceed to present and discuss the results of the static Gaussian model calculations.

2.4.1 Assumptions and source parametrization

The model postulates that the particle source is a spherically symmetric static system with Gaussian distributed $\mathbf{x}$, $\mathbf{y}$, $\mathbf{z}$ coordinates, and some (very short or zero) life time τ. There is no correlation between coordinates and momentum. The source emits particles with a momentum distribution resembling the experimentally measured one. In this study we used the transverse mass spectrum distributed according to the Boltzmann law with some temperature

T. The choice of the temperature was based on the experimentally measured transverse mass spectrum. An extensive discussion about thermalization in heavy-ion collisions can be found in [31] and the references cited therein.

Parametrization of the source function was chosen as:

$$\rho(\vec{r},t) \sim e^{-|\vec{r}|^2/2R^2 - t^2/2\tau^2}.$$

Spherical symmetry of the source implies equality of rms values[5] :

$$\langle x^2 \rangle = \langle y^2 \rangle = \langle z^2 \rangle = R^2$$

and

$$\langle t^2 \rangle = \tau^2.$$

Parameter R is usually referred to, in the studies devoted to correlations of identical pions, as the *one-dimensional root-mean-square radius.* Another parameter often used in the literature [47] is the so called *three-dimensional root-mean-square radius*, simply related to it's one dimensional counterpart by

$$R^{3d}_{rms} = \sqrt{{R_x}^2 + {R_y}^2 + {R_z}^2}.$$

For a symmetric source

$$R^{3d}_{rms} = \sqrt{3}R.$$

It is useful to remember the relation between a uniform sphere of radius R_S, which is sometimes assumed in calculations of the target or projectile sizes,

[5] We will also denote in the text $\langle x^2 \rangle^{1/2}$ as R_x, $\langle y^2 \rangle^{1/2}$ as R_y and $\langle z^2 \rangle^{1/2}$ as R_z.

and R^{3d}_{rms} of the symmetric Gaussian source. Simply

$$R^{3d}_{rms} = \sqrt{3/5}R_S$$

Note the factor of $\sqrt{5}$ between a uniform sphere radius and Gaussian parameter R [6].

A popular variation of the Gaussian source parametrization of

$$\rho(\vec{r},t) \sim e^{-|\vec{r}|/R_K^2 - t^2/\tau_K^2}$$

leads to an appearance of an additional factor of $\sqrt{2}$.

$$R = R_K/\sqrt{2}$$

One should keep in mind these (rather trivial) relationships when comparing data from various experiments. For an excellent review of model sources for particle emission as well as overview of intensity interferometry in subatomic physics we direct the interested reader to [8] .

2.5 Results of the Calculations

As we said earlier, the main reason for measurement of the two-proton (as well as any other particle) correlation function is a hope to extract some information about the space and time extent of the emitting source.

[6]It is worth mentioning here that the difference in the proton correlation functions corresponding to Gaussian source and uniform spherical source distributions (with the same rms radius $\langle r^2 \rangle^{1/2}$) was found [42] to be small. The same observation was made in [46].

2.5.1 Source size dependence of the two-proton correlation function

Figure 2.1 shows the proton-proton correlation function (denoted as C2) calculated [7]for static Gaussian sources with fairly arbitrarily chosen parameters. One can see a characteristic "bump" at about 20 MeV/c, which is due to the interplay of the effects of quantum statistics, Coulomb repulsion and the strong resonant[8] attraction in a two proton system. Indeed, one can notice the sensitivity of the correlation function to the change of the source size. We have chosen (following [42] and others) as a criteria of the strength of the correlation function its value at q_{inv}=20 MeV – where the maximum is located. It is a somewhat arbitrary choice but it gives a reasonable feeling of the correlation function behaviour, conveniently allowing one to not plot a multitude of figures and curves.

Figure 2.2 shows the dependence of the height of the correlation function peak on the one-dimensional radius R of the source. The peak value changes, within 5% accuracy, inversely proportional to the radius. The same (with somewhat less accuracy) can be said about the peak value of the reduced

---

[7]The statistics and binning in this calculations were chosen to match approximately the statistical errors and binning of the correlation function measured by E877 collaboration in Au+Au collisions at the energy 10.8 AGeV/c, during 1993 run. It was intended to illustrate the sensitivity of the data.

[8]As was mentioned in [46], strictly speaking the so called ^2He "resonance" is not a resonance, since the phase shift does not increase by 90°, but only by about 60°.

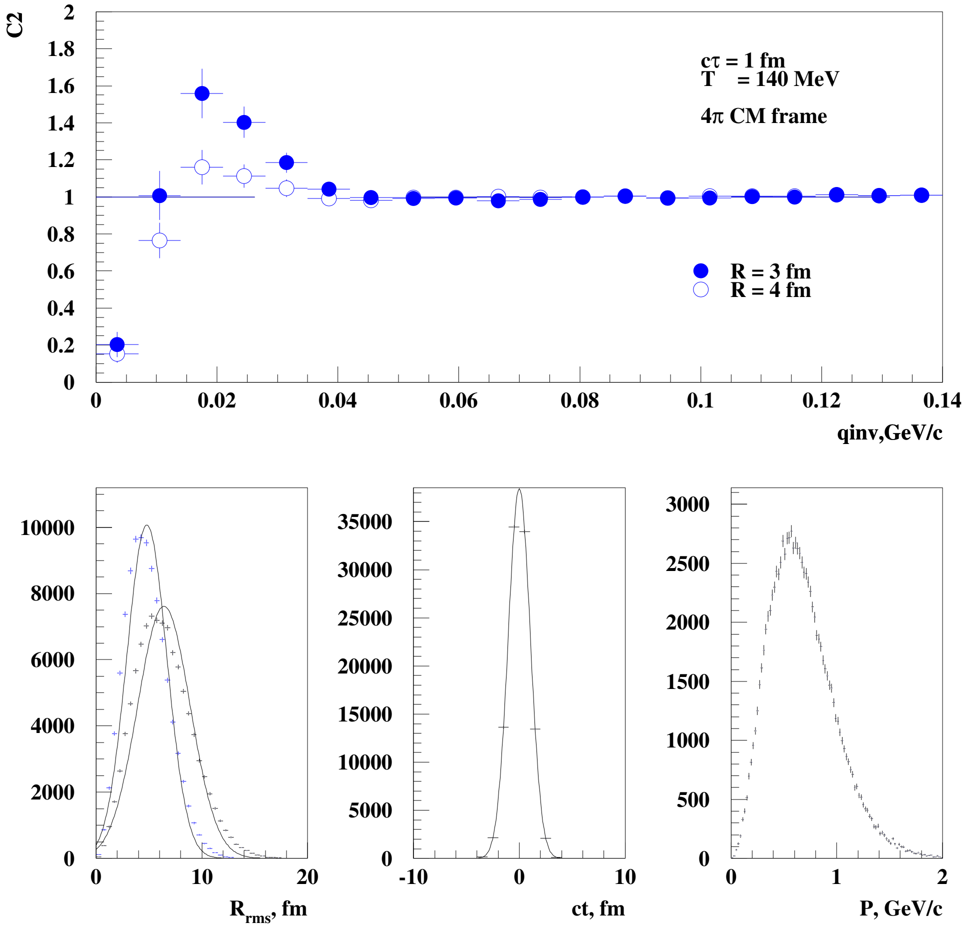

Figure 2.1: Upper panel:Two-proton correlation function for Gaussian sources with two different one-dimensional radii. Lower panels: Source parameter distributions: (From left to right) three-dimentional rms radii of the sources, emission time, momentum of the particles.

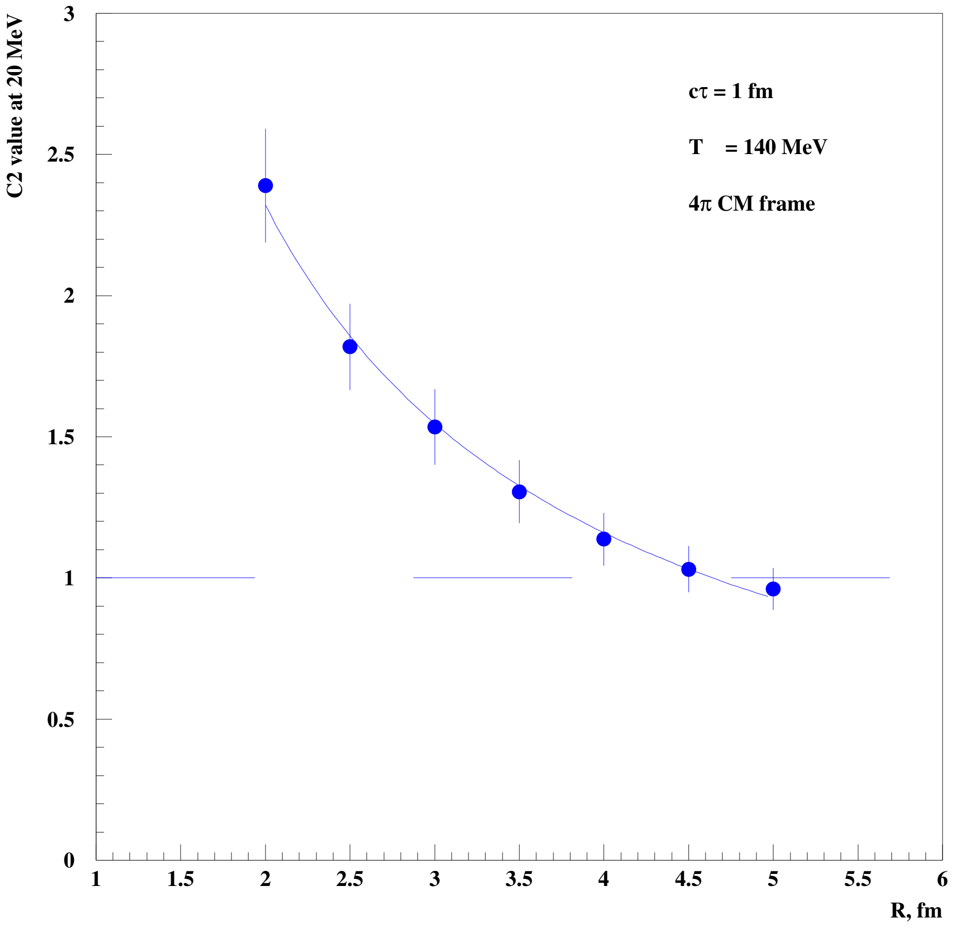

Figure 2.2: Value of the correlation function at q_{inv}=20 MeV/c as a function of R. Line shows a fit to the function $f(R) = const/R$. See description in the text.

correlation function and the volume parameter R^3, shown in Figure 2.3.

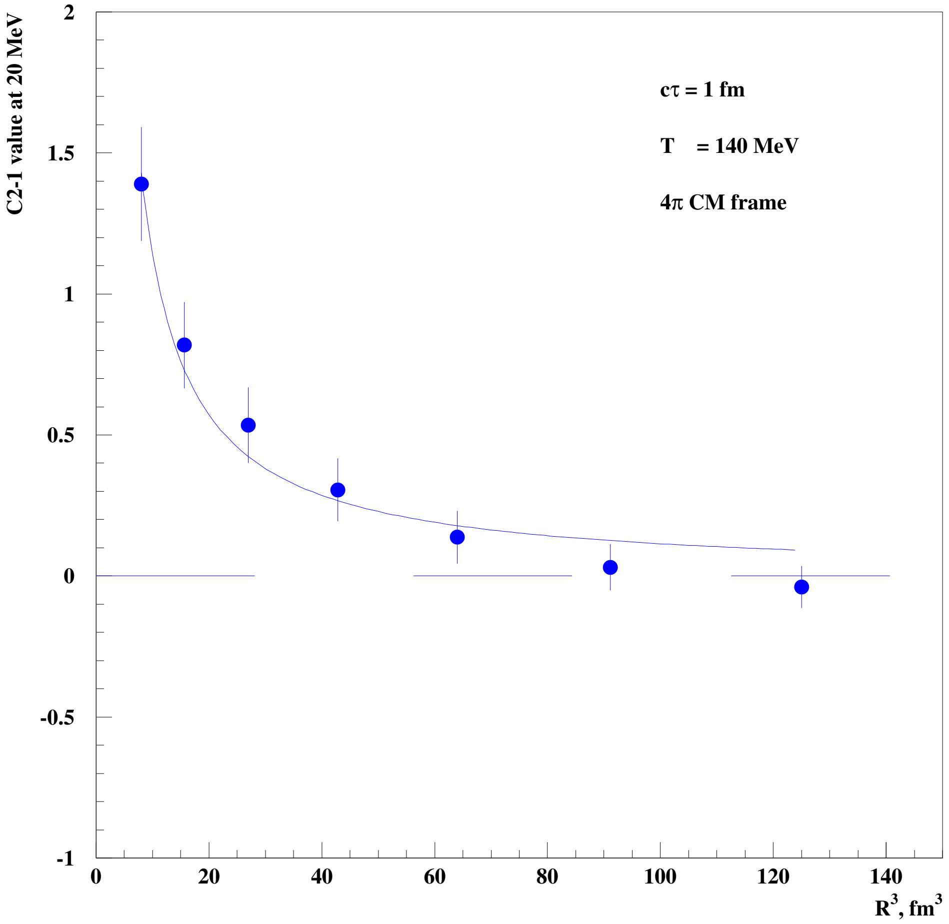

Figure 2.3: Value of the correlation function minus one at q_{inv}=20 MeV/c as a function of R^3. The line shows a fit to the function $f(R) = const/R^3$. See description in the text.

2.5.2 Dependence on the Life-Time of the Source

Figure 2.4 shows the dependence of the correlation function peak on the lifetime of the emitting source. The general trend is that the peak value gradually diminishes with the increase of the system lifetime, similar to [7]. This will lead to difference in the "observed" sizes for systems with different lifetimes, which are otherwise identical to each other. The effect is easily understood if one recalls that the effective distance between two emitted particles is of the order $R + v\tau$, where v is an average velocity of the particles and τ is an average time interval between two emissions. Note the "plateau" at values of the parameter $c\tau$ smaller then 3 fm [9]. This may suggest that the temporal extent of the source starts to play a role only after its value exceeds the value of the characteristic length of the source. To illustrate this point Figure 2.5 shows complete correlation functions for $c\tau$=1 and 3 fm which look rather similar to each other.

2.5.3 Temperature Dependence

The majority of the existing calculations in the literature were performed for sources with temperatures of the order of few MeV. It is instructive to perform calculations in the range of temperatures typical for the nucleus-nucleus collisions at AGS. The temperature dependence of the correlation function naturally arises for the sources with a nonzero lifetime and enters through the

[9] which is a characteristic length of the spatial dimension of the source in this particular case.

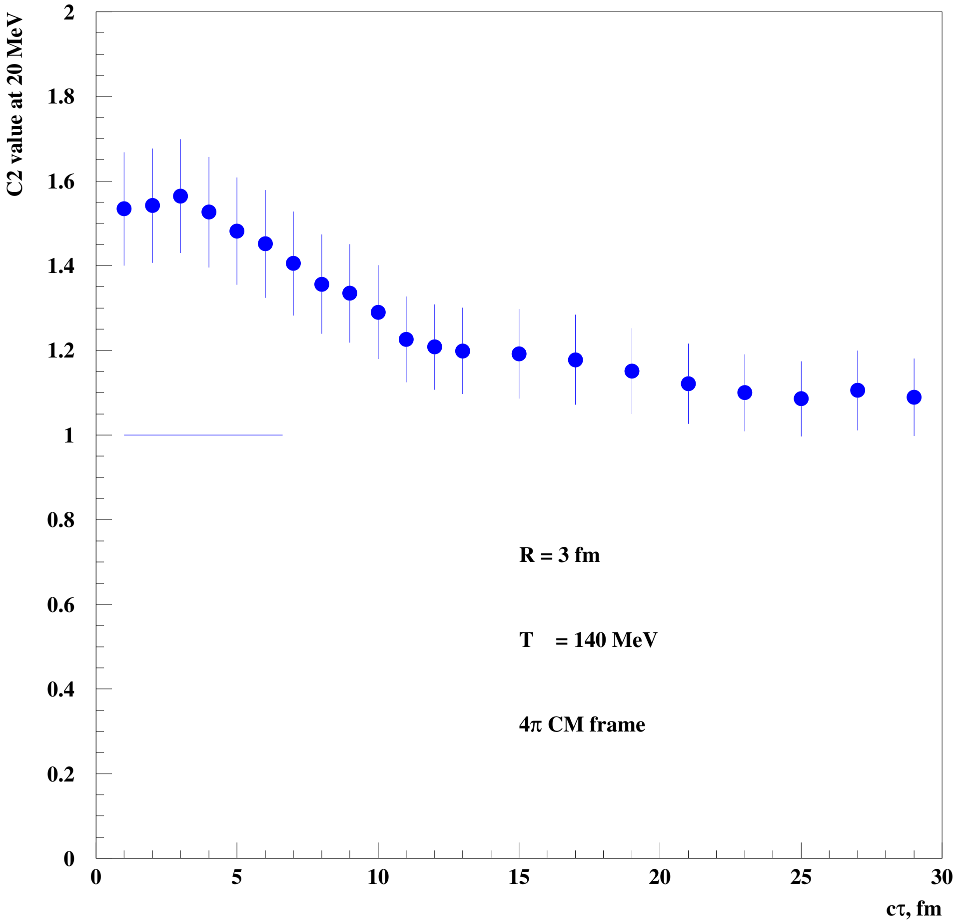

Figure 2.4: Dependence of the two-proton correlation function on the lifetime of the source.

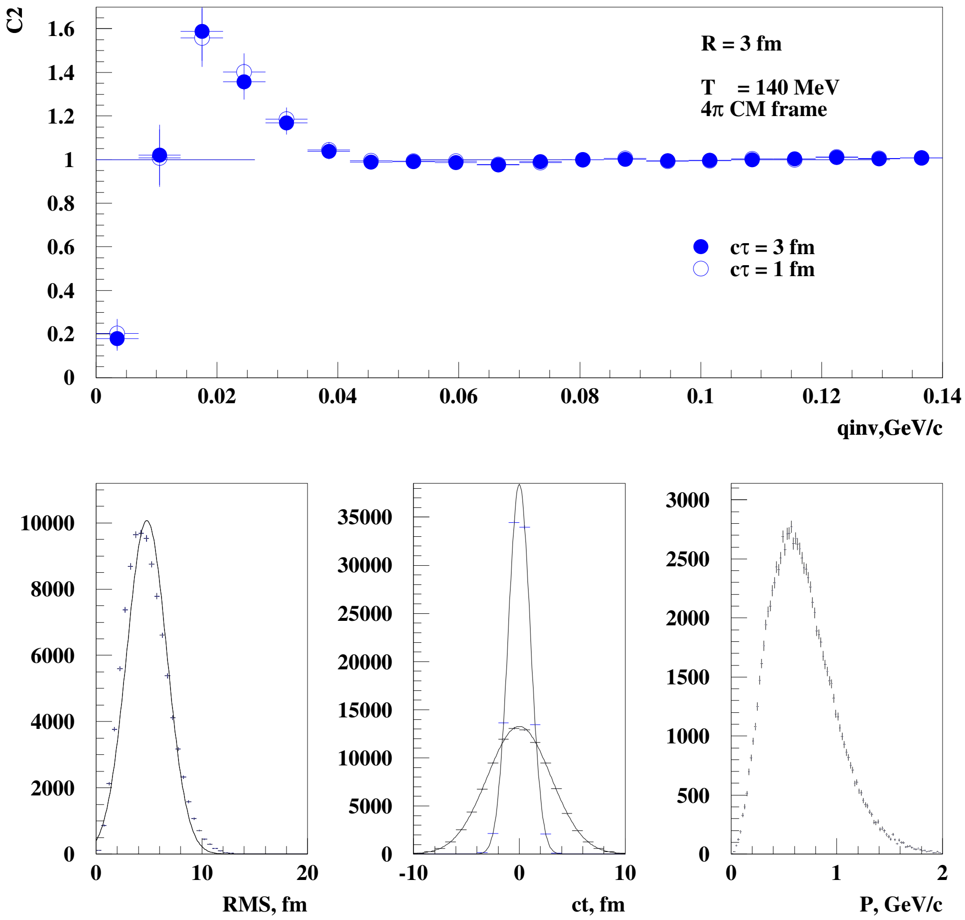

Figure 2.5: Dependence of the two-proton correlation function on the lifetime of the source for two particular choices of τ.

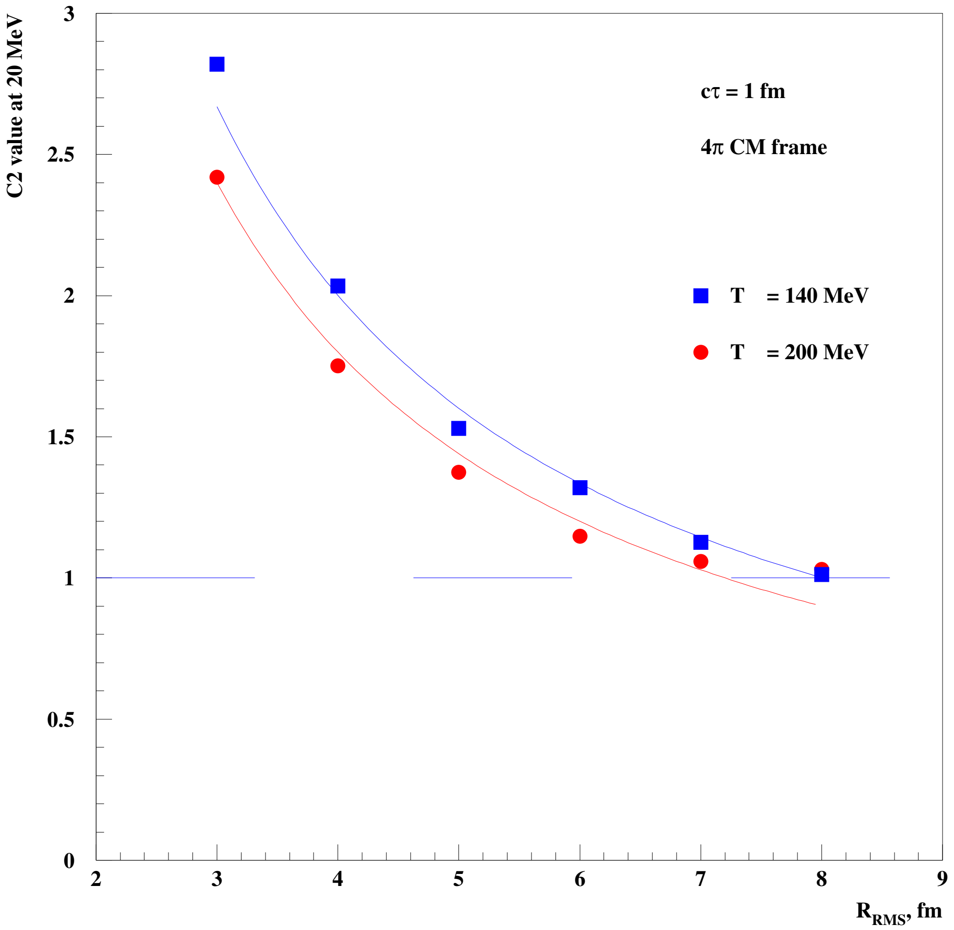

Figure 2.6: Value of the correlation function at q_{inv}=20 MeV/c as a function of R^{3d}_{rms} for different temperatures of the system. The line shows a fit to the function $f(R) = const/R$. See description in the text.

average velocity of the emitted particles. For a source with the radius r, time of emission τ, which emits particles with an average velocity v the average separation scale between two particles will be of the order of $\delta r = |r + v \cdot \tau|$. The average velocity is proportional to the square root of the temperature therefore the source of the same size and lifetime but higher temperature will have apparent radius (probed with the help of the correlation function) larger then the similar source with the lower temperature.

Figure 2.6 shows the dependence of the height of the correlation function peak on the *three-dimensional (remember factor $\sqrt{3}$!)* radius R^{3d}_{rms} for two different temperatures of the source. The effect of the decrease of the correlation function peak value with the increase of the source temperature can be clearly seen. The two values of temperature for which the calculations were performed roughly correspond to the interval of the proton temperatures measured at AGS energies.

Chapter 3

E814/E877 Experimental Setups

Data presented in this thesis were taken at different times by different collaborations. Therefore we will use a “historical” approach to the description of the E814/E877 experimental setups. First, this approach will allow us to avoid repetitions in the description of the the experiments, which share many common features. Second, it will help us to show the evolution and improvements of the apparatus which were dictated by the changing collision environment and different physics goals of the experiments.

The Si+Pb data set was obtained by the E814 Collaboration and Au+Au data were taken by the E877 Collaboration. Both were working on the C5 beam line at the Alternating Gradient Synchrotron at Brookhaven National Laboratory (AGS BNL). In this chapter we will give a brief introduction to the main features of both setups. Various detector subsystems and the aspects of their utilization in the analysis procedure will be discussed in greater details in the next chapters.

The E814 experiment was initially intended for peripheral collision studies, including measurements of projectile fragmentation and projectile inelastic scattering with about 1 MeV excitation energy resolution (see for example Reference [35]). The capabilities of the apparatus allowed subsequent studies of central collisions, by measuring the distribution of transverse energy (E_T) and charged particle multiplicity and studies of associated baryon and meson spectra with an emphasis on low to intermediate transverse momenta [43]. A two-pion correlation study was also attempted and yielded interesting results [13].

With the advent of the Au beam at AGS in 1992, the new E877 Collaboration took over the C5 beam line. The E877 experiment at BNL was largely based on it's predecessor: E814. Tracking and time of flight (TOF) systems were significantly upgraded, as well as the trigger and data acquisition system, in order to cope with the high multiplicity environment of Au+Au central collisions.

E877's physics goals are measurements of the distribution of E_T and charge particle multiplicity and studies of associated baryon and meson spectra with emphasis on low to intermediate transverse momenta. Also, studies of the directed nuclear flow were some of the main goals. Measurements of two-particle correlation functions were intended from the very beginning of the experiment.

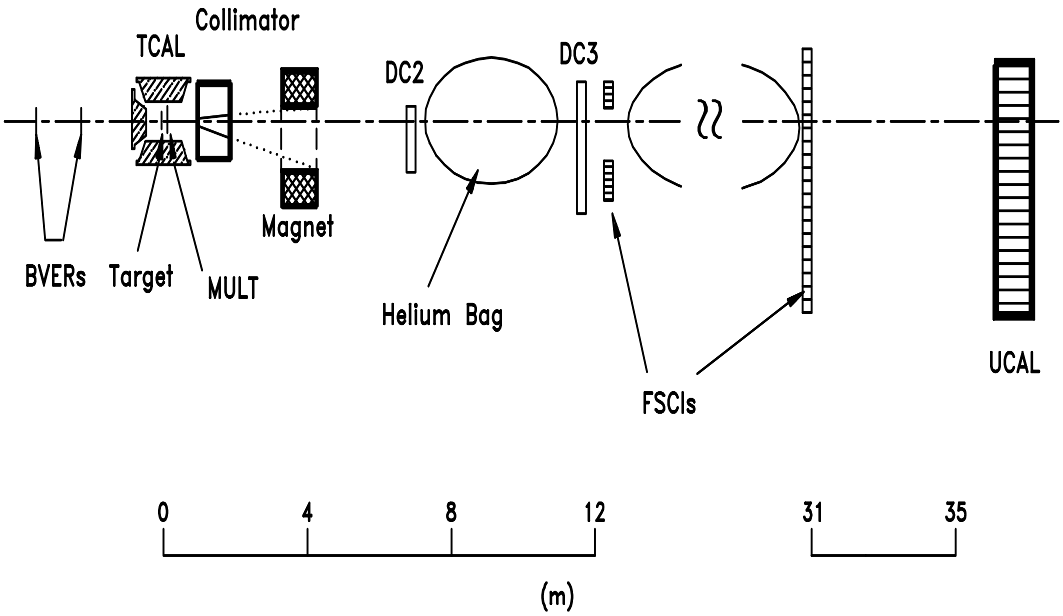

Figure 3.1: The E814 experimental setup. Beam enters from the left. See description in the text.

3.1 E814 Apparatus

The Si+Pb data set was taken by the E814 Collaboration at the BNL AGS, during the spring run of 1991. The E814 experimental setup was in its final configuration, with only one magnet and a lead collimator with a stainless steel insert having a larger opening then in previous runs.

The E814 apparatus, schematically shown in Figure 3.1, consisted of several detector groups.

3.1.1 Upstream Detectors

A group of detectors located upstream of the target, consisting of a set of plastic scintillators and silicon detectors, provided information on beam particles and generated a start signal for the TOF system. A better view of the detector layout can be seen on Figure 3.6. We will provide in Chapter 4 an extensive description of this detector group and its utility in the event selection and TOF analysis (see also Appendix D).

3.1.2 Calorimeters

A set of two high granularity sampling calorimeters (TCAL, PCAL), positioned around the target area, provided event by event measurements of transverse energy (E_T) production in the interval of pseudo-rapidity -2.0$< \eta <$4.7 . This measurement was supplemented by the data from a uranium calorimeter (UCAL), located downstream from the forward spectrometer, which covers angles close to zero degrees, thus providing the experiment with the capability of almost 4π measurement of E_T. For a more extensive description of the E814/E877 calorimeters and their utilization see Reference [50] and references therein.

Target Calorimeter (TCAL) The Target Calorimeter is positioned, as its name implies, around the target and provides measurements of transverse energy in the backward (in the collision CM frame) hemisphere. It consists of two structural parts with different coverage: four side walls cover a pseudo-rapidity range from $-0.5 < \eta < 0.8$ and the backward wall covers $-2 < \eta < -0.9$. The schematic layout of TCAL is shown on Figure 3.2. The TCAL is an electro-magnetic calorimeter, composed of 992 NaI(Tl) crystals, positioned in the projective geometry, with a long axis pointing to the target. Such configuration ensures that the particle shower will be contained in a minimal number of crystals. A typical crystal has dimensions of $3.6cm \times 3.6cm \times 13.8cm$. The length of the crystal corresponds to about 5.4 radiation lengths and 0.34 of a hadronic interaction length. For the runs analyzed in this thesis the back wall of the TCAL was removed to create an open space for a ΔE-E scintillator range stack telescope (TELE). Data from the TELE were not used in our analysis.

Participant Calorimeter (PCAL) This device measures energy flow in the forward hemisphere, covering pseudorapidity range $0.83 < \eta < 4.7$. The schematic layout of the PCAL is shown on Figure 3.3. It is a Pb/Fe/Scintillator sampling calorimeter, segmented laterally into 8 radial, 16 azimuthal and 4 depth sections. The total number of detecting elements is 512. Structurally PCAL is divided into four identical, movable quadrants, with a rectangular opening in the middle through which the beam and interaction products pass. The PCAL opening determined the acceptance of the forward spectrometer to be within $|\theta| < 14$ mrad in a so-called "closed" geometry. The opening could be increased by moving the upper quadrants thus creating a larger acceptance (see the E877 description later in this Chapter).

In depth, each segment consists of 2 electromagnetic and 2 hadronic sections. PCAL has a total depth of about 4 hadronic interaction lengths or

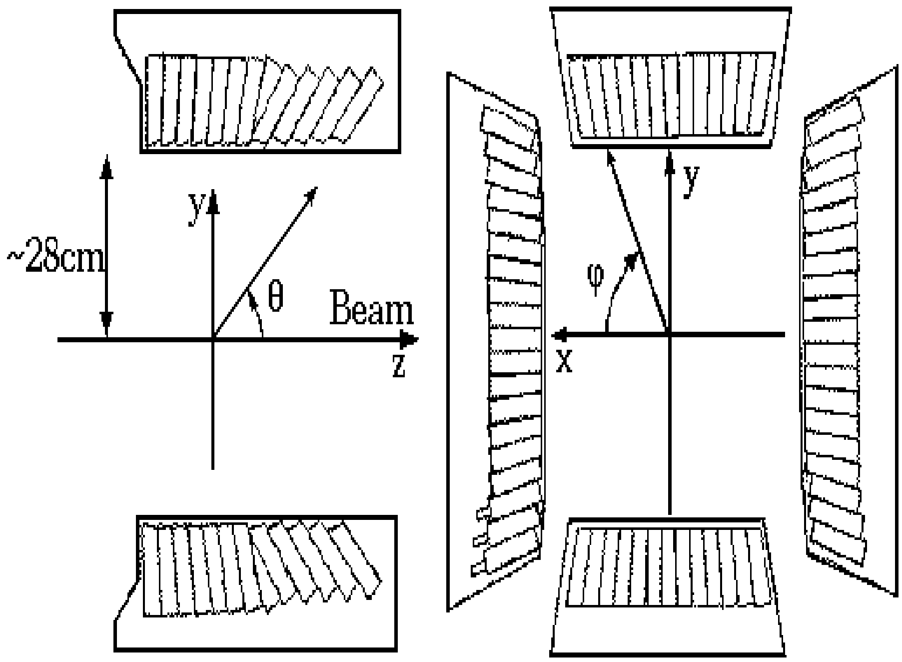

Figure 3.2: The Target Calorimeter layout. Left panel- side view, right panel- rear view. See description in the text.

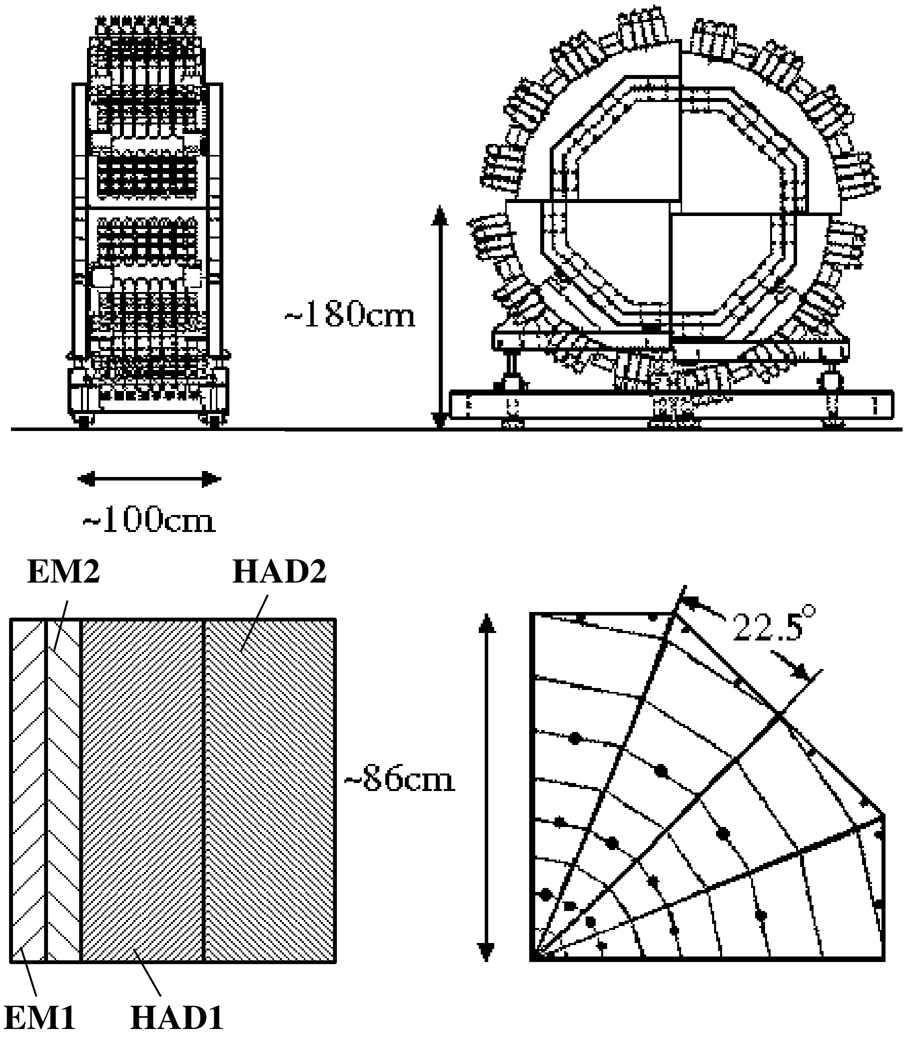

Figure 3.3: The Participant Calorimeter . Upper-left: side view; upper-right: view from target of the assembled PCAL in "closed" configuration. Lower-left: longitudinal segmentation; lower-right: latteral segmentation. See description in the text.

100 radiation lengths. The energy resolution of the electromagnetic sections is $28\%/\sqrt{E(GeV)}$ while the hadronic section resolution is $45\%/\sqrt{E(GeV)}$.

PCAL was designed with the ability to be moved out from the target area. The main purpose for this was maintenance, but such configuration also provided a possibility to run the forward spectrometer in a large acceptance configuration. In such cases a lead collimator was put in place of the PCAL. The angular opening of the collimator was $-111 < \theta_x < 14$ mrad and $-21 < \theta_y < 21$ mrad. The 1991 dataset, discussed in this thesis, was taken in such configuration.

Uranium Calorimeter (UCAL) This calorimeter is located about 36 meters downstream from the target. It consists of 20 segmented modules. Each module has 12 vertical towers consisting of 40 U/Cu/Scintillators blocks. Each block has two 3 cm uranium (^{238}U) plates, one 0.5 cm copper plate as an absorber, interleaved with 0.25 cm thick scintillator sheets. The resolution of this detector was about $50\%/sqrtE$.

3.1.3 Multiplicity Detector

Global event characterization was also performed by a set of silicon multiplicity detectors each segmented in 512 pads and covering the pseudo-rapidity range $0.8< \eta <3.9$. These detectors provided input for the trigger system. Note that the trigger was based on global event characteristics such as measurement of the transverse energy production and charged particle multiplicity in a wide interval of pseudo-rapidity.

3.1.4 Forward Spectrometer

The forward magnetic spectrometer has been used for registration and identification of charged particles. As we already mentioned, in the large acceptance configuration, the spectrometer had a rectangular aperture allowing the beam to pass through[1] it. The angular coverage was -115< θ_x <14 mr in the magnetic bend (horizontal) plane, and -21< θ_y <21 mr in the perpendicular plane [35, 36]. The corresponding coverage in transverse momentum and rapidity is shown in the upper panel in Fig. 3.4 . The 1991 configuration of the spectrometer consisted of the dipole magnet, two drift chambers (DC2 and DC3) and two TOF hodoscopes (FSCI).

Magnet The magnetic analysis of the charged particle momenta is done with the help of the dipole magnet located downstream of the collimator. It can be operated in two different polarities, A and B in the E814/E877 slang. At the AGS, the field polarities of all dipole magnets follow a unique nomenclature. “A” polarity dipoles bend the beam to the same side as the dipoles in the main AGS ring; “B” polarity is the opposite. To put it in a more “visual” way, B polarity deflects positively charged particles towards the bottom on the Figure 3.1. “A” polarity deflects positives in the opposite way. The dimension of the rectangular opening in the magnet was 45.72 $cm\times$ 15.24 $cm\times$ 91.44 cm (18 $inch\times$ 6 $inch\times$ 36 $inch$) in (x, y, z). The z-position of the

[1] This unique “beam through” geometry of the forward spectrometer allowed us to perform direct measurements of the Au beam momentum. We will describe details of the beam momentum measurements in Appendix B

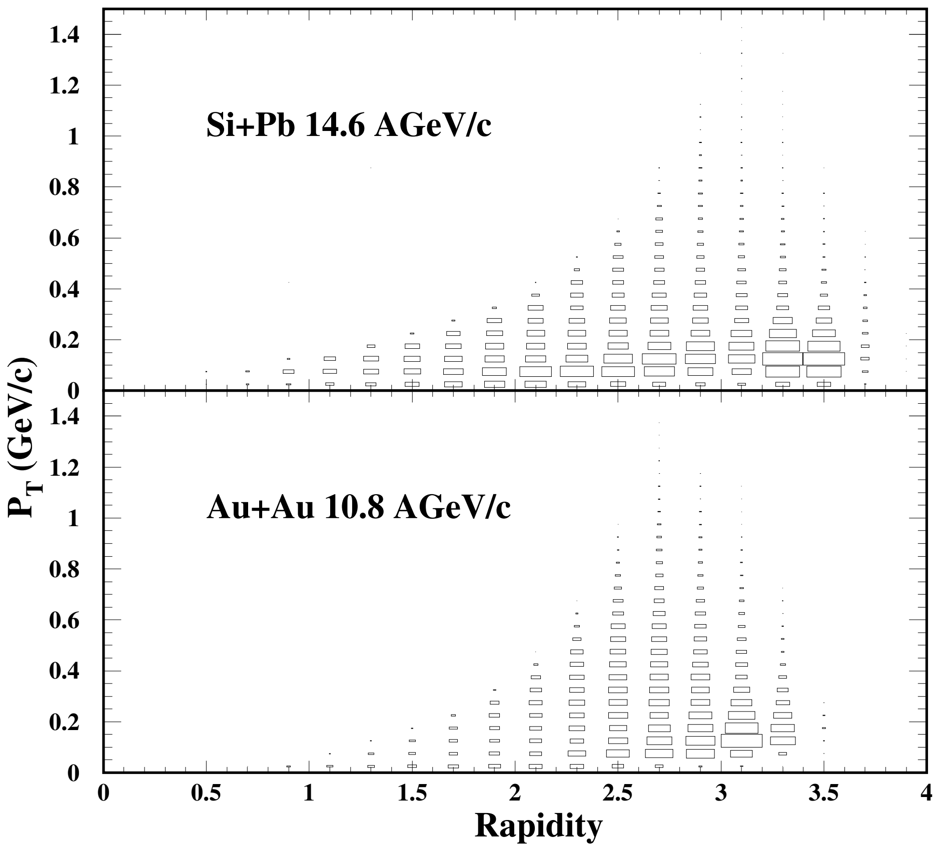

Figure 3.4: E814 (upper panel) and E877 experimental acceptance in rapidity and transverse momentum for protons.

magnet is given in Table 3.1. Typically the magnet was operated at around 10% of its maximum current. Details of the magnetic field mapping can be found in Appendix B.

Drift Chambers Both drift chambers have a similar design, with 6 independent drift planes and one wire plane with a cathode readout. Each drift plane consists of 18μm gold plated tungsten signal wires and 75μm stainless steel field wires. The distance between signal wires is 6.35 mm (quarter inch) in DC2 and 12.7 mm (half inch) in DC3. The differences in geometrical parameters were due to the projective geometry of the spectrometer, different intended distances from the target (see Table 3.1) and, hence, different occupancies per unit surface. The wire planes are separated with an aluminized mylar cathode, with wires in every neighboring plane staggered by a half of the drift cell size. The layout of the chambers is shown schematically in Figure 3.5. The staggering of the planes was done to aid in the resolution of the left-right ambiguity of a hit. For Au runs, the wires in the region where the beam passed through chambers were purposely deadened in order to avoid the high voltage breakdown.

DC2 and DC3 use a gas mixture of 50% Ar and 50% Ethane at atmospheric pressure. The mixture provides a drift velocity of about 51-53 μm/ns at nominal voltages.

The vertical (y) position of a particle hit was determined from measurements of the charge shared by pads on the cathode pad plane. Each chamber had three pad density regions. Regions closest to the beam had the highest pad density in order to cope with a higher occupancy. The DC2 position res-

Detector	Z-position, cm
Magnet Upstream Face	263.4
Magnet Downstream Face	354.8
DC2	692.2
DC3	1156.3
FSCI Upstream	1211.4
FSCI Downstream	3133.7

Table 3.1: Distance from the target of the magnet and detectors in the E814 forward spectrometer.

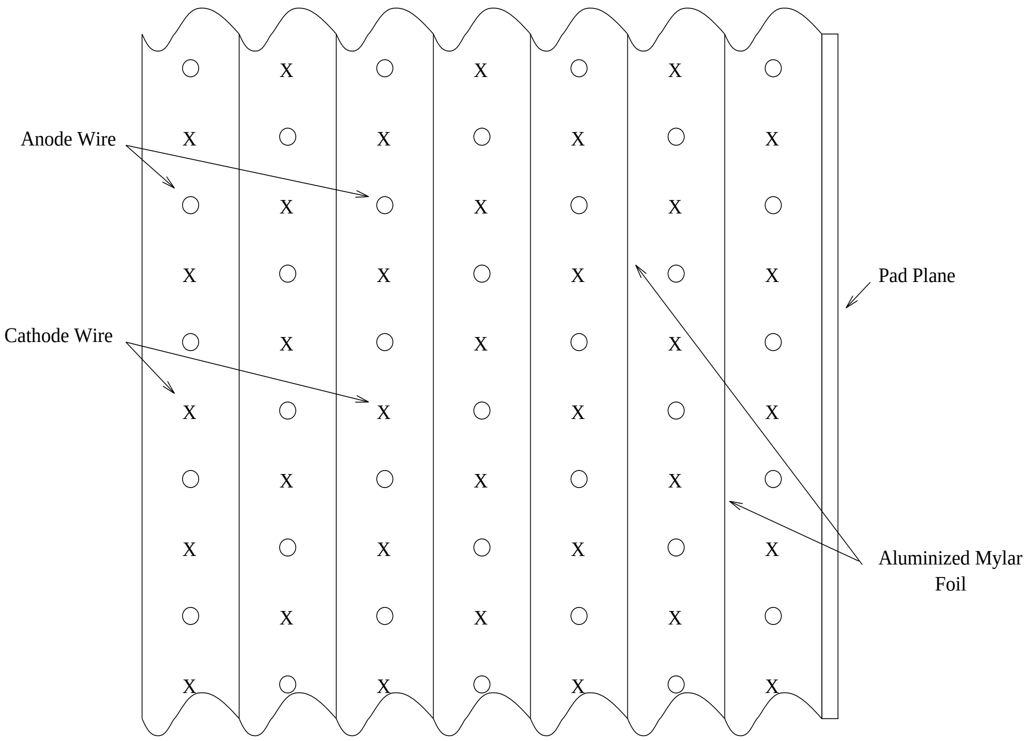

Figure 3.5: Scematic layout of the drift chambers.

olutions in the vertical (y) direction were estimated to be 2.3 mm, 5.1 mm and 15.0 mm for a fine, medium and coarse regions respectively. For DC3 the y-resolutions were 4.3 mm, 7.0 mm and 36.0 mm. The position resolution of drift chambers in the x direction was determined [51] to be approximately 250 μm in DC2 and 300 μm in DC3.

Forward Scintillators (FSCI) The FSCIs consisted of two group of plastic scintillator (BC-404) detectors. One group was positioned about 12 m from the target and had 10 vertical scintillator slats. Each slat had dimensions 10 cm $\times$ 60 cm $\times$ 1 cm $\times$ and was equipped with two photo-tubes. The time resolution of this detector was about 200 ps. The second FSCI group was positioned 31 m from the target and consisted of 39 scintillating slats which were twice as tall as the first group. The time resolution of this group was about 350 ps.

Single charge particles were selected by cuts on the amplitude of the signal in the TOF hodoscope. Simultaneous measurements of the particle rigidity and time of flight in the spectrometer provided particle identification up to the momentum of the beam.

In order to decrease multiple scattering and improve momentum resolution most of the space between the detectors in the forward spectrometer was filled with helium gas.

3.2 E877 Apparatus

The two Au+Au data sets, which we also present in this thesis, were taken during the 1993 and 1994 runs.

The E877 setup is shown in Figure 3.6. The E877 coverage in transverse momentum and rapidity is shown in Fig. 3.4. The parameters of the E877 geometry are listed in Appendix C.

For the 1993 run the opening of the PCAL was increased and the collimator was placed inside. This setup determined the geometrical acceptance with angular coverage -134< θ_x <16 mr and -11< θ_y <11 mr. The vertical acceptance was reduced compared to the E814 configuration in order to limit the multiplicity in the forward spectrometer, since the average multiplicity in Au+Au collisions is approximately 2.5 times higher than in Si+Pb collisions. In order to handle the higher multiplicities, the forward spectrometer was upgraded with a set of four multiwire proportional chambers (MWPC) positioned between the two drift chambers. Also, an additional TOF hodoscope (TOFU) was installed about 12 meters downstream from the target, almost immediately behind DC3.

Multiwire Proportional Chambers (MWPC) Each MWPC has a similar design with differences in sizes dictated by a projection geometry of the forward spectrometer. They had 18 μm diameter gold plated tungsten wires, stringed vertically with 5.08 mm spacing. The wire spacing also determined the x position resolution. The wires in the beam region were also deadened (see description of the drift chambers).

The MWPC utilized a gas mixture of 50% Ar - 50% Ethane at atmospheric pressure. The increased redundancy of tracking was used by the E877 tracking software for confirmation of the tracking solutions determined by the hits in the drift chambers. The detection efficiency of the set of 4 MWPCs was determined to be about 97% with three out of four chambers required for confirmation of the track.

Time of Flight Unit(TOFU) The TOFU consisted of 160 vertical, optically isolated slats, made of plastic scintillator (BC404). Each slat was equiped with photo-multiplier tubes at the top and bottom. The scintillating slats were about 1 m long, with a square cross section of two different sizes. The region near the beam line (-21.0 cm$\leq x <$ 17 cm) had 39 slats which were 1 cm wide. The rest of the TOFU has 1.7 cm wide slats. A time resolution of the calibrated TOFU averaged over all slats and runs was about 90 ps.

Forward spectrometer and track reconstruction software was capable of tracking up to 25 charged particles per event, though an average event contains only about 7. With every consecutive run, the momentum resolution was further improved by adding more helium bags, thus reducing the multiple scattering over a larger part of the particle trajectories in the forward spectrometer. Monte Carlo studies of the momentum resolution showed that it was better than 3% for protons and pions [52, 56]. The resolution was found to be in good agreement with the momentum dependence of the measured width on the proton mass peak (see Chapter 5 for more details).

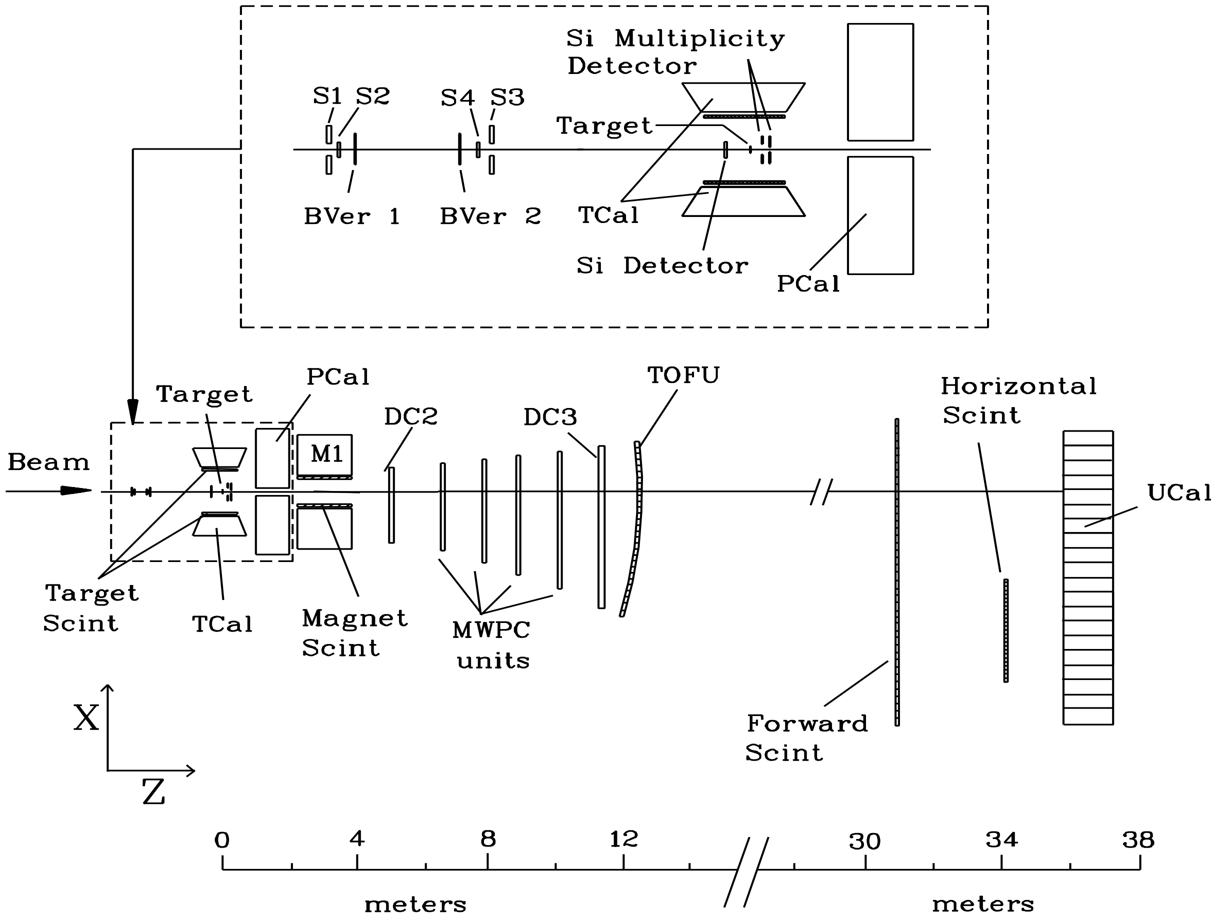

Figure 3.6: E877 experimental setup. See description in the text.

3.3 Trigger System

A grossly simplified picture of the triggering system will be presented in this section. The triggering system evolved, to adapt to the changing physics goals of the experiment. For brevity's sake we will discuss the E877 scheme noting only general features.

Global event characteristics were obtained with the help of calorimeters or multiplicity detectors. A typical time structure of the AGS Au beam was a 1.5 sec long spill with a 4 second period. During the spill usually about 20k ions satisfied the *beam trigger* requirement: signals in BSCI2 and BSCI4 with no signal in veto counters BSCI1 and BSCI3 (see Chapter 4). Typical Au targets utilized by E877 were about 1 or 2% of the Au beam interaction length. These conditions lead to about 200 to 400 inelastic interactions in the target. In order to select these interactions out of the stream of *beam triggers* some energy deposition in PCAL (1 GeV and higher) was required in order to generate the so called *pre-trigger*. A *first-level trigger* insures that no beam particle has entered the apparatus within 1 μs after the "pre-triggered" particle. The next, *second-level trigger* decision is based on the the signals from the TCAL, PCAL and multiplicity detector. The analog signal from these triggering detectors is digitized by the Fast Analog to Digital Converter (FERA ADCs) and summed together in the Arithmetic Logic Unit (ALU). The summed signals are proportional to the E_T deposition in the certain calorimeter and the number of hits in the multiplicity detector. E814 used a trigger based on the multiplicity measurements, E877's second-level trigger was based on the information from calorimeters. ALU output was analyzed by the Programmable Logic Unit which compared the digitized sum with a set of the predefined thresholds. The thresholds are designed to select a predetermined number of events, based on the DAQ maximum throughput. Typically, the early E877 DAQ system, for example the 1993 version, was able to "digest" about 50 events per spill[2]. All events with an energy deposition signal above the highest threshold in the PLU were fully digitized and written on tape. Events passing the next thresholds were downscaled by some predefined factor. This provided the balanced mixture of events with different transverse energy depositions and hence different centralities. Trigger masks for every event were written on tape and the natural shape of the E_T deposition was reconstructed during the offline analysis.

3.4 Data Acquisition and Monitoring

Front End Most of the electronic components were located in the climate controlled electronics room in the E814/E877 counting house. The digitization of the signal from the detecors took place in Fastbus or CAMAC modules. Each Fastbus crate was controlled by a SLAC Scanner Processor (SSP) and the whole Fastbus segment was controlled by a master SSP. During a spill, slave SSPs read out data from the Fastbus modules in its crate and stored them in local memory. Between spills, the master SSP polled all the

[2]This number steadily improved with every run, reaching about 200 in 1995, due to the efforts of the E877 trigger and DAQ teams.

slave SSPs and the CAMAC branch, performed the data readout and events assembly and passed the assembled events to the main DAQ computer. After the readout was completed the slave SSP's memory was cleared.

DAQ System The DAQ computer received data from the master SSP, wrote events on tape and also distributed events for the online monitoring. The central element of the E877 data acquisition system was the VME CES Fast Intelligent Controller[3] (FIC) 8232 based on the Motorola 68030 CPU. The interface between the FIC and the master SSP was handeled by a Fastbus-VSB Interface (FVSBI) module. OS9 operating system was used as a DAQ operating environment. The FIC wrote data directly on to the SCSI EXABYTE 8500 8mm tapes. The interface with the monitoring computer was implemented with a help of the BIT3 VME/GIO dual-port memory module, which was located in the VME crate, and was connected to both FIC and the main monitoring computer - a Silicon Graphics, Inc. (SGI) Indigo workstation. The 8 Mb dual-port memory of the BIT3 module was seen as its own by both Motorola and SGI computers. This allowed a transparent access to the data stream between the master SSP and tapes for the online monitoring software of the experiment.

On-line Monitoring The DAQ software stored events in a circular buffer in the BIT3 memory. This circular buffer was accessible for reading by

---

[3] Also known as Patagonia (because of its Internet address: patagonia.ags.bnl.gov) and during the last run of the E877 as Paranoia. The latter name was undeserved because the DAQ system was working very well during that run.

the dual-port (DP) server program on the SGI workstation. The DP server process distributed events on demand to the client processes running on the same SGI host or on the computers on the E814/E877 counting house network. The communication between the DP server and clients (remote or local) was based on the Remote Procedure Call (RPC) protocol. The server managed communication with its clients in a "fair" way, ensuring that the fast clients are not blocking the clients with a slower turnaround time. The monitoring software was based on the standard E814/E877 data handling package known as STEP1. It was designed to perform the data analysis regardless of the physical source (disk, tape, network or DP server) the event stream is coming from. The input source was specified in the startup parameter file and the changing of the source did not require the recompilation of the code. STEP1 unpacked the raw data into internal data structures and performed the initial calibrations of the data as well as pedestal substractions. It also included a general framework for the data analysis, booking and filling of the histograms, etc.

This approach proved to be very flexible and powerful, allowing reuse of codes developed during the run for monitoring purposes (remaping, addition of the new modules and/or detectors, etc) in the later offline analysis. Basically, the online and offline software were the same. The unification of the general analysis structure provided a steep learning curve and effective sharing of its knowledge within the collaboration.

For the real time monitoring, STEP1 was interfaced via a shared memory section with CERN's Physics Analysis Workstation (PAW) package. PAW was configured to run in the GP style mode with multiple menus and displayed, in real time, data accummulated by the STEP1 routines. STEP1 based Event Display could also be run independentely as one of a DP server's clients, providing a graphical view of the forward spectrometer performance. The entire monitoring framework was run under the Motif Window Manager (MWM) based menu system which allowed management of the whole monitoring system or its particular subsystem by a simple mouse click. The use of PAW and MWM, instead of proprietary visualisation software, proved to be an effective and robust solution. It allowed the use of standard software components and was essentially hardware or operating system independent.

Utilizing the advanced multimedia capabilities of the SGI workstations, the monitoring system included voice and sound extentions. They were used to announce the beginning and the end of the data taking, the end of the tape, etc. as well as to attract the attention of the operator to some "catastrophic" events like the crash of the DP-server or some other subsystems. This increased the interactivity of the online monitoring system, not to mention making it a lot of fun, especially during the night shifts[4].

---

[4]The design of the "talking" subsystem allowed an easy replacement of the sound events, customizing them to the tastes of the current shift crew. As a consequence, the opinions were split on the utility of the whole idea and after some time the sound scheme was enforced to be standard, at least at the time of shift rotation :)

Chapter 4

Event Selection

In this Chapter we will discuss details of the global event selection procedure. For the global event selection in our analysis we have used information from the set of detectors located upstream from the target.

4.1 Upstream Detectors Setup

The description of the E877 experimental setup was introduced in Chapter 3; its layout is presented in Figure 3.6. The upstream group of detectors is shown in the upper insert. During the run time these detectors were used for "good beam particle" definition and determination of these particles parameters, like charge and angle of incidence on the target, as well as for suppression of upstream interactions. Utilizing the E814/E877 detector naming scheme we will call them $BSCI$, $BVER$ and $SILI$. The analysis presented in the current section was performed on the basis of the 1993 gold beam run data, with a 2 percent interaction length Au target. Tracking was performed for the events with transverse energy deposited in the Participant Calorimeter ($PCAL$) greater then 220 GeV which corresponds to about the upper 13.9 percent of the total cross section. We applied the same cut for the presented event selection analysis.

4.2 Beam Scintillators

Beam SCIntillators ($BSCI$) is a group of 4 plastic[1] scintillator detectors equipped with photomultipliers . On Figure 3.6 they are denoted as S1, S2, S3 and S4.We will use different names ($BSCI$) with the same numbering scheme. These detectors are designated to provide start time reference information for the experiment and to discriminate beam particles. The geometry and relative placement of the $BSCI$ scintillators are also used to define a "good beam particle" and to provide an afterprotection for the event acceptance decision and event readout periods. $BSCI1$ and $BSCI3$ have a "donut" shape, with a hole radius about the size of the target, and were utilized as veto counters. Signal in these counters means that a beam particle was not focused on the target. $BSCI2$ and $BSCI4$ define a "good" beam particle. In the analysis of this subsection we used only information from $BSCI2$ and $BSCI4$. These two detectors were equipped with fast Hamamatsu R2083 photomultipliers with a typical rise time of about 0.7 ns. Pulse height analysis of $BSCI$ signals may provide information about "double beam" events i.e. when two beam particles passed through the scintillator within the time resolution of the detector and

[1] Bicron BC-422, 0.5 mm thickness

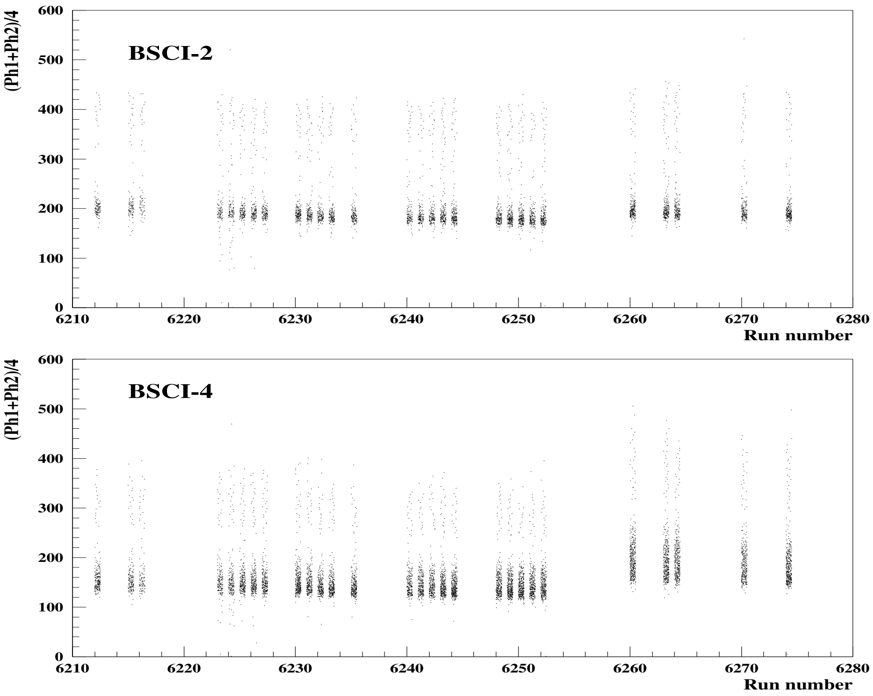

Figure 4.1: Pulse height (both phototubes combined) distribution in BSCI-2 and BSCI-4 as a function of run number. No cuts applied.

were accepted at the trigger level as one particle. In a case when both particles have interacted in the target such an event would have higher transverse energy deposition and possibly higher multiplicity than in the case of a normal event. Clearly, such events should be excluded from the analysis. Figure 4.1 shows combined pulse height distributions of signals from BSCIs as a function of run number. Figure 4.2 shows the correlation between the pulse heights in $BSCI2$ and $BSCI4$ as well as separate pulse height distributions from each

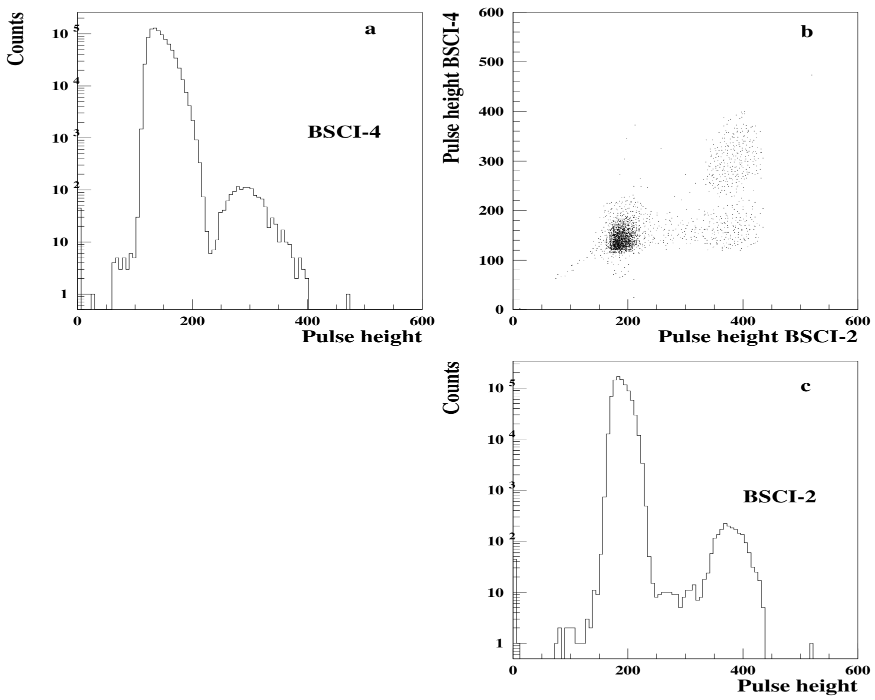

Figure 4.2: a - Pulse height distribution in $BSCI4$, b - Pulse height correlation between $BSCI2$ and $BSCI4$, c - Pulse height distribution in $BSCI2$.

detector [2]. One can clearly see double beam bands in both Figures 4.2 and 4.1. Another interesting feature which can be seen on Figure 4.2b is an almost total absence of events with one beam particle hit in $BSCI2$ and a double or higher hit in $BSCI4$. Such a combination may occur due to interactions in the upstream detectors themselves. Figure 4.3 shows, on the upper panel, the correlation between transverse energy detected in Participant Calorimeter and Target Calorimeter for the events with the large signal amplitude in either the $BSCI2$ or $BSCI4$ detector.

4.3 Beam Vertex Detectors

Incident beam trajectories before the target are measured by silicon microstrip Beam VERtex detectors($BVER's$) with 50 μm spatial resolution. These determine the incident angle of beam particles with an angular resolution of about 20 μrad in the xz -plane. The thickness of the detector was 200 μm. In Figure 3.6 they are denoted as $BVer1$ and $BVer2$. The number of hit clusters in the $BVERs$ may also be used for "double beam" and "upstream interaction" suppression. Another special situation may occur when one or both $BVERs$ have no hits detected due to inefficiency, "hot channels" subtraction or any other reason. In such a situation no incident beam angle can

[2] In order to avoid smearing a pulse height distribution, due to the global shift in a BSCIs pulse amplitude after run 6252 (see Figure 4.1) , we didn't use these runs to generate Figure 4.2. This trick creates a more visible separation between single and double hit peaks.

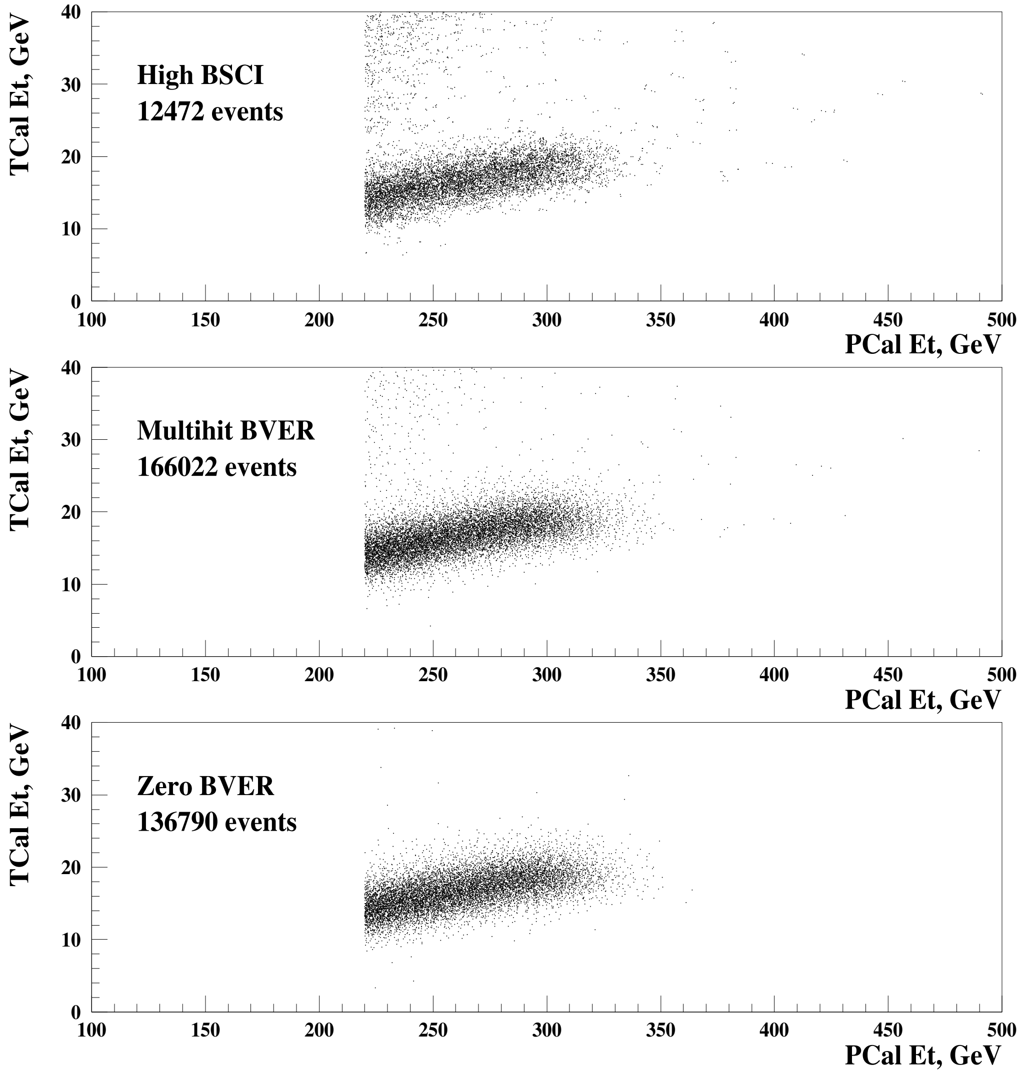

Figure 4.3: Upper: Transverse energy correlation for events with a high signal in either of the $BSCI$ detectors, Middle: Transverse energy correlation for events with multiple hit clusters in either of the $BVER$ detectors, Lower: Transverse energy correlation for events with no hit clusters in the $BVER$s.

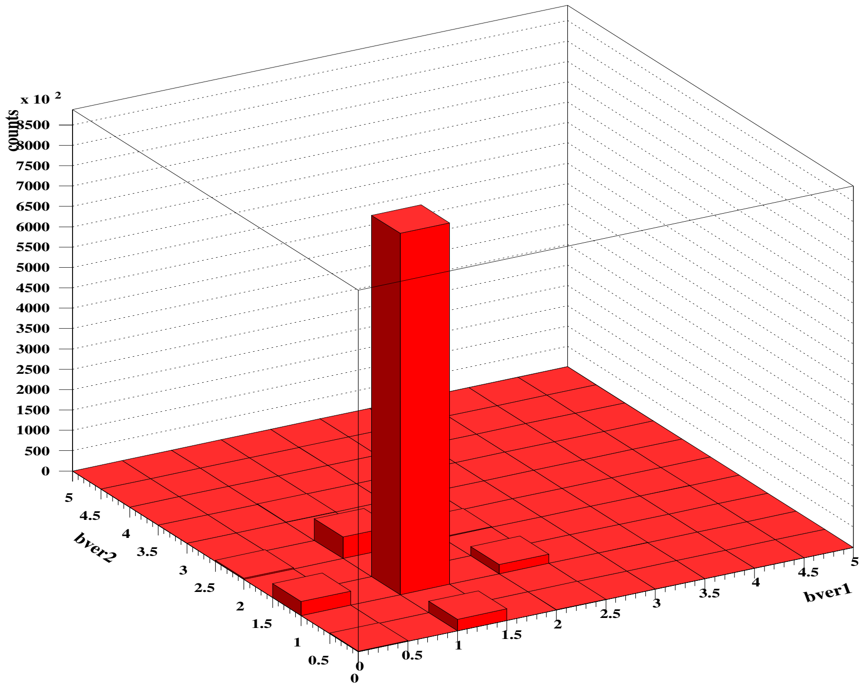

Figure 4.4: Number of hit clusters detected in $BVER1$ versus number of clusters in $BVER2$.

be restored directly from $BVER$ information and one should perform some special procedure to reasonably guess this angle if it has been decided that otherwise such an event was acceptable and should be included into the analysis. Figure 4.4 shows the correlation between the number of hit clusters in $BVER1$ versus $BVER2$. Table 4.1 includes the numeric values of the average hit cluster multiplicity per event in $BVER1$ and $BVER2$. Figure 4.3 shows, on the middle panel, the correlation between transverse energy detected in the Participant Calorimeter and Target Calorimeter for events with several clusters (multihit) in either of $BVER$ detectors. It is interesting to see that for

Number of clusters	*BVER1*	*BVER2*
0	0.038	0.03
1	0.94	0.91
2	0.022	0.06
> 3	< 0.0003	< 0.001

Table 4.1: Average number of clusters per event in $BVER1$ and $BVER2$.

events with zero BVER clusters, Figure 4.3 lower panel, there is no significant contribution in the very high transverse energy region.

4.4 Upstream Silicon Detector

The upstream SILIcon Detector ($SILI$) is a semiconductor detector located before the target. It is used to confirm the beam particle and suppress upstream interactions and double beam events. Due to radiation damage and subsequent detector performance deterioration, several units were changed during the run. Typically they had a round shape with a 200 mm^2 sensitive area, 87 μm sensitive depth and 100 μm thickness. On Figure 3.6 this detector is denoted as Si Detector. Figure 4.5 shows the pulse height distribution

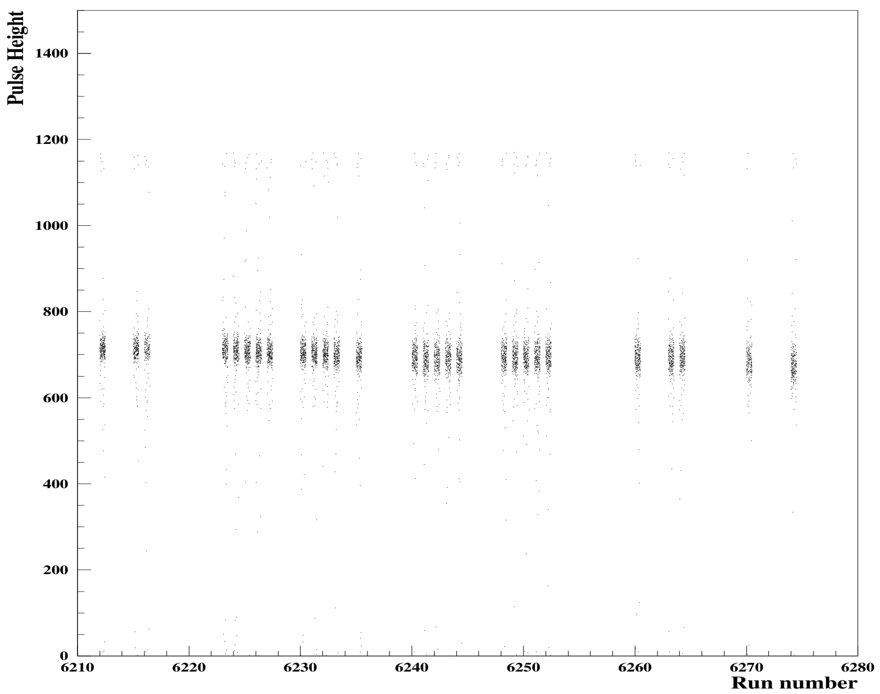

Figure 4.5: Pulse height in $SILI$ as a function of run.

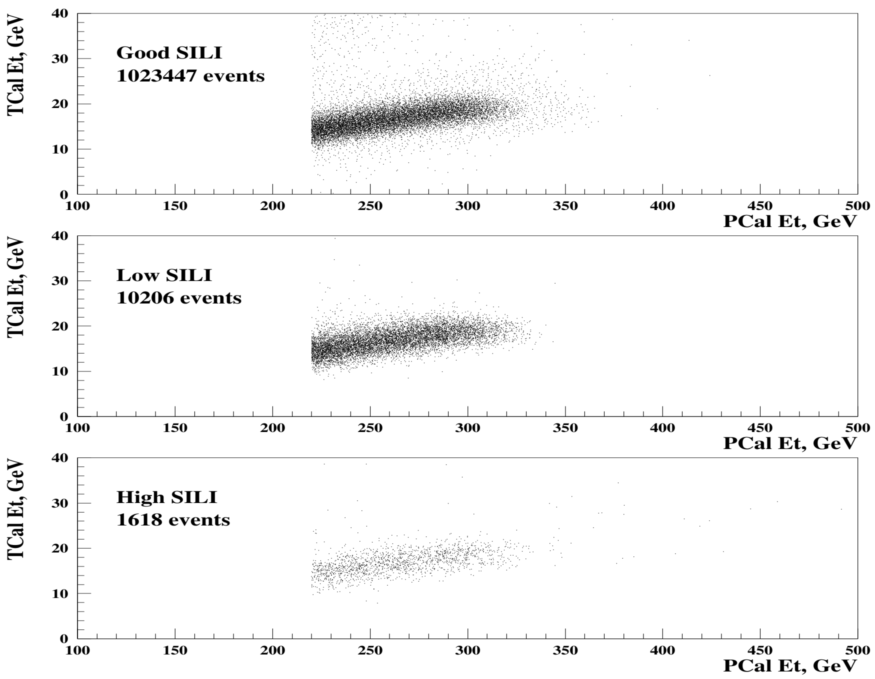

Figure 4.6: Transverse energy deposition in TCal and PCal for events with different ranges of the signal in $SILI$.

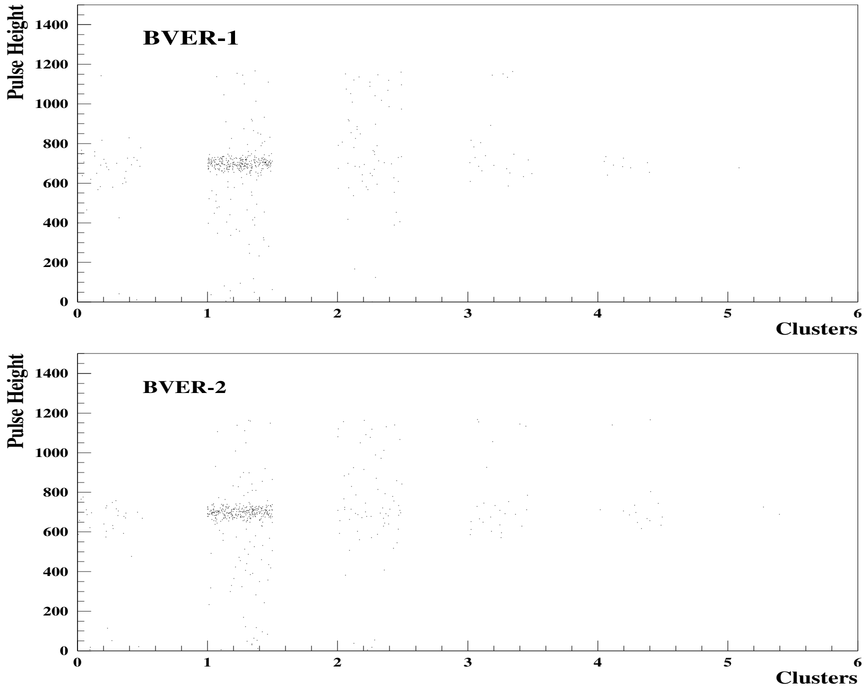

Figure 4.7: Correlation between pulse height in $SILI$ and number of clusters in $BVER$s.

in $SILI$ as a function of run number. We have applied both low and high cuts on the upstream silicon detector signal. It is interesting to see how the pulse amplitude in $SILI$ is correlated with the transverse energy production detected by E877 calorimeters. One would generally expect that for events with a high amplitude in $SILI$ (double beam, upstream interactions) the transverse energy will be higher than average one for a "normal" $SILI$ signal. Figure 4.6 shows the correlation between transverse energy detected by the participant calorimeter ($PCal$) and target calorimeter ($TCal$) for three ranges of $SILI$ signal amplitude. As can be seen from the "good SILI" panel of Figure 4.6 this requirement does not eliminate the very high transverse energy component in the $TCal$. On the "high SILI" panel of Figure 4.6 one can see that the cut has little or no influence on the suppression of high transverse energy deposited in the $PCal$ and $TCal$. That leads us to conclusion that "high SILI" signal most likely means a second beam particle which passed without an interaction along with the interacted one. "Low SILI" cuts show, as well, no significant sensitivity to the very high transverse energy production in both calorimeters. Figure 4.7 shows the correlation between the pulse height in $SILI$ and the number of hit clusters in both $BVERs$. Here one can see that a high number of clusters in $BVERs$ is related with "good" and "high" $SILI$ ranges.

4.5 "Good Beam Particle" Requirements

A set of simple requirements was applied in this analysis in order to select events with a "good beam particle" definition. Based on the results discussed in previous sections, we defined several failure modes. The beam particle was considered to be ill-defined if :

- The pulse height in $BSCI$ or $SILI$ was outside a predefined window
- The number of hits in both[3] $BVER$s was not equal to one.

Each failure mode was assigned a numeric value and the final failure flag for the event was a sum of all modes. The flag for a properly defined beam particle was assigned to be zero. Figure 4.8 shows a final flag distribution for all analyzed events. Out of 2070542 events with reconstructed tracks 318732 (15.4%) failed our requirements. One can see that the main reasons of failure (flags 32 and 64 in Figure 4.8) are related to the performance of the Silicon Detector. 126982 events (6.1%) had zero $BVER$ and 151342 (7.3%) events had multiple hit clusters in $BVER$. Figure 4.9 shows the correlation in

[3]The later requirement is necessary for the accurate definition of the beam particle angle of incidence on the target.In the case of one BVER missing one can try to guess the angle using information about average angle of the beam particles in several previous events with good BVER information. This method is based on the assumption that the average angle of the beam particles varies monotonically during the spill. We did not used this method in the current analysis. Events without hits in BVERs were simply excluded.

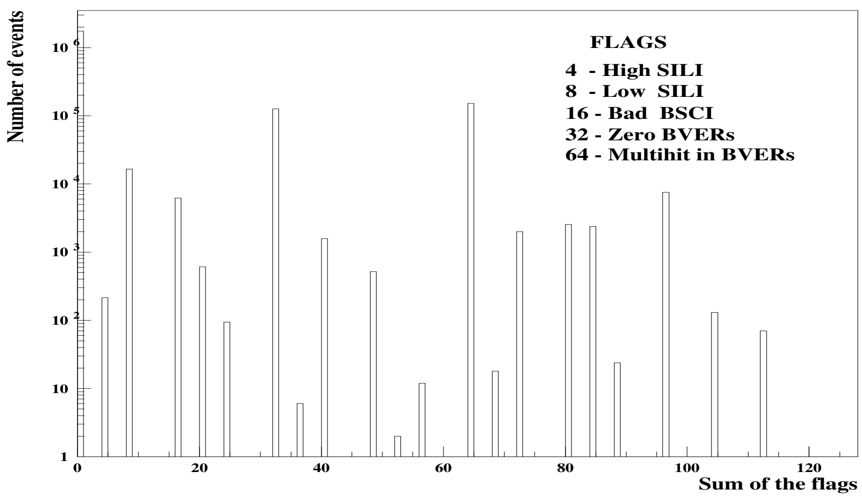

Figure 4.8: Event selection failure flags

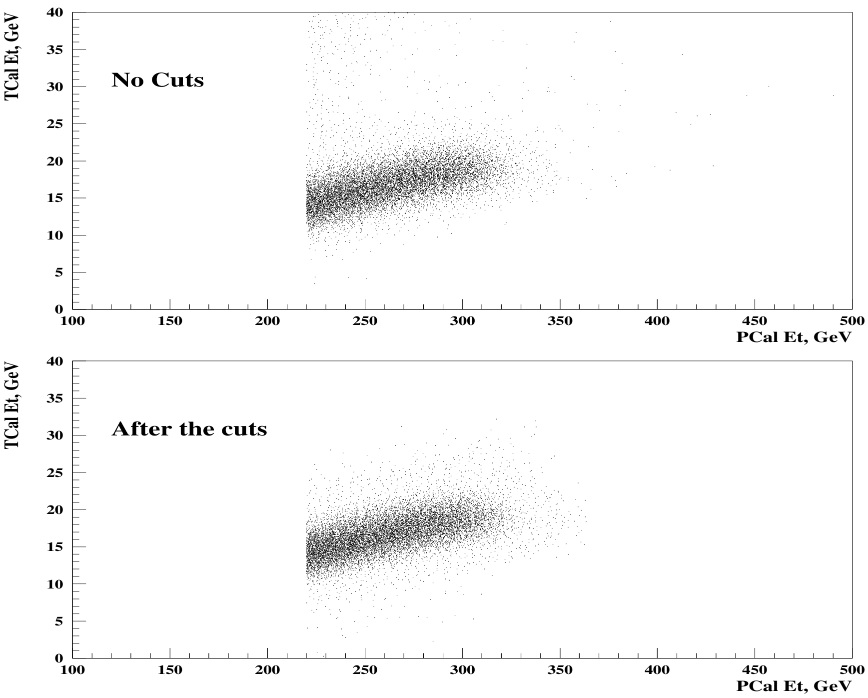

Figure 4.9: Correlation between transverse energy detected in the TCal and PCal before and after applying event selection cuts.

transverse energy detected in the TCal or PCal calorimeters before and after applying the event selection requirements mentioned above. One can see that in the resulting transverse energy distribution (after the cuts) the events with a very high deposition in either detector are effectively suppressed.

The approach described in this section was implemented as an event selection routine in a framework of the E877 STEP2 offline software, which allowed a unified analysis procedure for the 93, 94 and 95 Au+Au runs within the collaboration and thus greatly simplified comparisons of similar analysis made by different groups.

Chapter 5

Particle Identification

Simultaneous measurements of the particle's momentum and time of flight in the spectrometer provided identification of the particle's species. In this section we will discuss issues involved in the track reconstruction and track selection.

5.1 Track Reconstruction

The trajectories of the charged particles emitted from the target into the opening of the collimator were bent by the magnetic field of the dipole magnet. The hits in the drift chambers (and, for the E877 setup, the set of multiwire proportional chambers- MWPC's) positioned downstream from the magnet were used to reconstruct the track trajectory. The pattern recognition program was based on a "tree" algorithm [44]. The advantage of this algorithm is that it can effectively resolve the left-right ambiguity while finding segments in the drift chambers. After segments in the drift chambers are reconstructed the pattern recognition routine attempts to build tracks using additional information from other detectors if necessary, in particular information about the hits in the time of flight walls and (when available) from MWPC's. After tracks are reconstructed downstream from the magnet they are projected back to the target. In this process, we assume that tracks originated from the target. A simplified "box" model of the magnetic field with the field integral Bdl equivalent to that measured is also used[1] in this procedure. Completely reconstructed tracks were written out as a part of the standard E877 ntuple along with "global" event information. The data structure associated with every reconstructed track has 35 variables containing the information from all detectors in which this track was registered along with some diagnostic information from the pattern recognition routine. This allows track selection and rejection cuts on the later stages of analysis on various parameters of the track.

5.2 Track Selection

Further cuts and selection criteria were imposed on the reconstructed tracks. In the present analysis of Au+Au data we have chosen to apply the same cuts that were used in single particle analysis of pions and proton spectra. This allowed us to unify software acceptances (fiducial cuts) of both analysis and interpret the information obtained from the single particle analysis and

[1] In order to improve tracking reconstruction, two multiwire chambers were installed before the magnet during 1994 and 1995 runs. They were not used in the analysis presented in this thesis.

two-particle analysis more transparently and consistently.

A cut on a pulse height in the TOFU slat associated with the track was applied for all tracks. All TOFU slats amplitude spectra have been normalized in such a way that the peak of a minimum ionizing particle (MIPS) was assigned to be at amplitude 1. Tracks were required to have an amplitude between 0.8 and 1.50. Figure 5.1 presents a typical calibrated TOFU amplitude spectrum along with the single charge cuts.

5.3 Software Acceptance Cuts

Most of the cuts were related the so called “soft collimator” or “software acceptance” which is a set of geometrical cuts inside the volume of the spectrometer. The trajectories of the “good” tracks should satisfy the following requirements:

- Pass not too close to the walls of the collimator
- Pass not too close to the dead regions of the tracking chambers and TOFU.
- Fit into the vertical and horizontal boundaries of the fiducial surface of the tracking chambers.
- Not be associated with dead or malfunctioned slats of the TOF hodoscopes

A collection of cuts has been implemented in a routine called TRIVIAC which became a standard part of the E877 offline analysis procedure. This approach

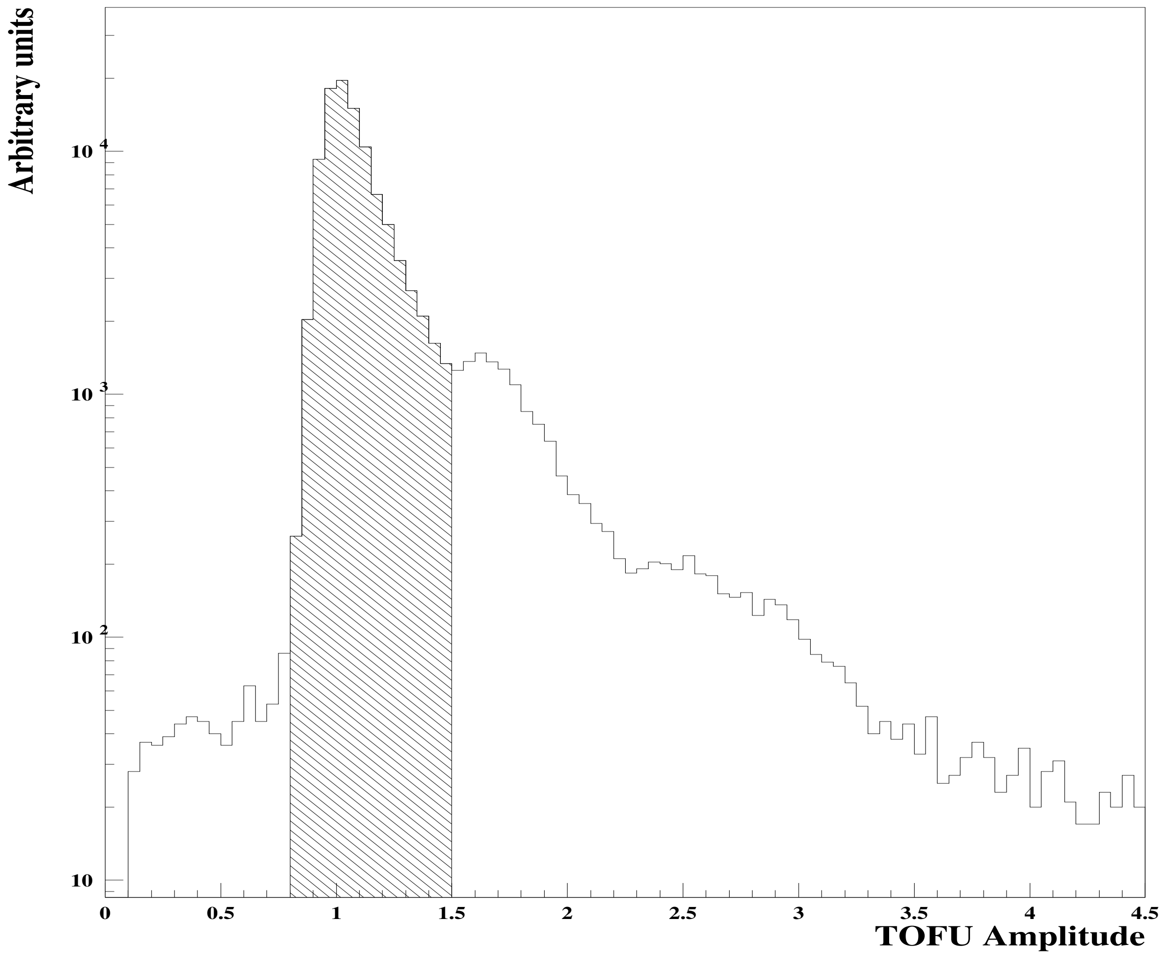

Figure 5.1: Typical calibrated TOFU amplitude spectrum. Shaded area shows single charge selection region.

Cut	Fraction of rejected tracks
Maximum momentum cut	27%
Collimator cut in X	16.5%
Collimator cut in y	22.4%
Fiducial cut in DC's	1.8%
Dead regions in DC's	13.5%
Dead regions in PC's	1.2%
Bad TOFU slat	17.4%

Table 5.1: Fraction of the rejected tracks per single track cut.

turned out to be very useful in Monte Carlo simulations of the correlation functions beacause it allowed the application of exactly the same geometrical cuts to the model as to the single particle distributions in the data.

5.4 Particle Identification

After determination of the particle momentum and time of flight we can determine the mass of the particle using the following relationship between mass and momentum[2]:

$$m = \frac{p}{\beta\gamma} = \frac{p\sqrt{(1-\beta^2)}}{\beta}. \tag{5.1}$$

Lorentz factor β can be expressed using the measured time of flight -T_{meas} and the measured length L of the particle's trajectory.

$$\beta = \frac{L}{T_{meas}} \tag{5.2}$$

The relationship between the particle mass and the measured values can be expressed in the form convenient for use in the particle identification procedure:

$$m^2 = p^2\left[\left(\frac{1}{\beta}\right)^2 - 1\right] \tag{5.3}$$

The width of the mass squared peak as a function of momentum is determined by the momentum resolution of the spectrometer and the resolution of the time of flight system. It is straightforward to express the dispersion of m^2 as a function of momentum resolution σ_p and time of flight resolution σ_T. Using

[2]We will use units where speed of light is equal to 1.

equation 5.3 (and neglecting the dispersion of the particle trajectory length L in equation 5.2) one can write:

$$\sigma^2_{m^2} = 4\frac{m^4}{p^2}\sigma^2_p + 4p^4\frac{1}{\beta^2}\sigma^2_T \tag{5.4}$$

It has been shown in [52, 56] that the momentum resolution of the E877 spectrometer can be expressed in the following form

$$\sigma^2_p = C_1 p^4 + C_2 p^2 \left(\frac{1}{\beta}\right)^2, \tag{5.5}$$

where C_1 and C_2 are coefficients determined by the properties of the spectrometer. C_1 can be related to the position resolution of the tracking chambers and the integral of the magnetic field and is assumed to be constant for all particles. C_2 is determined by the materials of the spectrometer and reflects contributions from multiple scattering to the momentum resolution. It is also a constant for all single charged particles. After substituting equation 5.5 into equation 5.4 and also expressing $\beta = p/\sqrt{p^2 + m_0^2}$, where m_0 is an assumed mass of the particle, one can write the dispersion of m^2 as a function of momentum in the following form:

$$\sigma^2_{m^2} = C_1 \cdot 4\frac{m_0^4}{p^2} + C_2 \cdot 4m^4(1 + \frac{m_0^2}{p^2}) + C_3 \cdot (4p^2(m_0^2 + p^2)) \tag{5.6}$$

where coefficient C_3 is proportional to the ratio of the time of flight resolution and the length of the particle trajectory squared.

The values of the coefficients C_1, C_2, C_3 can be determined from the fit to the experimentally measured width of the mass peak . Figure 5.2 shows the width of the mass peaks as a function of the particle momentum as well as

particle	C_1	C_2	C_3
proton	0.0024	0.0298±0.0001	0.00218±0.00001
deuteron	0.0024	0.0273±0.0004	0.00194±0.00005

Table 5.2: Coefficients of the mass squared width parameterization extracted from the fit to the data.

the fitted curves based on Equation 5.6. Data from the 1994 Au+Au run were used. The value of C_1 was calculated according to the method suggested in [56] and was kept fixed during the fit. Values of the coefficients extracted from the fit to the proton and deuteron peaks are presented in Table 5.2. Equation 5.6 has a form convenient for particle identification and allows one to specify cuts based on the mass peak dispersion for a given momentum. Figure 5.3 shows the typical measured mass distributions in different momentum intervals for single-charged positive particles. A cut of 1.5σ on the mass squared peak[3]was

[3]It was estimated, in reference [57], that for 2.5σ mass square cut, the contamination of the proton sample is less than 2%. As a part of a standard analysis check the two-proton correlation function was obtained for different mass cuts in the particle identification routine. In this way one can check the influence of the "background" or misidentified particles on the correlation function. It was found that within the range of reasonable choice of the cuts, from one to two standard deviations, this cut has no influence on the correlation function.

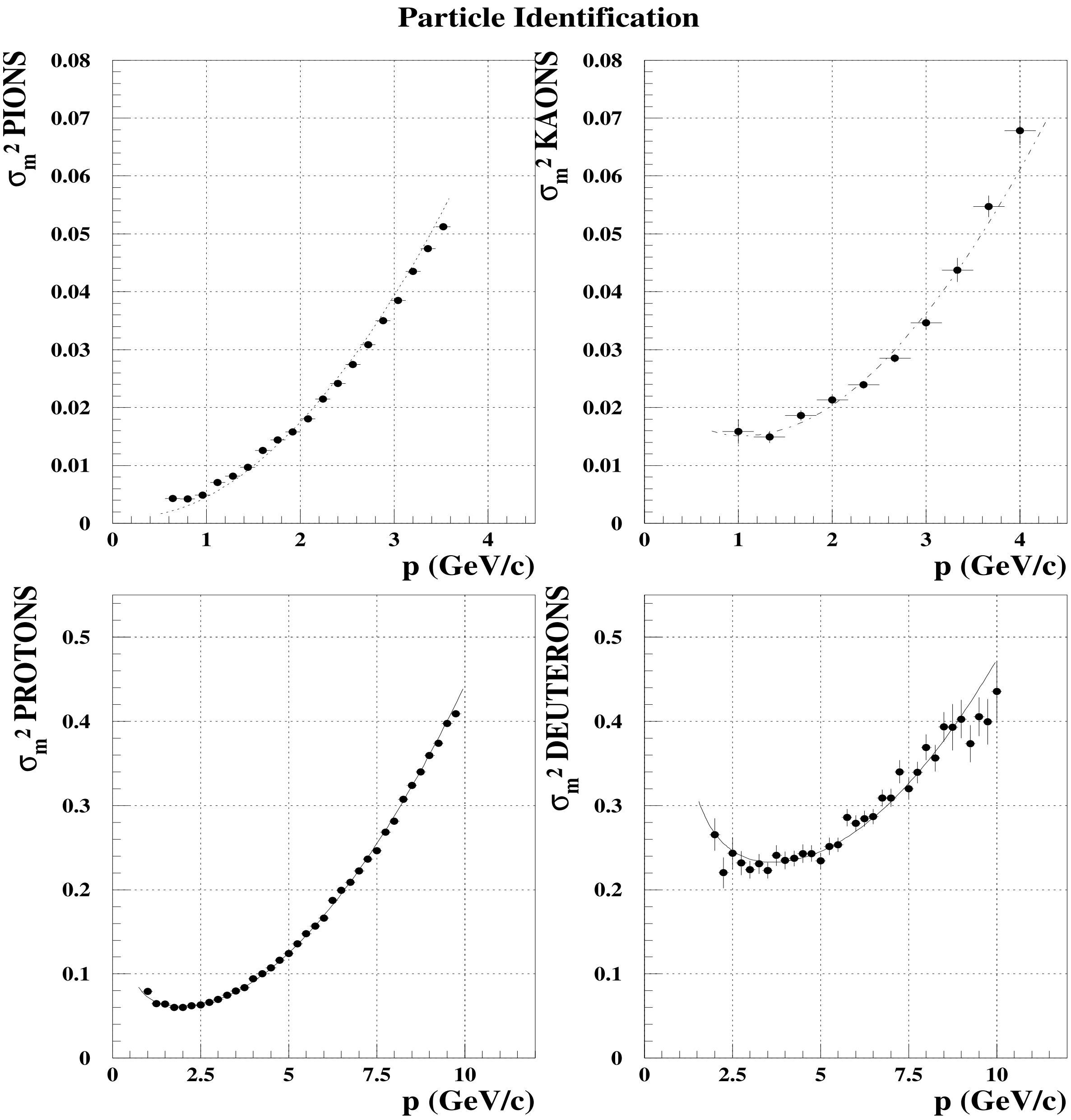

Figure 5.2: Fit to the width of the mass squared peak as a function of momentum for different particles. Functional form 5.6 with fixed C1 was used.

applied. It can be clearly seen that E877 provides excellent mass resolution and particle identification capabilities.

We conclude that protons can be clearly identified up to 10 GeV/c, while pions as well as kaons can be reliably resolved up to a momentum of 4 GeV/c. Deuterons can be identified up to 20 GeV/c except in the momentum region from about 10 GeV/c to 12 GeV/c where protons and deuterons can not be resolved. Above 12 GeV/c we considered the contribution of protons to the deuteron yield to be negligible.

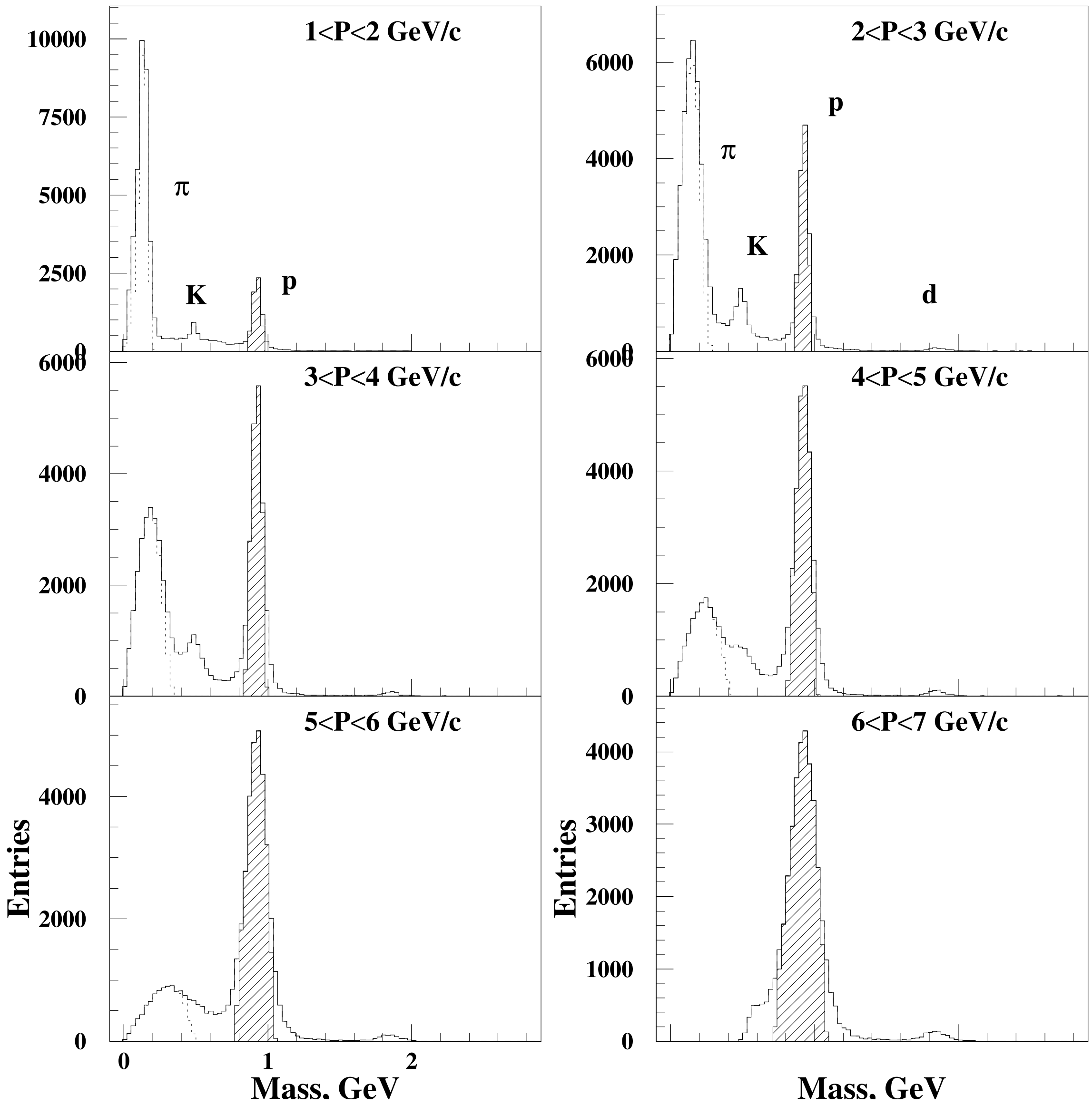

Figure 5.3: Measured mass distributions for different momentum intervals. Shaded area shows protons identified by the particle identification routine. See description in the text.

Chapter 6

Two-Particle Correlations

6.1 Experimental Definitions

The experimental correlation function C_2 is defined as:

$$C_2(P_{cm}) = \frac{N_{tr}(P_{cm})}{N_{bk}(P_{cm})} \tag{6.1}$$

where P_{cm} is the momentum difference of the pair in the pair's rest frame; N_{tr} is the number of pairs in a given P_{cm} bin which came from the same event; and N_{bk} is a number of pairs obtained from different events (see a detailed description in the next section).

For the pairs of the same mass P_{cm} is equal to the four-momentum difference,

$$P_{cm} = Q_{inv} = \sqrt{-(p_1^{\mu} - p_2^{\mu})^2}, \tag{6.2}$$

while for particles with different masses

$$P_{cm} = \sqrt{Q_{inv}^2 + \left(\frac{m_1^2 - m_2^2}{M_{inv}}\right)^2} \tag{6.3}$$

where m_1, m_2 are the particle masses and M_{inv} is the invariant mass of the pair. The conventional variable for two-proton correlation studies is $q_{inv} = \frac{1}{2}Q_{inv}$.

6.2 Mixed Event Background

The "background" distribution, N_{bk}, was obtained using an event mixing method; a single proton was randomly selected from one event and then combined with another proton selected from a different, randomly selected event. The large statistics of the N_{bk} distribution ensures that the major contribution to the statistical errors in the correlation function comes from the statistics of the true proton pairs.

A requirement that the two protons did not share the same slat of the TOF hodoscope has been imposed on pairs from both distributions. Cuts on separation between two track hits in the drift chambers have also been applied on pairs from both distributions. These cuts are discussed in details in the next section.

By studying the distributions N_{tr} and N_{bk} as a function of q_{inv}, we found that the "background" spectrum N_{bk} has the same shape as the true spectrum N_{tr} for $q_{inv} > 100$ MeV/c; Figure 6.1 shows a typical shape of both distributions. The background distribution was normalized to the total number of entries in the true distribution within the range $100 < q_{inv} < 1000$ MeV/c.

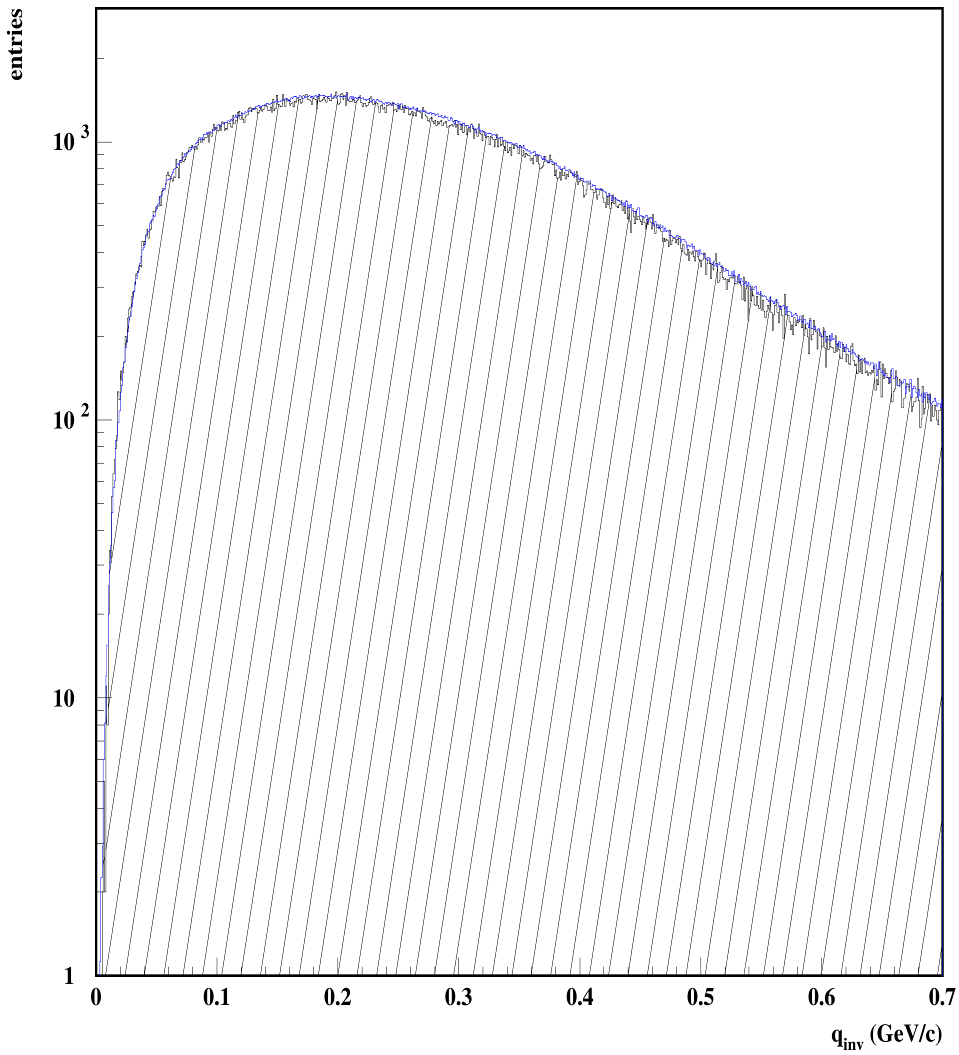

Figure 6.1: True (solid shaded histogram) and normalized background (dashed histogram) distributions.

6.3 Momentum Resolution

We will argue in this section that it is important to know the properties of the momentum resolution so that it can be included into the model calculations. The simulated correlation function will be distorted by a finite momentum resolution of the spectrometer, similar to the experimentally measured correlation function. The q_{inv} resolution is completely determined by the momentum resolution of the apparatus. When the momentum resolution of the spectrometer is known, the determination of the relative invariant momentum resolution is a straightforward algebraic exercise. The results of this exercise are presented in Appendix E.

As we have mentioned in Chapter 5, the question of the momentum resolution can be addressed and cross-checked in several ways.

6.3.1 GEANT Based Studies

The standard approach is to use the GEANT simulation package [45], a "de-facto" standard in high-energy and nuclear physics. It provides a comprehensive framework for realistic simulations of the experimental setup. Provided with a "realistic" model of the particle source and detailed description of the geometry and materials of the apparatus, GEANT serves as a powerful aid in understanding the properties of the experimental setup. Calculations[1] based

[1]The discussion in this section is largely based on the work done by C.M. Zou on the E877 GEANT model and by Y. Kwon on the GEANT interface with the E877

on the GEANT package interfaced with E877 tracking software [52], yielded a relative momentum resolution ($\delta p/p$) of protons and pions of 2.2% and 2.5% respectively for the momentum range of 2 to 10 GeV/c.

6.3.2 Semi-analytical Approach

In Reference [55] an analytical method of calculating the momentum covariance matrix for the multi-plane tracking systems was proposed. This method employs direct calculations of the covariance matrix elements based on knowledge of the multiple scattering properties of the material of the detector as well as on the resolution of the detecting planes. This method[2] allowed the expression of all elements of the momentum covariance matrix as analytical functions of momentum and properties of the spectrometer. Note that, in our model calculation, we have used a routine based on this approach for simulating the momentum resolution of the E877 spectrometer.

It has been shown [56] that this routine is in good agreement with GEANT Monte Carlo simulation. The calculated resolution is also in a good agreement with the measured width of the mass peaks of various particle species (see Chapter 5 or [58] for more details).

Analitical calculations of the momentum resolution of the E814 spectrometer were done, in a similar spirit, in Reference [62] where it was stated to be

---

tracking software, from which we have greately benefited.

[2]For more details see E877 Collaboration memo by D. Miskowiec [56]

described by the parametrization $\delta p/p \approx 4.8\%/\beta$.

6.3.3 Resolution in q_{inv}

The invariant relative momentum resolution for the E814 Spectrometer, found from Monte Carlo studies [63], was etimated to be on the order of 11 MeV/c for $q_{inv} \leq$ 40MeV/c (the most sensitive region for the correlation measurement).

The q_{inv} resolution of the E877 Spectrometer was estimated to be on order of 5 to 10 MeV/c for $q_{inv} \leq$ 40MeV/c depending on the year of the run. For the 1994 run, the resolution was better then in 1993 due to the increase in the amount of helium in the forward spectrometer which subsequently reduced the multiple scattering (see Chapter 3).

For the 1993 and 1994 data sets we have used histograms with 7 MeV/c bin width for the presentation of our data. During the ntuple scanning phase, data were filled into the histograms with 1 MeV/c bins, which later can be rebinned into any appropriate bin width. The 7 MeV/c bin was found to be the optimum compromise between q_{inv} resolution and statistics within the bins in the low q_{inv} region.

6.4 Two-Track Efficiency

Finite segmentation, high occupancy of detectors and imperfections of the tracking code are among the factors that lead to the losses of pairs with small relative momentum. As the separation between two tracks in the detector becomes smaller and smaller, the probability that the detector will register hits from both tracks correctly becomes smaller and smaller. Accordingly, the probability of reconstruction of the correct track by the tracking software diminishes. Such losses inevitably occur in any detector and lead to distortions in the shape of the measured two particle correlation function. In order to illustrate the point, Figure 6.2 shows the distribution of two proton relative separation in DC2 and DC3 for both "true" and "mixed" pairs as well as the ratio of these distributions. The ratio was obtained by division of the "true" distribution on a normalized "mixed" distribution. It can be clearly seen that "true" and "mixed" distributions have very different shapes at small separations. Figure 6.3 shows the two-track separation in both chambers as a function of q_{inv}.

6.4.1 Typical Scales

In general, one would expect that the described effects become significant when the distance between two tracks is less than some typical granularity scale of the detector. In the drift chambers the distance between signal wires, or the drift cell size, suggests a natural unit for such a scale. The distance between signal wires in each tracking plane[3] is equal to 6.35 mm in DC2 and 12.7 mm in DC3. From the distributions shown on Figure 6.3, it is evident that

[3]Each drift chamber used in the E877 apparatus has 6 independent wire planes, with wires in every neighboring plane staggered by half of the drift cell size. See Chapter 3.

distortions due to the two-track reconstruction inefficiencies become important when the distance between two tracks becomes approximately less than the size of two drift cells.

The distance between two tracks in the drift chambers and q_{inv} are related. The visible diagonal cutoffs on Figure 6.3 suggests a correlation between the q_{inv} and the distance between two hits in the detector. One can use a simple model in order to understand the typical track separation scale in the E877 spectrometer. Let us consider a particle with momentum $\vec{P} = (p, \theta_0, \phi)$. In a small angle and single bend approximation one can show that the position of the hits in DC2 and DC3 can be expressed as:

$$X_{DC2} = \frac{0.3BL}{P} Z_2 + (Z_1 + Z_2)\,\theta_0 \tag{6.4}$$

$$X_{DC3} = \frac{0.3BL}{P} (Z_2 + Z_3) + (Z_1 + Z_2 + Z_3)\,\theta_0 \tag{6.5}$$

where BL is the magnetic field integral, Z_1 is the distance between the target and the center of the E877 magnet, Z_2 is the distance between the center of the magnet and DC2, and Z_3 is the distance between DC2 and DC3. As an example we will perform calculations for DC3. Note that $Z_1 + Z_2 + Z_3 \approx$ 11.6m . Then the distance D between two hits in DC3 can be expressed using Equation 6.5 as:

$$D = X_1 - X_2 = (Z_1 + Z_2 + Z_3)\,(\theta_1 - \theta_2) = (Z_1 + Z_2 + Z_3)\,\theta \tag{6.6}$$

where θ is the angle between the two particles. It is trivial to obtain a similar expression for DC2. We will assume further that particles have equal masses

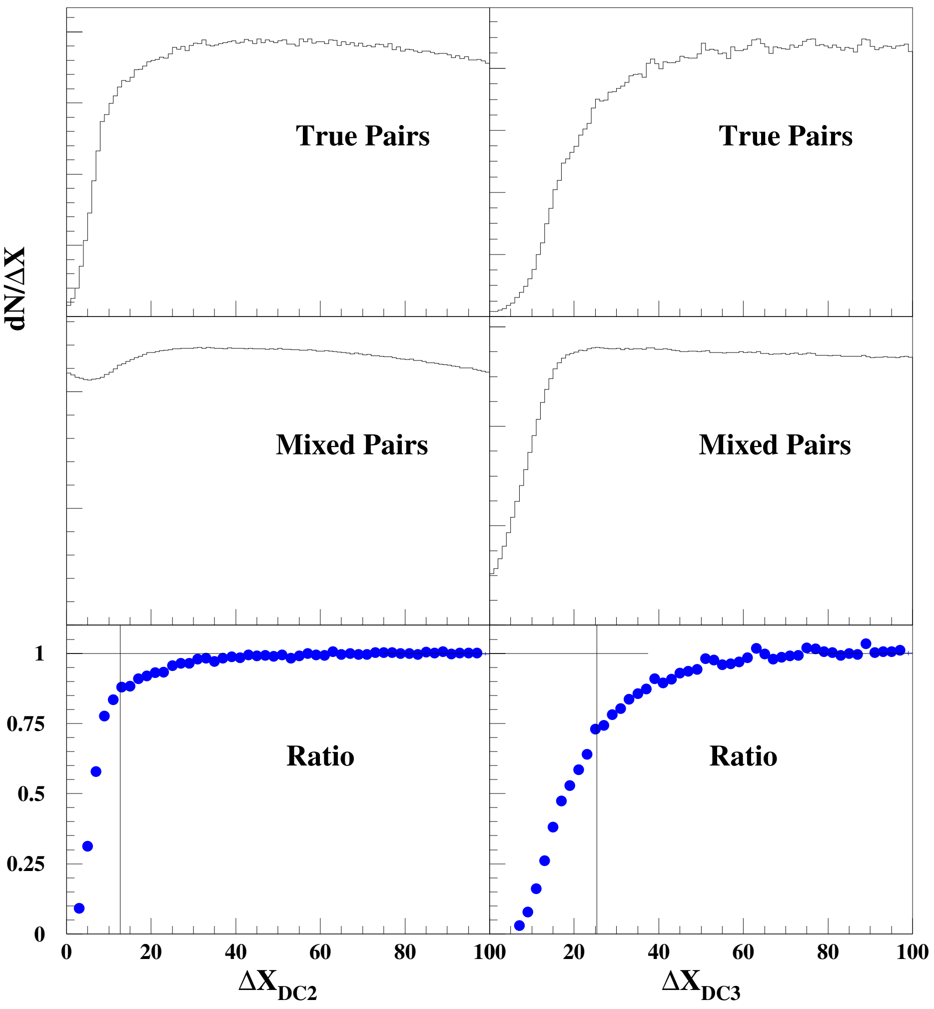

Figure 6.2: Two-track separation in DC3. Upper panels - true pairs, middle panels - mixed pairs, lower panels - ratio of true to normalized mixed distributions. Vertical lines on the lower panels show the size of the two drift sells in both drift chambers.

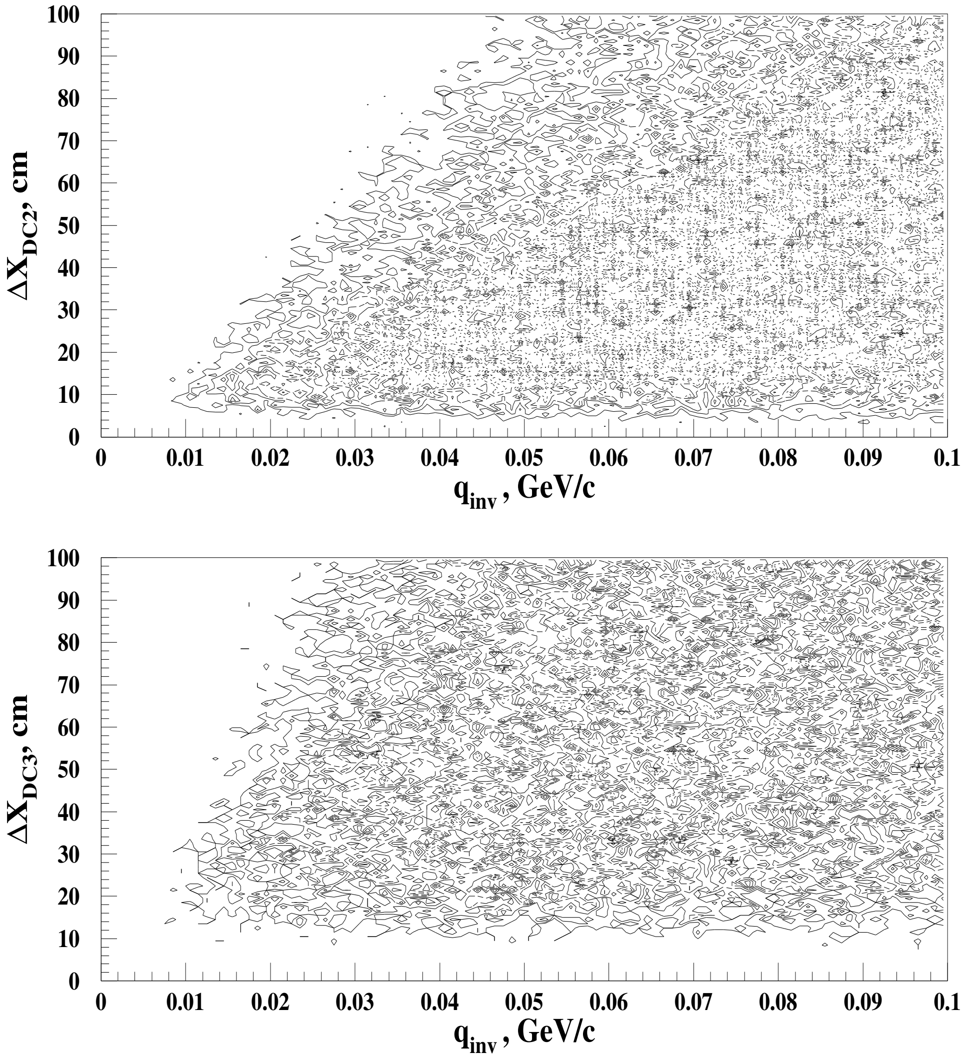

Figure 6.3: Two-track separation in DC2 and DC3 as a function of q_{inv}.

$m_1 = m_2$. In the equal momentum approximation $P_1 = P_2$, or equivalently ΔP$\ll$P, this assumption leads to the maximum separation between tracks with a given P and Q_{inv}.

In this approximation the relationship between Q_{inv} and the angle between two particles θ becomes rather simple:

$$Q_{inv}^2 = \left(\vec{p_1} - \vec{p_2}\right)^2 - \left(E_1 - E_2\right)^2 = 2p^2\left(1 - \cos\theta\right) \tag{6.7}$$

or

$$\theta = \arccos\left(1 - \left(\frac{Q_{inv}}{\sqrt{2}p}\right)^2\right). \tag{6.8}$$

Substituting this expression in to Equation 6.6 one can calculate the two-track separation for a given Q_{inv} and momentum. The results of the calculation are presented in the Table 6.1 for certain values of the parameters. We have chosen q_{inv} to be in the region of the maximum sensitivity of the proton correlation function. Figure 6.4 presents the separation in DC3 as a function of momentum and q_{inv}. The results in the table qualitatively agree with the position of the diagonal cutoff which can be seen on the lower panel of the Figure 6.3. The smearing of the cutoff line is due to multiple scattering.

6.4.2 Two-track Separation Cuts

To account for distortions of the correlation function introduced by two-track reconstruction inefficiencies in high multiplicity events, cuts on the separation of two tracks in the drift chambers were introduced. Figure 6.5 shows

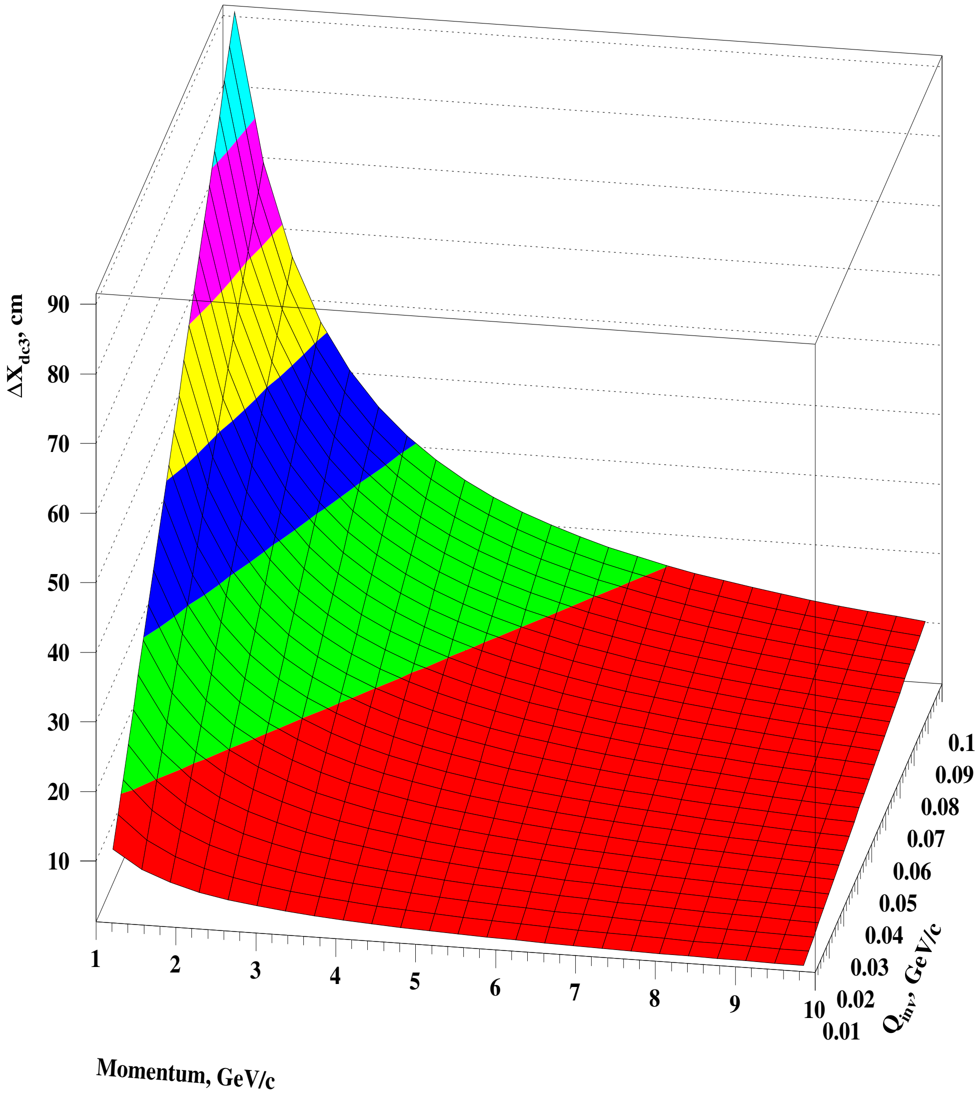

Figure 6.4: Track separation in DC3 as a function of momentum and q_{inv}. Equal momentum approximation was used. See description in the text.

the behavior of the first six bins (the most sensitive region of the correlation function) under the cut on the separation of two tracks in DC3. Each bin is 7 MeV/c wide and the q_{inv} value given on each panel refer to the center of the bin. It can be seen that the correlation function in every bin stops changing somewhere around the cut value of 20mm. Therefore the applied cut removes regions from both true and mixed distributions that are different from each other due to the two-track reconstruction inefficiencies. It can be seen, from the lower panel of Figure 6.3, that the cut suppresses only a small fraction of the existing statistics in the region of q_{inv} around 20 MeV/c. The 24 mm cut on track separation in DC3, along with 12 mm cut in DC2 was used for the analysis of Si+Pb and Au+Au data. Figure 7.3 suggests that after application of the two-track separation cuts the distortion in the ΔX spectra was corrected.

The size of the cut is not fixed exactly, though it should be closely related to the typical segmentation scale of the detector. The value of the cut is a tradeoff between the available statistics in the small relative momentum bins and the need to correct the distortion. Figure 10.4 illustrates the influence of different cuts on track separation on the shape of the correlation function. It's clear from the Figure that the shape of the correlation function in the peak area is fairly stable under the cut.

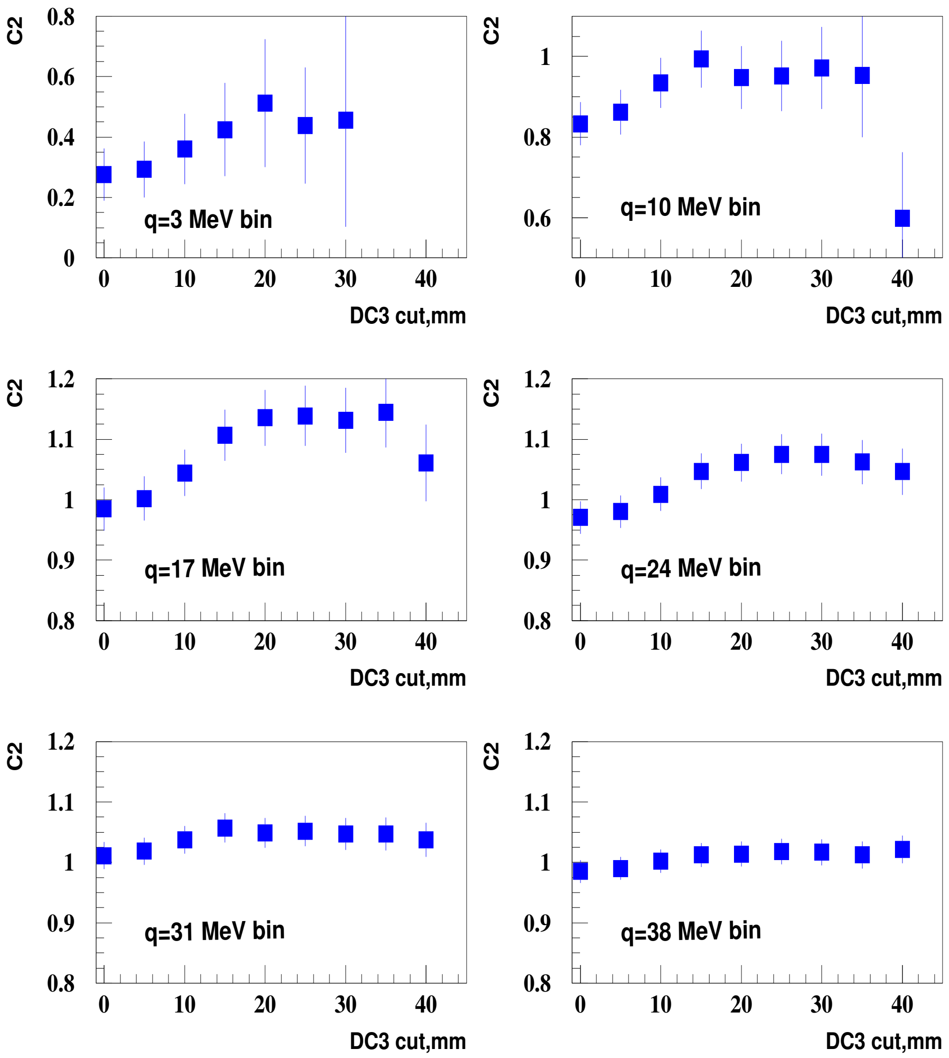

Figure 6.5: Correlation function in each of the bins as a function of the separation cut in DC3.

P, MeV/c	Q_{inv}, MeV/c	q_{inv} ,MeV/c	θ, rad	D, cm
9000	40	20	$4.44 \cdot 10^{-3}$	5.1
9000	20	10	$2.22 \cdot 10^{-3}$	2.6
7400	20	10	$2.70 \cdot 10^{-3}$	3.1
4000	20	10	$5.0 \cdot 10^{-3}$	5.8

Table 6.1: Two-track separation in DC3, calculated using 6.6, for a given momentum of the particle and q_{inv} of the pair. See description in the text

6.4.3 GEANT Simulations

Monte Carlo studies based on the GEANT [45] detector simulation package showed that the discussed cuts effectively suppress distortions due to close track reconstruction inefficiencies. In this study we tried to simulate the E877 spectrometer performance combined with the tracking software[4] efficiency under conditions similar to those in Au+Au collisions at 10.8 AGeV/c [52]. The advantage of this method is that it allows us to study the influence of both hardware and software factors on the two proton correlation function within the same framework. The drawbacks of this method are its computational

[4]The E877 tracking routine was called "Quanah", after the famous native American tracker, this name will appear on the figure titles in this subsection.

intensity and large demand for disk space which limits the available statistics.

6.4.4 The Simulated Environment

It was essential to understand the behavior of the spectrometer in the high track density environment when several different particles are being propagated through the apparatus. Initial transverse momentum and rapidity distributions of the particles "thrown in" to the apparatus were generated using the output of the RQMD 1.08 cascade code. Multiple scattering and hadronic interactions in the materials of the spectrometer were taken into account. Obtained hit banks were interfaced with the E877 tracking software and reconstructed tracks were used to generate the simulated correlation function in the same way as the real data analysis. Figure 6.6 shows the mass distribution of the successfully reconstructed particles. Figure 6.7 shows the reconstructed proton multiplicities before and after applying track selection cuts by the analysis routine. The idea of this approach was to construct the distortion function of the E877 spectrometer in q_{inv} space. The initial input has no two-particle correlations by definition, so under the ideal conditions one should expect the simulated correlation function to be consistent with unity. Any structures in the simulated correlation function will be due to imperfections of the spectrometer and tracking software. This "correlation function" can be used to correct the real correlation function. Also one can study the influence of the cuts introduced in the real data analysis and two-track sepa-

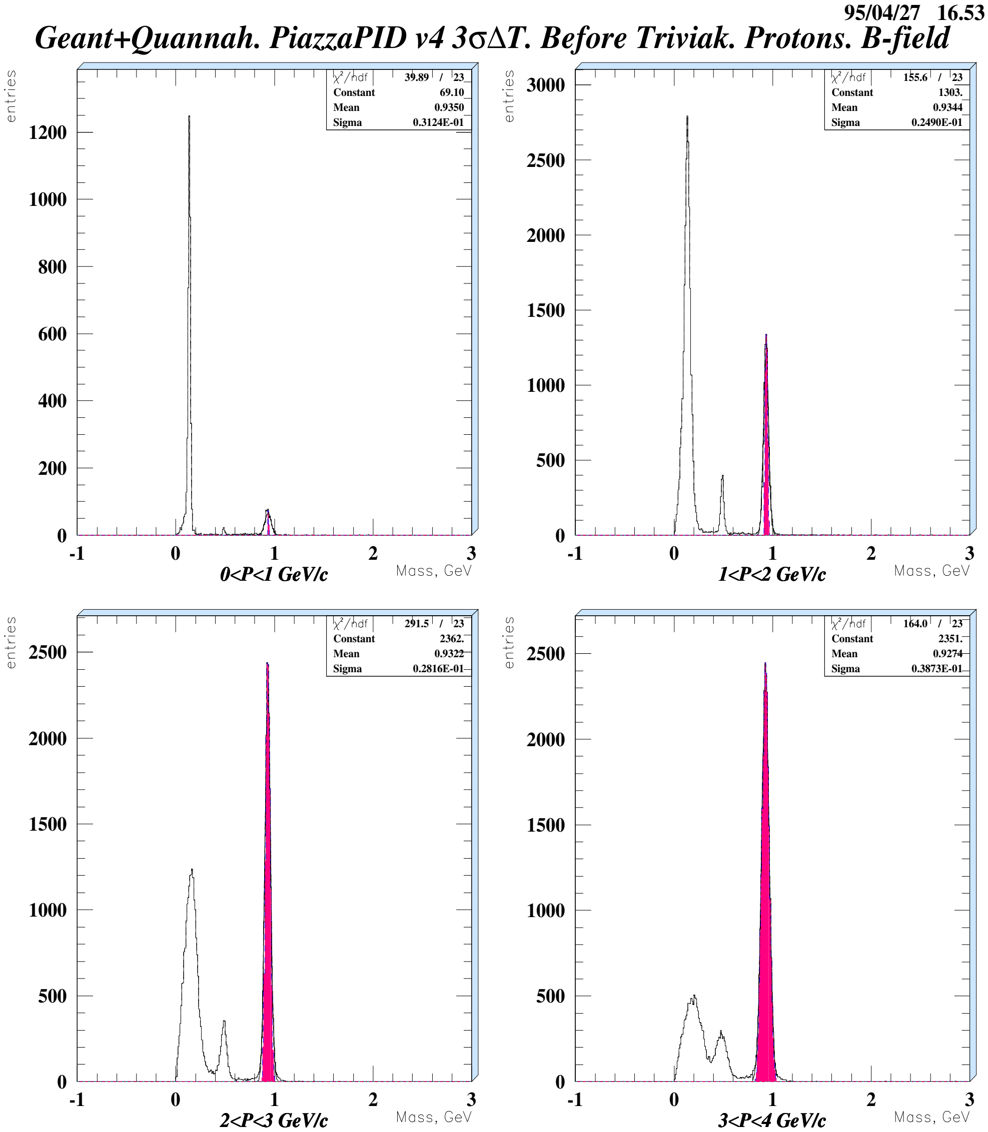

Figure 6.6: GEANT simulations.Mass distributions of the reconstructed particles. Shaded areas shows protons identified by the pid routine.

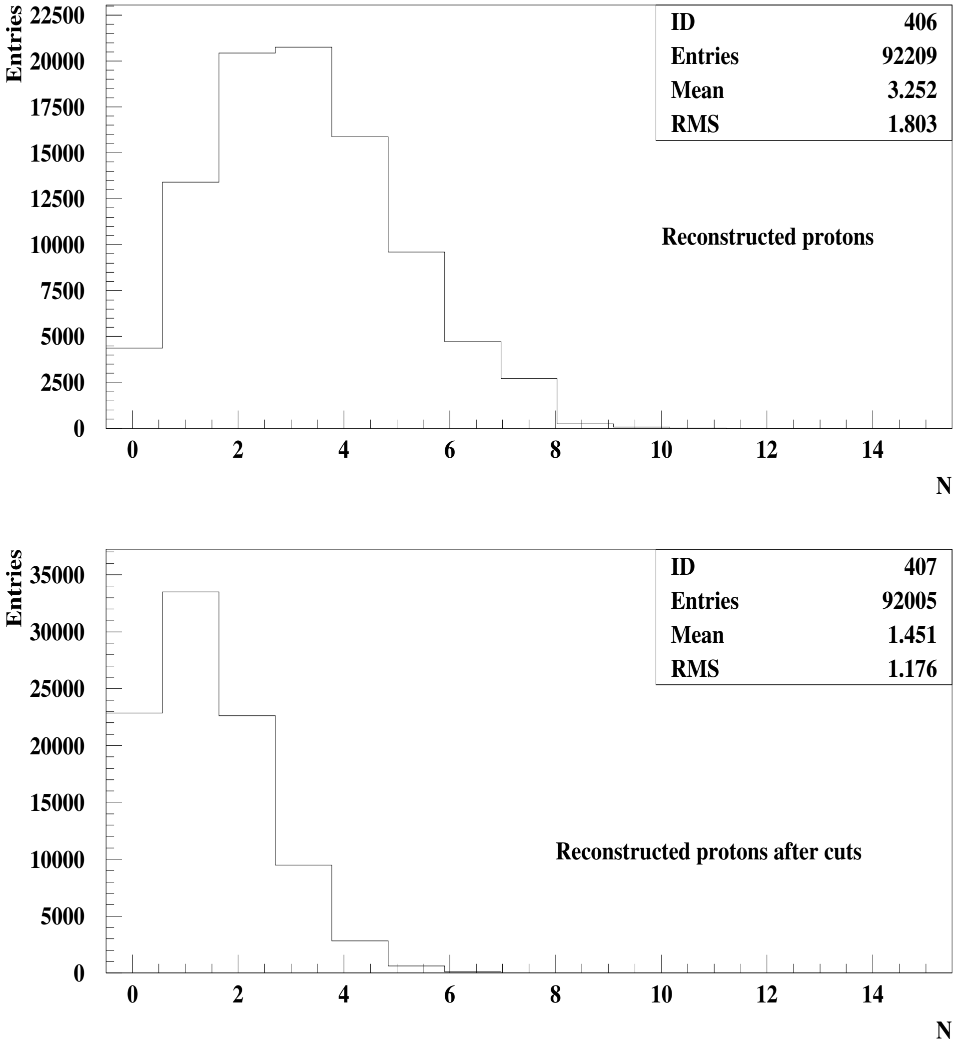

Figure 6.7: Multiplicity of the reconstructed protons in our spectrometer before (upper panel) and after (lower panel) track selection cuts

ration cut in particular.

Figure 6.8 presents the simulated two-proton correlation function. Only the requirement of TOFU non-sharing was imposed on two tracks. As one can see, at low q_{inv} the correlation is less than 1, reflecting the fact that the shape of the "background" distribution is different from the shape of the "true" distribution. Pairs from the same event suffer from additional losses due to the effects of two-track reconstruction efficiencies.

Figure 6.9 summarizes the discussion in this section. On the lower right panel the result of the division of the measured raw correlation function (shown on the upper left panel) by the GEANT correction function (shown on the upper right panel) is shown. Even though the resulting corrected correlation function suffers from limited statistics, it is clear that the height of the correlation peak qualitatively agrees with the peak height of the correlation function obtained with two-track separation cuts.

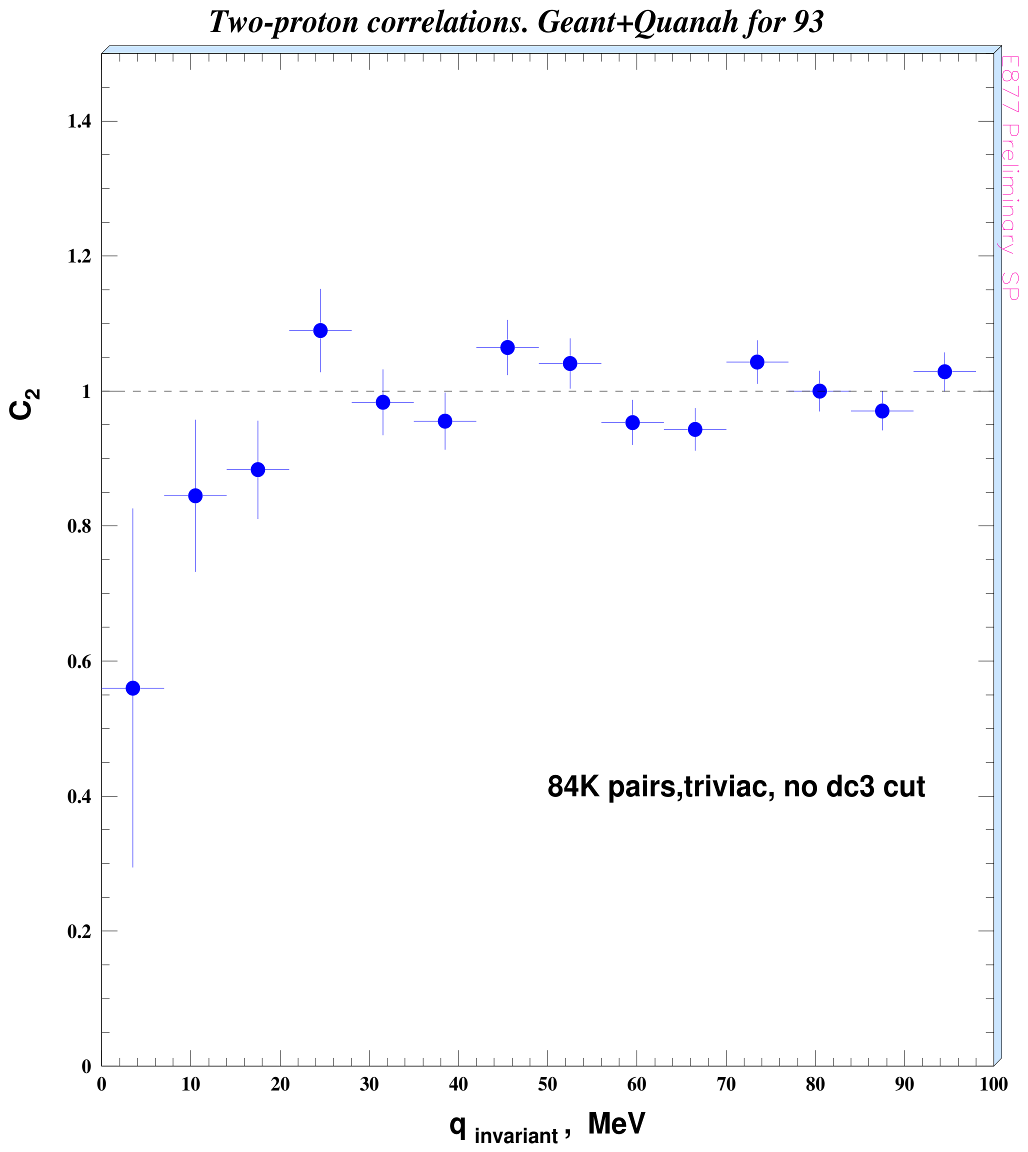

Figure 6.8: GEANT simulated two-proton correlated function. No cut on track separation in DC3 was applied

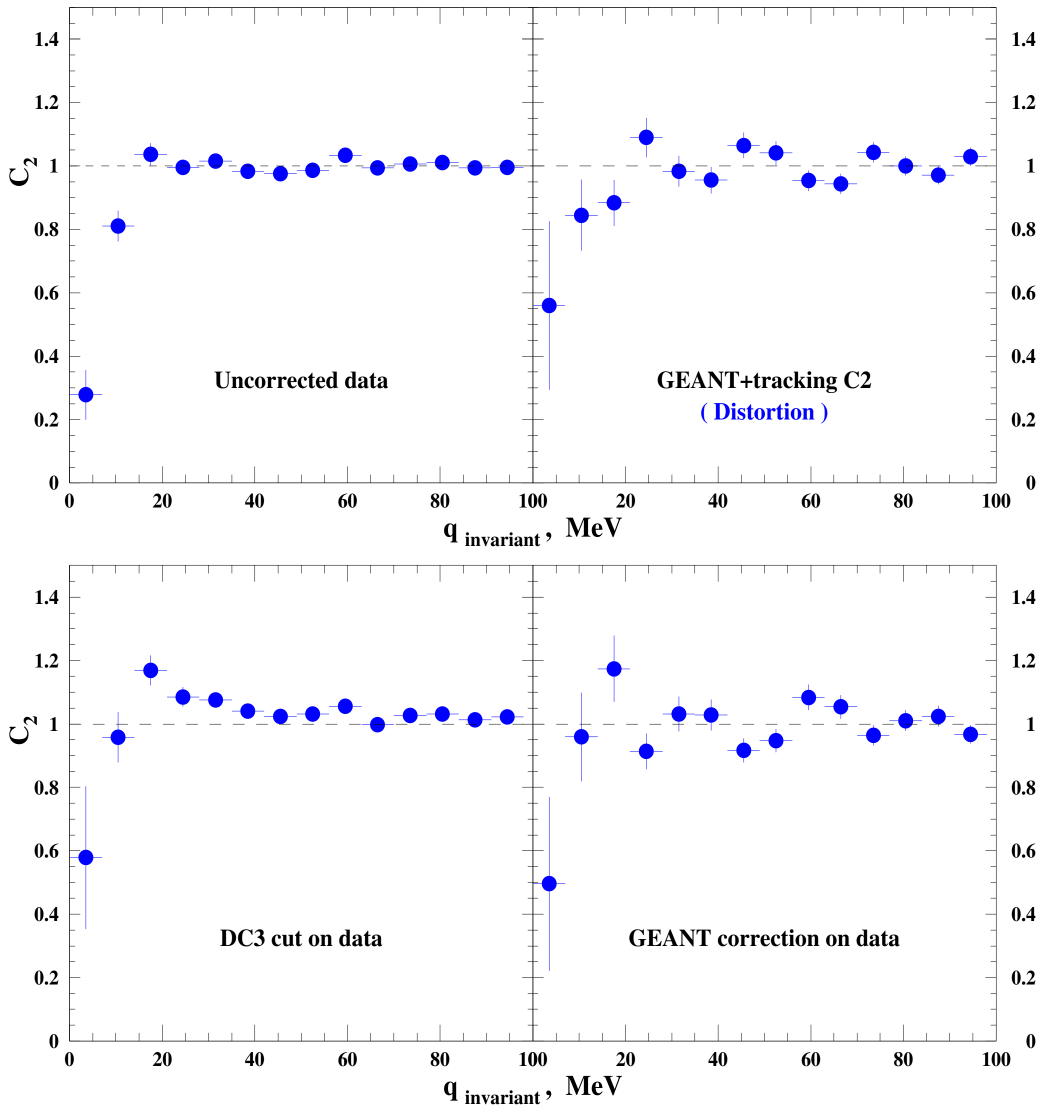

Figure 6.9: Left panels: top- Uncorrected correlation function from data , bottom- 20mm cut on track separation in DC3 was applied on the raw correlation function; Right panels: top- GEANT simulated correlated function, bottom- raw correlation function from data divided by the uncorrected GEANT correlation function.

Chapter 7

Results of 14.6 A·GeV/c Si+Pb collisions

In this Chapter we present the results of an analysis of the two-proton correlation functions, measured by the E814 Collaboration in 14.6 A·GeV/c Si+Pb collisions at AGS BNL during the Spring run of 1991. Details of particle identification were described earlier, more details on systematics of the single particle proton distributions can be found in Reference [62]. Additional details on the specifics of the two-particle correlation analysis, and two-pion correlations in particular can be found in Reference [63].

7.1 Description of the Data Set

The data set consists of two groups of runs. The first group consists of 4 runs with a Pb target with a thickness of 1% of a Si interaction length and the other group has 4 runs taken with 2% targets. It was reported in References [62, 64] that no significant difference, in terms of momentum resolution

Target	Thickness, mm(gr/cm^2)	Central Events	Selected Protons
Pb 1%	1.02 (1.110)	102.4k	142.6k
Pb 2%	2.02 (2.216)	127.9k	178.0k

Table 7.1: Target properties and statistics of the analyzed Si+Pb runs.

and lepton contamination[1], exists between the data sets. The measurements presented here are averaged over 1% and 2% targets.

About 230k events were selected, after a cut on transverse energy deposition in TCAL, corresponding to the upper 10% (most central) of the geometrical cross section. The average number of reconstructed protons per event was close to 1.4 . Table 7.1 gives some general information about the run groups.

The data set yielded a total of 115.6k proton pairs. Figure 7.1 shows the distribution of some kinematic variables of the proton pairs for the different ranges of q_{inv}. For each pair, all vectorial quantities ($\vec{p}$ and $\vec{p_t}$) were defined as an average of two vectors. The rapidity of the pair was defined as a half of the sum of rapidities of individual particles. The most sensitive region for correlations is hatched on the picture. In order to give a more quantitative characterization of the distributions, Table 7.2 shows a summary of the av-

[1] **Electron and positron contamination was estimated to be less than a few percent for pions and completely negligible for protons.**

Parameter	q_{inv} ≤0.05 GeV/c	q_{inv} ≤0.1 GeV/c	q_{inv} ≤1.0 GeV/c
$< P >$, GeV/c	4.71	5.37	5.78
$< P_z >$, GeV/c	4.71	5.36	5.77
$< P_t >$, GeV/c	0.16	0.18	0.21
$< y >$	2.18	2.32	2.34

Table 7.2: Mean values (from top to bottom) of the momentum, longitudinal momentum, transverse momentum and rapidity distributions of the proton pairs measured in 14.6 A·GeV/c Si+Pb collisions. See description in the text.

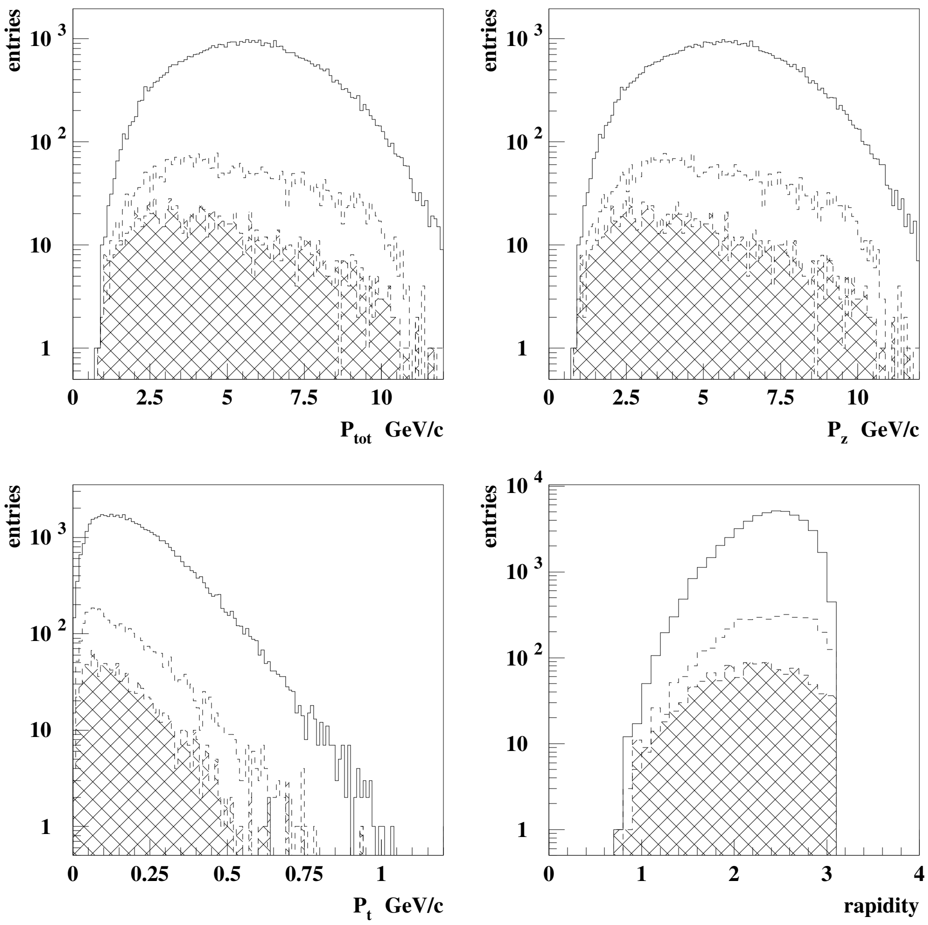

Figure 7.1: Some kinematic characteristics of the proton pairs. Top-left: total momentum, top-right: longitudinal momentum, bottom-left: transverse momentum, bottom-right: rapidity. The solid and dashed histograms represent the distributions for pairs with q_{inv} $\leq$1.0 GeV/c and q_{inv} $\leq$ 0.1 GeV/c respectively. Distributions for pairs with q_{inv} $\leq$0.05 GeV/c are hatched.

eraged values for the distributions presented on Figure 7.1. Note that pairs with small q_{inv} are considerably "softer", on average, than the rest of the data set.

7.2 Cuts on Proton Pairs

Before constructing the correlation function, several cuts were applied. Beam momentum protons were suppressed by a cut on the proton rapidity $y \leq 3.1$. This cut can be seen in the pair's rapidity distribution, shown on the lower right panel on Figure 7.1.

The "background" distribution, N_{bk}, was obtained using an event mixing method, as described in Chapter 6. A standard requirement that the two protons did not share the same slat of the TOF hodoscope has been imposed on pairs from both distributions.

In order to suppress effects of two-track reconstruction inefficiencies, a cut on two-track horizontal separation, in the drift chambers, was applied. Figure 7.2 shows the ratio of the ΔX distributions in DC2 for "true" and "background" pairs. It is clear that the shapes of two distributions become increasingly different at small separations. As we discussed in Chapter 6, this is because the event mixing procedure does not reproduce effects of two-track reconstruction.

A vertical line, on Figure 7.2, shows the position of the cut on two-track separation in the horizontal plane, that was subsequently applied. The value

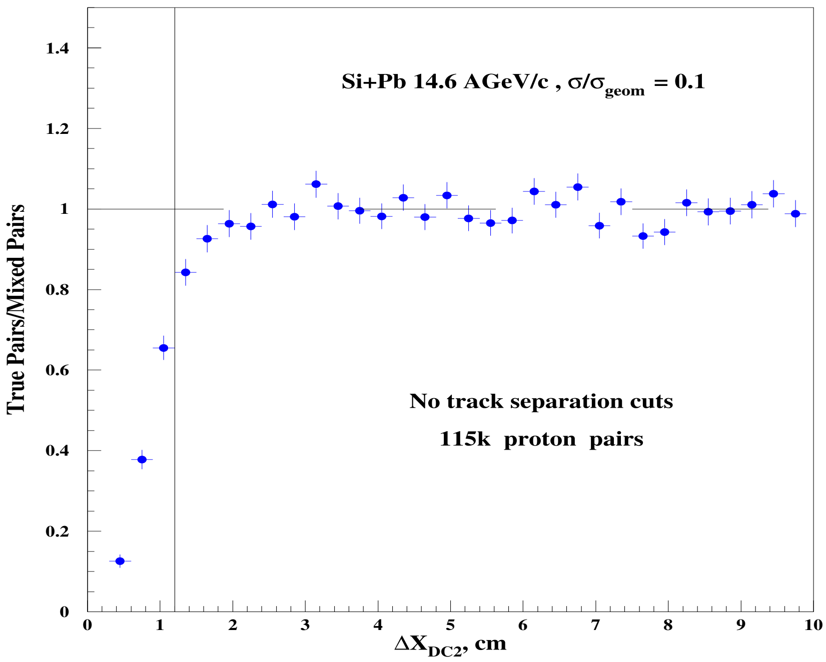

Figure 7.2: Ratio of the ΔX_{DC2} distributions of "true" and "background" pairs before cuts. See description in the text.

of the cut has been chosen to be approximately equal to twice the size of the drift cell of the each chamber. Figure 7.3 shows the same ratio after the combined cut on minimum separations in DC2 (12 mm) and DC3(24 mm) was applied. It is clear that the ratio of the ΔX distribution of survived pairs is consistent with unity. After all cuts, the N_{tr} distribution contains about 55k reconstructed proton pairs. Table 7.3 summarizes the influence of the above cuts on the proton pair statistics.

Figure 7.4 shows the influence of the cuts on the shape of the correlation

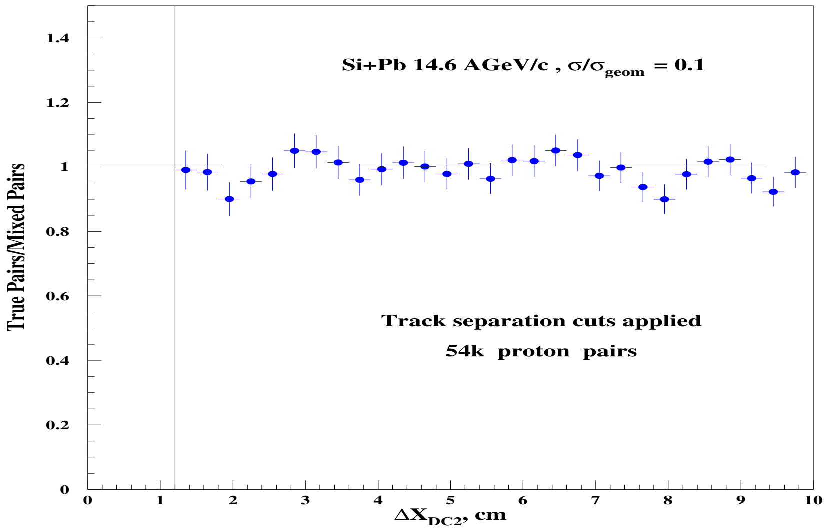

Figure 7.3: Ratio of the ΔX_{DC2} distributions of "true" and "background" pairs after applying the two-track separation cuts. See description in the text.

Cut	Number of pairs
No cuts	115647
$y \leq 3.1$ only	55665
$y \geq 3.1$ only	13980
$y \leq 3.1 + \Delta$X cuts	54781

Table 7.3: Number of proton pairs after cuts. See description in the text.

function. The final correlation function, after all cuts, is plotted on Figure 7.5. The error bars reflect only statistical uncertainties. The background distribution was normalized to the total number of entries in the true distribution within the range $100 < q_{inv} < 1000$ MeV/c. It can be seen from this figure that the distribution is fairly flat for $q_{inv} > 70$ MeV/c . At relative momentum close to 20 MeV/c, a prominent proton-proton resonance peak is evident.

The position and height of the peak is consistent with the E802 preliminary two-proton correlation function [37] measured in 14.6 A·GeV/c Si+Au collisions at $\sigma_{trig}/\sigma_{geom} \approx 12\%$, though the E802 measurement was performed at mid-rapidity and our measurement is at forward rapidities.

We will postpone further discussion of our result until Chapter 9 where it will be compared with a Au+Au data and model calculations.

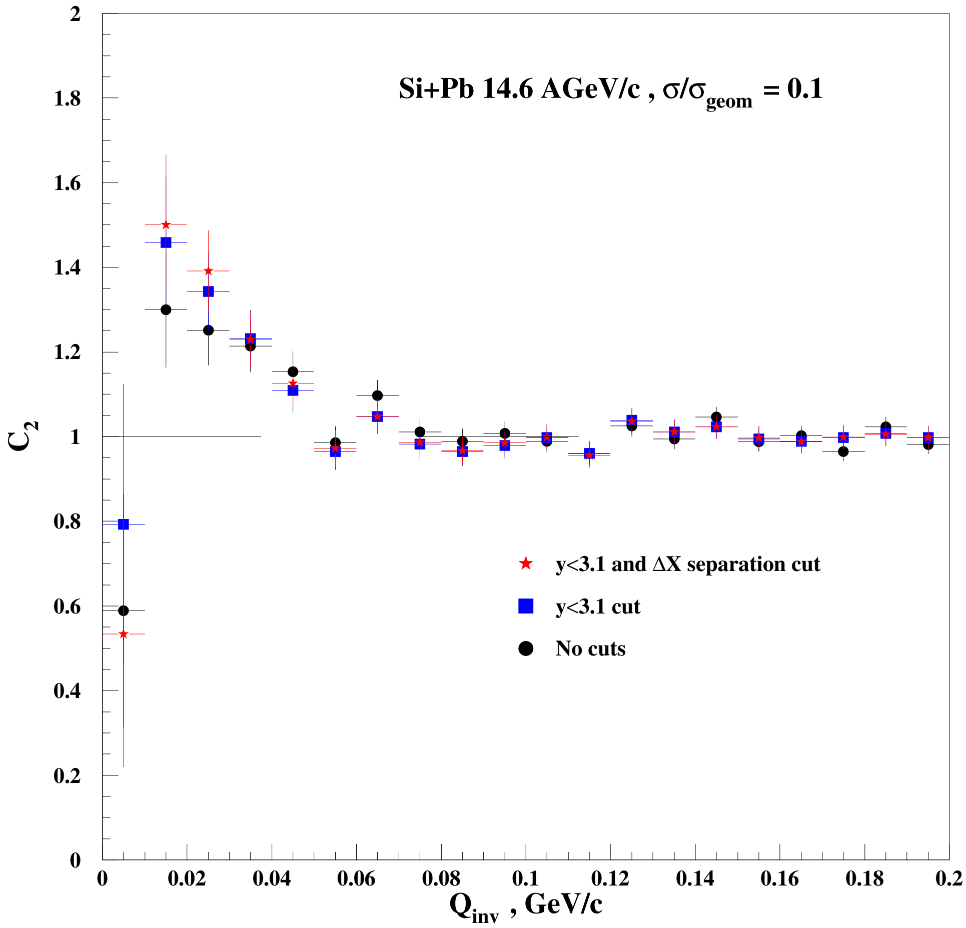

Figure 7.4: Influence of the cuts on the shape of the two proton correlation function for the Si+Pb system.

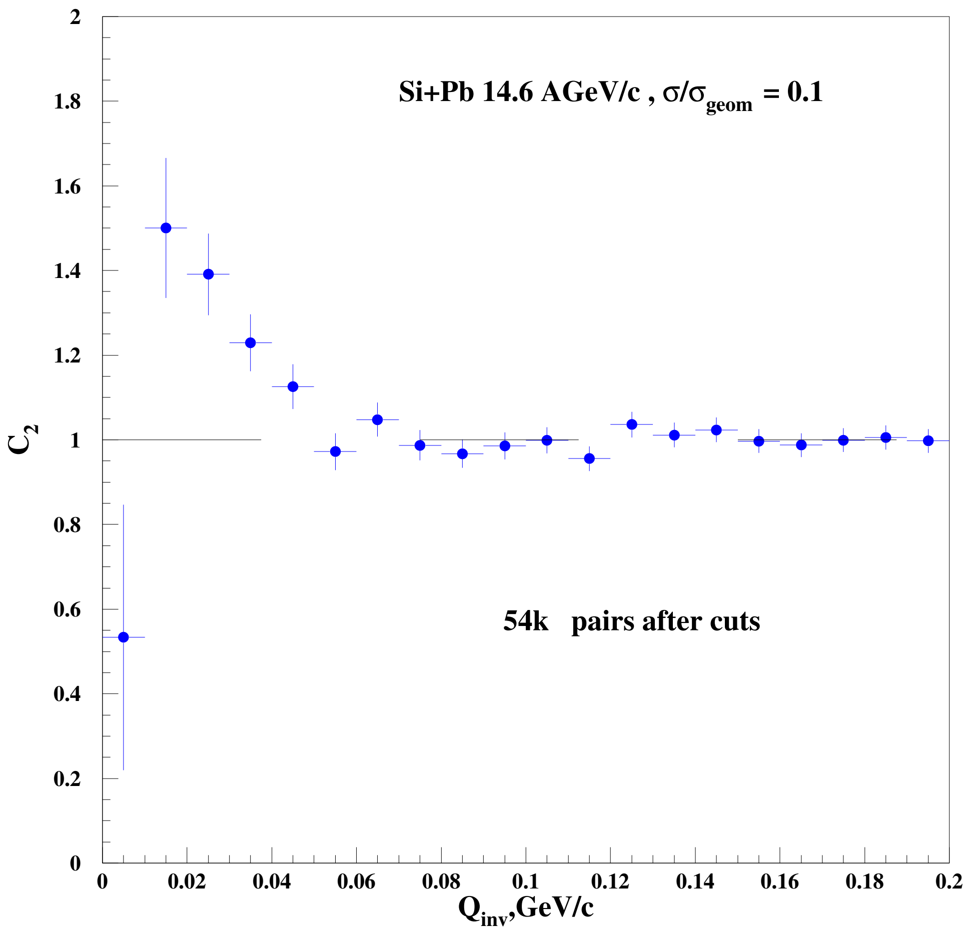

Figure 7.5: Measured two-proton correlation function in 14.6 AGeV/c Si+Pb collisions.

Chapter 8

Results of 10.8 A·GeV/c Au+Au Collisions

In this Chapter we present the results of the analysis of the two-proton correlation functions, measured by the E877 Collaboration in 10.8 A·GeV/c Au+Au collisions at AGS BNL during the Fall run of 1993. The details of the event selections were discussed in Chapter 4. Track selection procedures and details of particle identification were presented in Chapter 5. The methodical aspects of two-particle correlation analysis were discussed in Chapter 6. The data presented in this chapter was an initial objective for this thesis research.

8.1 Description of the Data Set

During this run a 2% interaction length Au target was used; the dipole magnet was operated in B-polarity and the value of the magnetic field integral was 0.262 $T \cdot m$. The number of analysed runs was 29.

In order to account for the distortions of the correlation function introduced by the two-track reconstruction inefficiency in high multiplicity events, cuts on the separation of two tracks in the drift chambers were introduced. About 522k “true” pairs were selected from 881k events which satisfied the global event selection requirements. Figure 8.1 shows the distribution of some kinematic variables of the proton pairs for different ranges of q_{inv}. For each pair, all vectorial quantities ($\vec{p}$ and $\vec{p_t}$) were defined as an average of two vectors. The rapidity of the pair was defined as a half of the sum of rapidities of individual particles. The most sensitive region for correlations, is hatched on the picture. In order to give a more quantitative characterization of the distributions, Table 8.1 shows a summary of the averaged values for the distributions presented in Figure 8.1. The measured proton-proton correlation function is shown on Figure 8.2.

One can see that the height of the peak at 20 MeV/c in the Au+Au collisions is lower than that of the Si+Pb collisions, indicating a larger source size for the heavier colliding system, although one must remember that the beam energy for the Si projectile was higher than the Au projectile. The peak height of the two-proton correlation function measured by E802 in 14.6 A·GeV/c Si+Al was found [37] to be even higher than that measured in Si+Au collisions. Such a systematic trend implies that the proton-proton correlation function is sensitive to the number of participants in heavy-ion collisions.

Parameter	q_{inv} ≤0.05 GeV/c	q_{inv} ≤0.1 GeV/c	q_{inv} ≤1.0 GeV/c
$< P >$, GeV/c	6.7	7.0	6.9
$< P_z >$, GeV/c	6.7	7.0	6.9
$< P_t >$, GeV/c	0.28	0.29	0.31
$< y >$	2.5	2.6	2.5

Table 8.1: Mean values (from top to bottom) of the momentum, longitudinal momentum, transverse momentum and rapidity distributions of the proton pairs measured in 10.8 A·GeV/c Au+Au collisions. See description in the text.

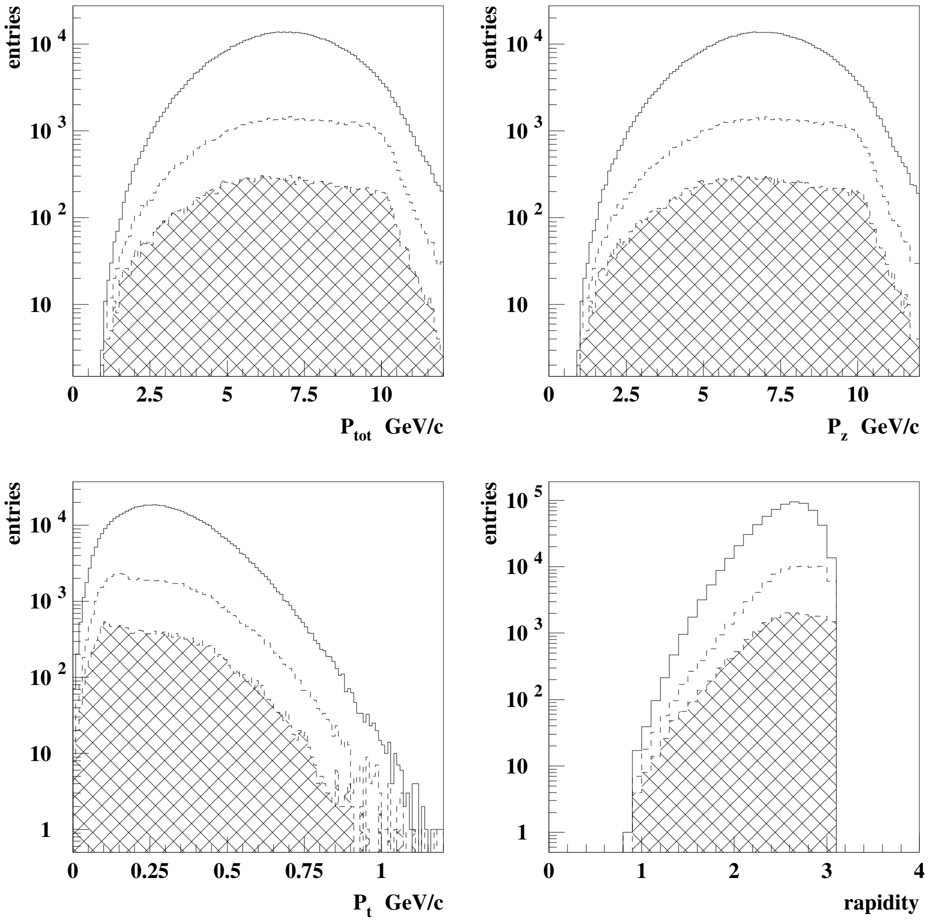

Figure 8.1: Some kinematic characteristics of the proton pairs. Top-left: total momentum; top-right: longitudinal momentum; bottom-left: transverse momentum; bottom-right: rapidity. The solid and dashed histograms represent the distributions for pairs with q_{inv} $\leq$1.0 GeV/c and q_{inv} $\leq$ 0.1 GeV/c respectively. Distributions for pairs with q_{inv} $\leq$0.05 GeV/c are hatched.

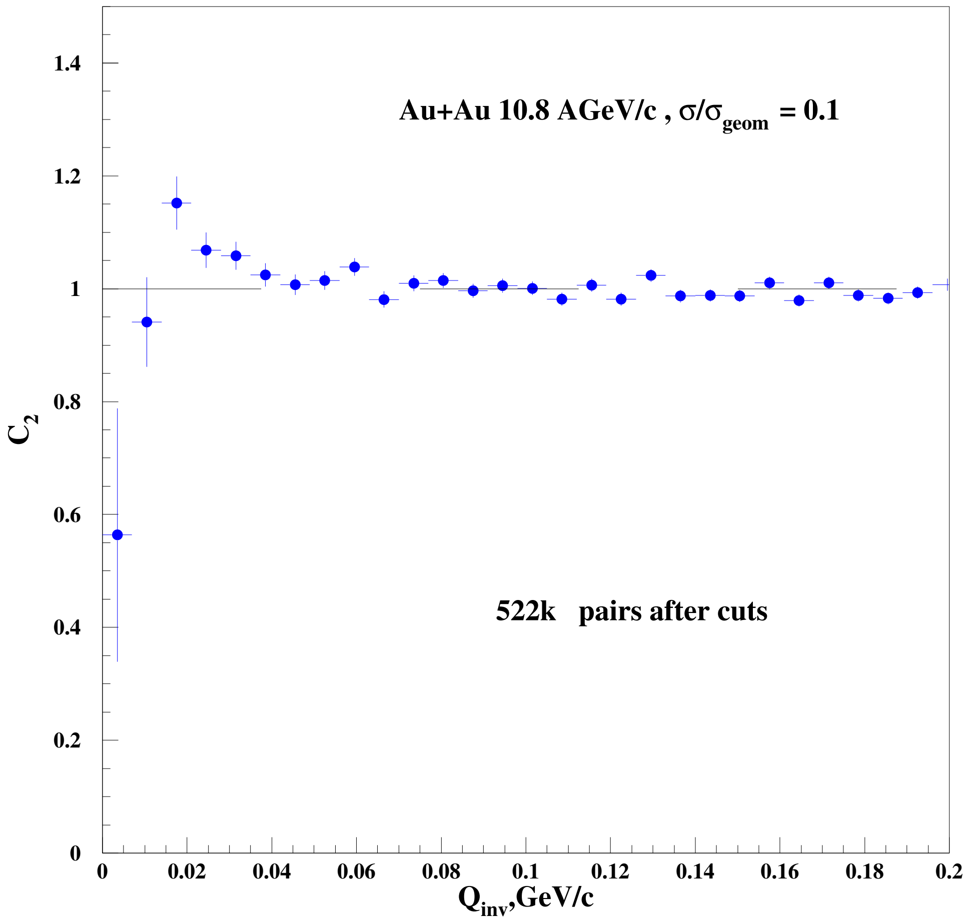

Figure 8.2: Measured two-proton correlation function in 10.8 AGeV/c Au+Au collisions.

Chapter 9

Discussion and Comparison to RQMD

In this Chapter we will discuss results of the measurements of the two-proton correlation functions in Si+Pb at 14.6 AGeV/c and Au+Au at 10.8 AGeV/c reactions. The measured proton-proton correlation function (solid symbols) is shown on the lower panel of Figure 9.1 along with the RQMD predictions (open symbols). One can see that the height of the peak at 20 MeV/c in the Au+Au collisions is lower that that of the Si+Pb collisions, indicating a larger source size for the heavier colliding system. The peak height of the two-proton correlation function measured by E802 in 14.6 A·GeV/c Si+Al was found [37] to be even higher than that from the Si+Au collisions. Such a systematic trend implies that the proton-proton correlation function is sensitive to the total number of nucleons involved in collision.

In order to extract physical information from the measured correlation function, we carried out a study using the phase space produced by the event generator RQMD(v1.08) [38, 39]. This model describes classical propagation of the particles, together with quantum effects of stochastic scattering and

Pauli blocking. It includes color strings, baryon and meson resonances, as well as finite formation time for created particles. It has been successful in the description of many features of relativistic heavy-ion collisions. In this model a particle's freeze-out position is defined as a point of the last strong interaction.

The basic structure of our approach is as follows: by taking the freeze-out phase-space distribution generated by RQMD and propagating the particles through the experimental acceptance, accounting for the resolution of the detectors, a subset of the phase-space points was obtained. Then the Koonin-Pratt method [40, 60] was used to construct the proton-proton correlation function. This method provides a description of the final state interactions between two protons and antisymmetrization of the their relative wave function. The results of the calculations are shown as open symbols on both panels of Figure 9.1. One can see that agreement between the experiment and the model is fairly good. Assuming that RQMD simulates the freeze-out phase-space and configuration space distributions correctly, one can ask what are the parameters of the proton source in this model? Figure 9.2 shows corresponding distributions for both colliding systems. We selected protons with freeze-out time $c\tau \leq 70$ fm; this cut has no significant effect on the proton size parameters. For all calculations, the nucleon-nucleon center of mass system was used. For the purpose of comparison, we also evaluated the parameters of the proton distributions at mid-rapidity (-1.0 $\leq y_{NN} \leq$ 1.0). Mean values and random mean squared of the distributions are listed in the Table 9.1.

Figure 9.2 clearly shows effects that complicate interpretation of the correla-

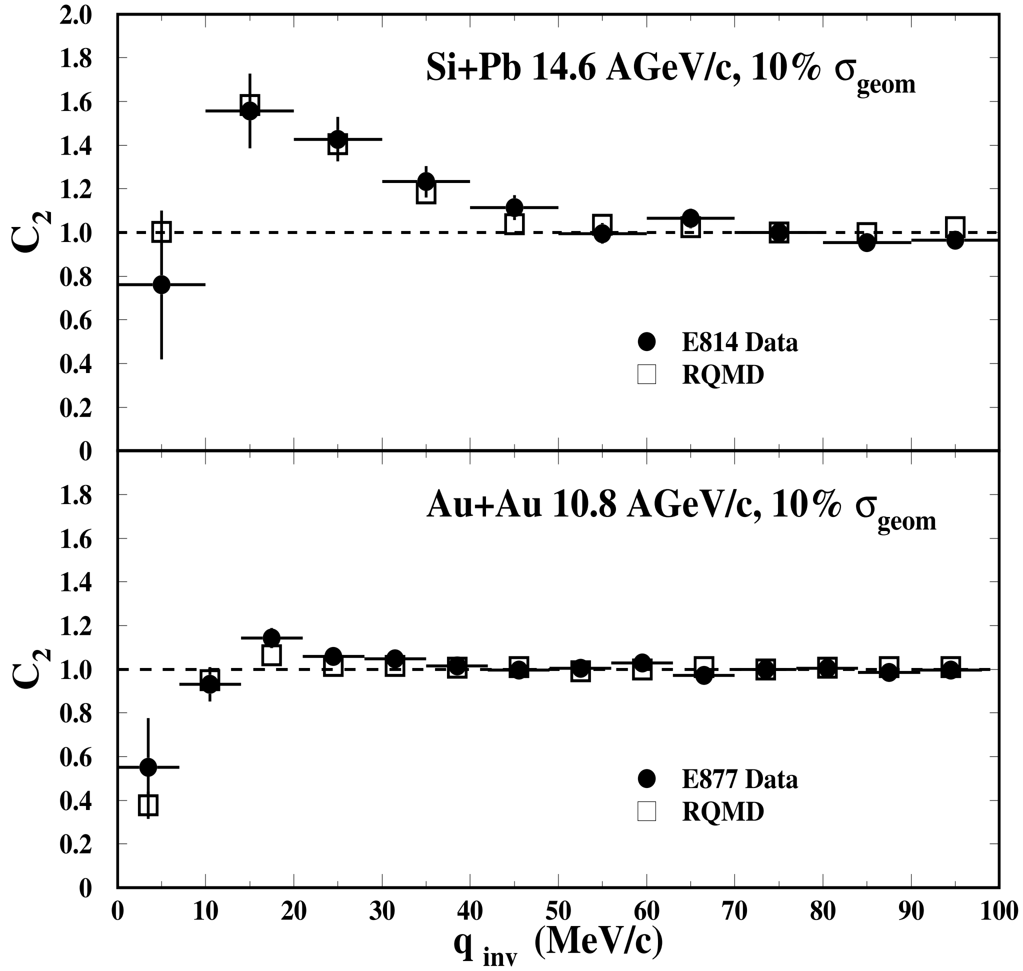

Figure 9.1: Two-proton correlation functions for Si+Pb (upper panel) and for Au+Au (lower panel) central collisions. Experimental results are shown as filled circles while the RQMD model predictions are shown as open squares.

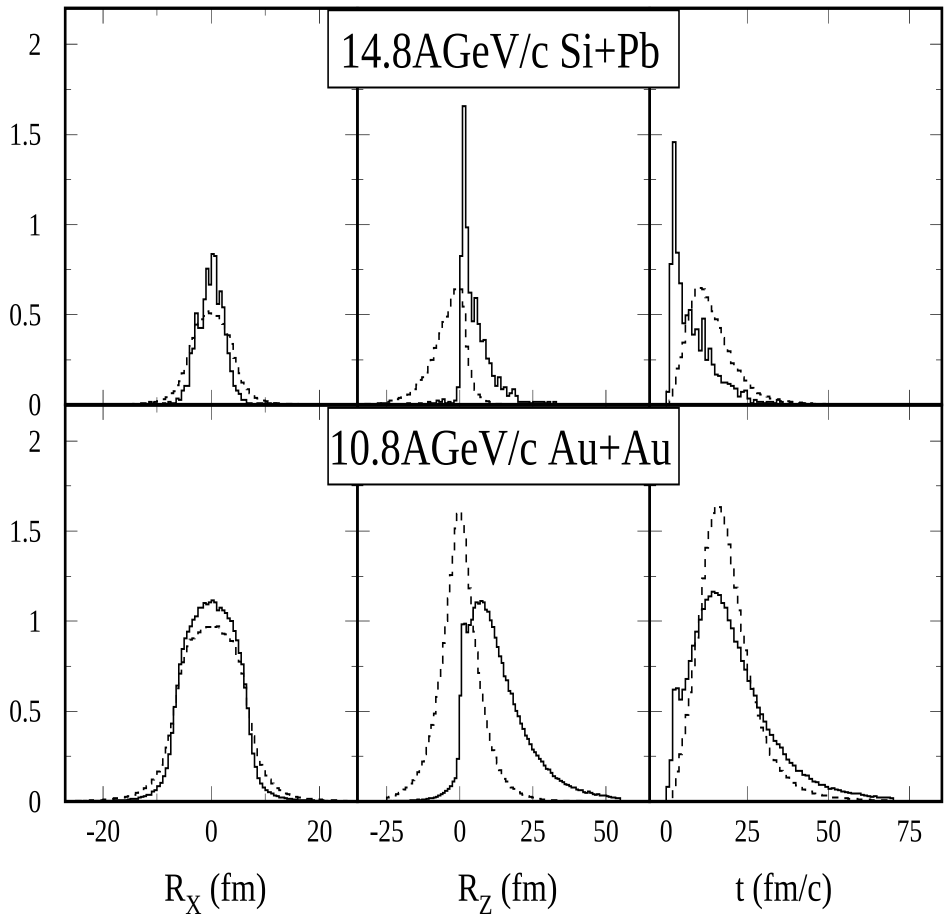

Figure 9.2: Proton distributions from RQMD(v1.08). Solid lines represent the distributions of the protons emitted into the E814/E877 spectrometer acceptance; dashed lines represent those at mid-rapidity $-1 \leq y_{NN} \leq 1$.

tion function. Different rapidity intervals yield different source distributions. This is a natural consequence of the proton momentum-position correlations. It is also clear that, in the RQMD model, protons are emitted over a non-zero interval of time. The system is continuously evaporating particles during the evolution of the collision. Two-particle correlations measure the distance between particles at the instant the second particle is produced [61] and this distance depends not only on the size of the source, but also on the duration of emission. This leads to several effects observed in two-particle interferometry such as dependence of the correlation function on the temperature of the source and it's velocity relative to the observer [12, 61]. It is not yet clear how to disentangled these contributions.

It is interesting to compare the geometrical parameters of the proton source in the model with those of the target and projectile nuclei. The equivalent Gaussian one-dimensional RMS radii of the Si and Au projectiles are 1.6 and 3.1 fm, respectively. (We assumed $R_{rms}^{proj} = \sqrt{1/5} r_0 A^{1/3}$ with $r_0 = 1.2$ fm.) From Table 9.1, one can see that all transverse radii (R_x in the Table) are significantly larger than the projectile values for both Si+Pb and Au+Au colliding systems. This increase in size parameters may be related to the transverse expansion observed [31, 32] in transverse momentum distributions. Larger transverse size parameters are found at mid-rapidity which may be attributed to the higher transverse velocity of expansion. It can be seen from Table 9.1 that in RQMD the overall proton spatial distribution is elongated along the beam direction. This is consistent with the effects of collective longitudinal expansion and incomplete stopping, although it is difficult to tell at this point

System	Source Parameters	$-1 < y_{NN} < 1$		In Acceptance	
		Mean	RMS	Mean	RMS
	R_X	0.0	3.9	0.0	2.5
Si+Pb	R_Z	-4.2	6.5	5.1	5.8
	$c\tau$	14.	7.3	8.4	6.9
	R_X	0.0	5.7	0.0	4.7
Au+Au	R_Z	0.0	7.6	12.7	10.5
	$c\tau$	18.9	8.8	18.3	13.0

Table 9.1: Parameters of the proton source calculated using the RQMD model for Si+Pb and Au+Au systems for different rapidity intervals. All source parameters are in fermi.

which effect plays a dominant role.

Chapter 10

Results of 11.5 A·GeV/c Au+Au Collisions

In this Chapter we present the results of the analysis of the two-proton correlation functions, measured by the E877 Collaboration in 11.5 A·GeV/c Au+Au collisions at AGS BNL during the Fall run of 1994.

In retrospect, the main focus of the 1993 data set, which we described in Chapter 8, was to obtain the first measurement of the two-proton correlation function of a truly heavy colliding system at AGS energies and to compare it with the available Si beam data. From the analysis point of view it was important to study the systematics of the upgraded spectrometer and the challenges imposed by the increased multiplicity in Au+Au collisions. Also a new approach to the determination of the parameters of baryon freeze-out with the help of a different type of correlation measurement, proton-deuteron correlations (which we will describe in Chapter 11), was attempted.

The 1994 data set opened new possibilities for the analysis of two proton correlations. The statistics were increased by an order of magnitude and the spectrometer systematics and analysis cuts were better understood. This allowed, in particular, a study of centrality and reaction plane dependencies.

10.1 Description of the 1994 Data Set

The general settings for this run were fairly similar to the 1993 run described in Chapter 8. Target thickness was 1.9% of an interaction length (about 0.5 mm). The value of the magnetic field integral of the dipole magnet was 0.335 $T \cdot m$; B-polarity was used. A total of 282 runs were analyzed.

Tracking was performed for the events with transverse energy deposited in the Participant Calorimeter (PCAL) greater then 150 GeV, which corresponds to approximately the upper 22% percent of the total cross section. Subsequent cuts on centrality were applied in the correlation analysis stage. Because of higher statistics in this data set it was possible to apply a much tighter cut on centrality. The approach of the selection of good event was identical to what was used for the analysis of the 1993 data, discussed in Chapter 4. The track selection procedure and particle identification process were also similar to the 1993 approach which was presented in Chapter 5.

For the purpose of studying the centrality dependence of the correlation function we subdivided the available data set into two subsets with different centralities. First we will discuss analysis details of the most central subset of the data, which also has higher statistics than the other subsets. We will discuss the details of centrality definition as well as the less central data set later in this Chapter.

Parameter	q_{inv} ≤0.05 GeV/c	q_{inv} ≤0.1 GeV/c	q_{inv} ≤1.0 GeV/c
$< P >$, GeV/c	6.7	7.1	7.0
$< P_z >$, GeV/c	6.7	7.1	6.9
$< P_t >$, GeV/c	0.28	0.30	0.33
$< y >$	2.5	2.6	2.5

Table 10.1: Mean values (from top to bottom) of the momentum, longitudinal momentum, transverse momentum and rapidity distributions of the proton pairs measured in 11.5 A·GeV/c Au+Au collisions at 4% centrality.

10.2 4% Centrality Data Set

Figure 10.1 shows the distribution of some kinematic variables of the proton pairs for the different ranges of q_{inv}. Table 10.1 shows a summary of the average values for the distributions presented in Figure 10.1. The definitions of the variables and cuts are identical to those used in 1993 data set analysis and were described in Chapter 8. It can be seen from the table that the region with lowest relative momentum also has a mean transverse momentum about 50 MeV lower than the whole of the data set. The average value of the rapidity distribution is fairly similar for all intervals of q_{inv}.

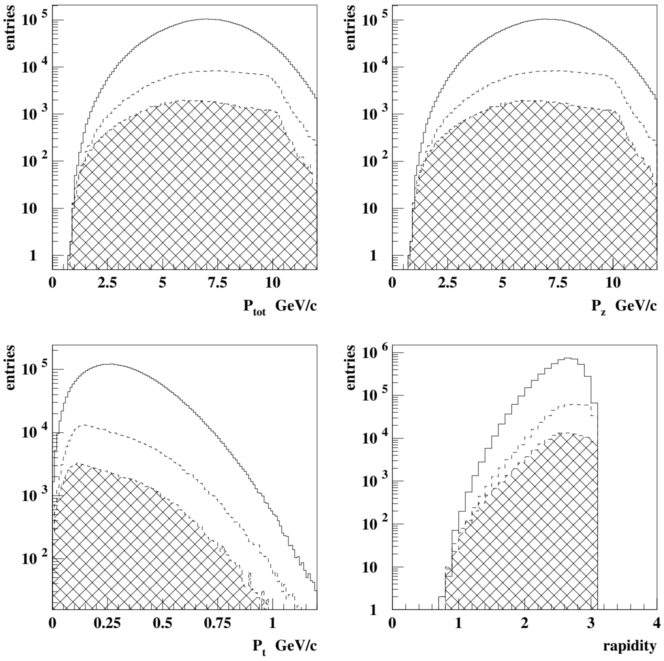

Figure 10.1: Some kinematic characteristics of the proton pairs in 1994 data set, with 4% centrality cut . Top-left: total momentum; top-right: longitudinal momentum; bottom-left: transverse momentum; bottom-right: rapidity. The solid and dashed histograms represent the distributions for pairs with q_{inv} $\leq$1.0 GeV/c and q_{inv} $\leq$ 0.1 GeV/c respectively. Distributions for pairs with q_{inv} $\leq$0.05 GeV/c are hatched.

10.2.1 Cuts on Proton Pairs

Before constructing the correlation function, several cuts were applied to the proton pairs. The cuts were the same as in the 1993 data set, discussed in Chapter 6. We briefly recall them here:

- Beam momentum protons were suppressed by a cut on the proton rapidity $y \leq 3.1$.

- In order to suppress effects of two-track reconstruction inefficiencies, the standard cut on two-track separation in the drift chambers was applied.

- A requirement that the two protons did not share the same slat of the TOF hodoscope has been imposed on pairs from both distributions. This condition stems from the particle identification routine and ensures the correct determination of the particle's time of flight. Taking into account the finite size of the slats this requirement also serves as a cut on track separation.

- During the mixing event procedure it was required that protons in the pair should have a PCAL E_T difference less than 10 GeV. This requirement takes into account possible dependencies of the correlation function on the reaction plane.

After all cuts, the N_{tr} distribution contains about 5.6 million reconstructed proton pairs. Table 10.2 summarizes the influence of the above cuts on the proton pair statistics. Figure 10.2 shows the influence of the cuts on the

Cut	Number of pairs
No cuts	8166812
$y \leq 3.1$	5715609
$y \leq 3.1 + \Delta$X cuts	5565122

Table 10.2: Number of proton pairs after cuts. Au+Au collisions at 11.5 AGeV/c with 4% centrality cut. See description in the text.

shape of the correlation function. The uncorrected correlation function exhibits a "dip-bump" shape even though the peak of the correlation function is distorted. As discussed in Chapter 6 the distortion is due to the two-track reconstruction inefficiency. The cut on pair rapidity did not significantly affect the shape of the raw correlation function.

The correlation function is shown in Figure 10.3. The increased statistics allowed us to present the correlation function with 5 MeV/c binning, instead of our standard 7 MeV/c. This reveals the shape of the correlation function in greater detail. The canonical "dip + bump" shape of the correlation function with a maximum around 22 MeV/c is evident. Figure 10.4 shows the influence of the two-track separation cuts on the shape of the measured correlation function. Note that the scale of Figure 10.4 was changed in order to provide a better view of the correlation functions. It is clear that the shape

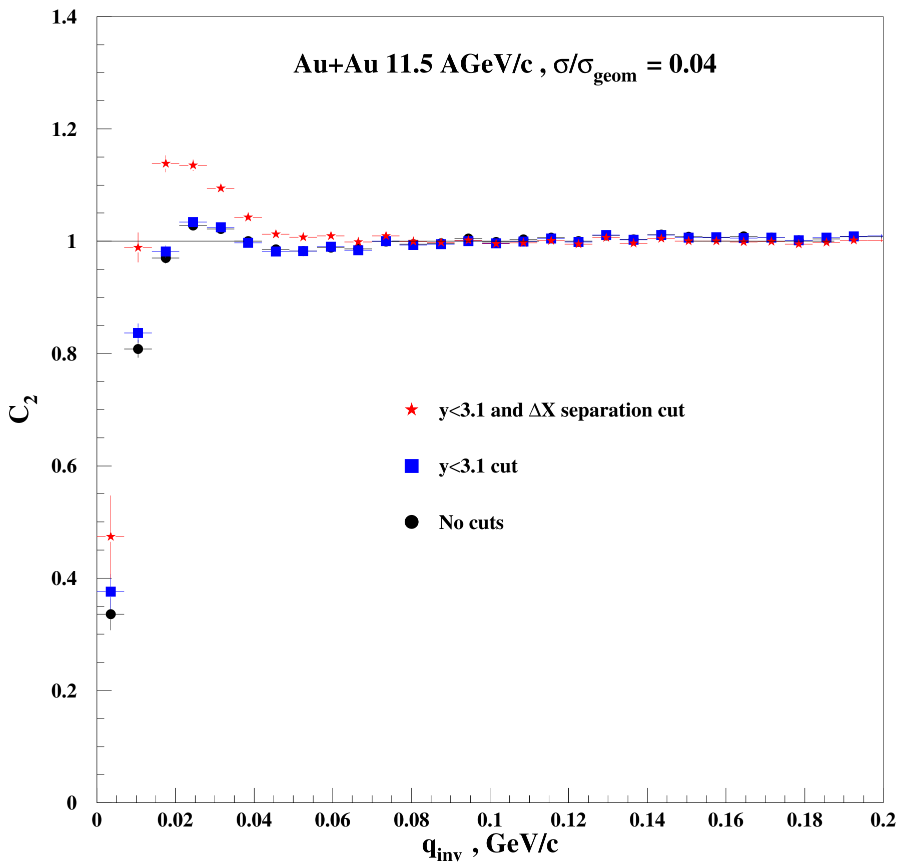

Figure 10.2: Influence of the cuts on the shape of the two proton correlation function for Au+Au at 11.5 AGeV/c with a 4% centrality cut.

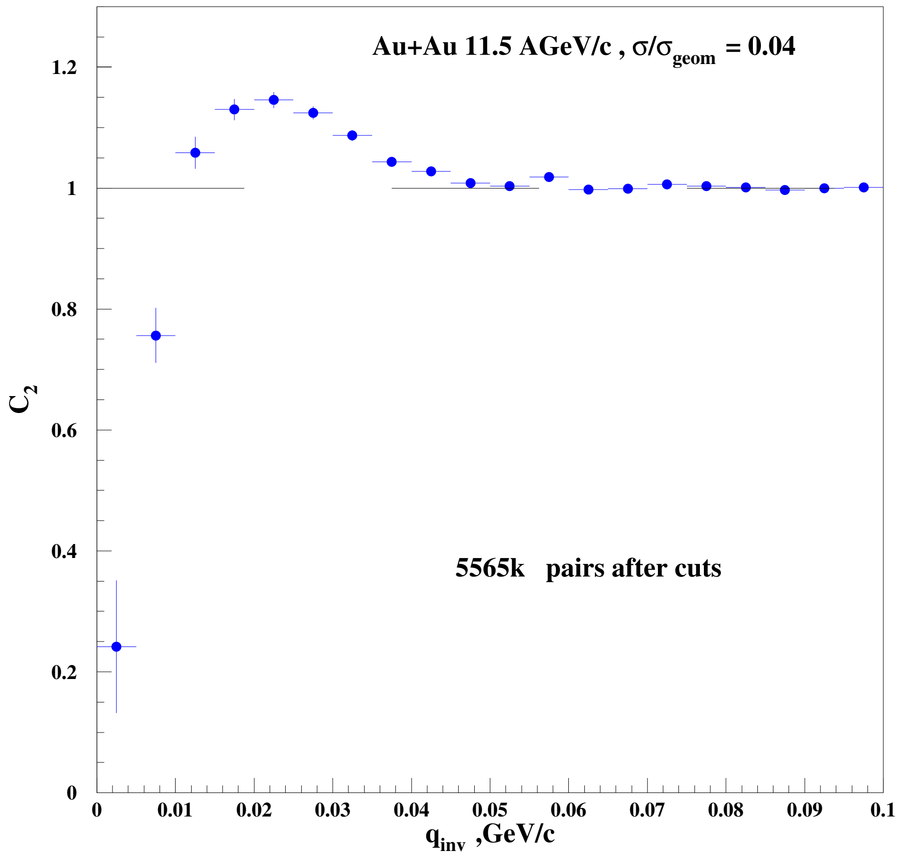

Figure 10.3: Measured two-proton correlation function in 11.5 AGeV/c Au+Au collisions.

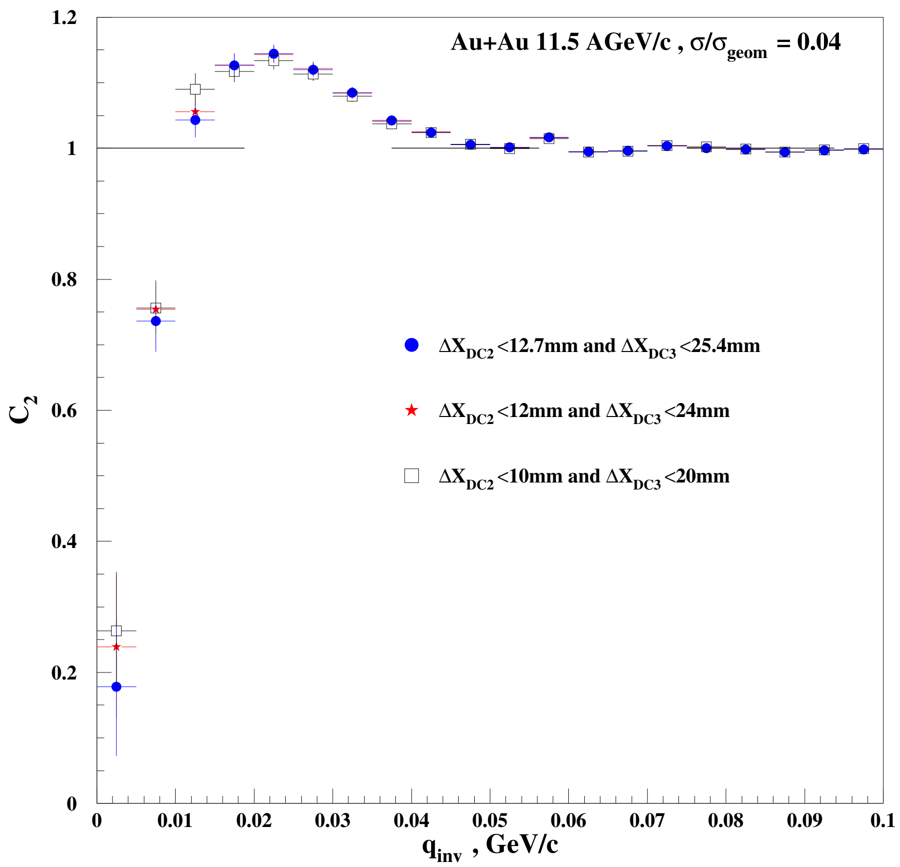

Figure 10.4: Influence of the two-track separation cuts on the shape of the two-proton correlation function.

of the correlation function in the peak area is fairly stable under the cut.

From the comparison of Figure 10.3 with Figure 8.2 it is also clear that the height of the correlation function peak agrees in both data sets, as one would expect.

10.3 Centrality Dependence

Usually, transverse energy (E_T) yielded in event is defined as

$$E_T = \sum_{particles} E_i \sin\theta_i \tag{10.1}$$

where E_i is a total energy of the i-th particle and θ_i is a polar angle of emission. It is intuitively clear that transverse energy, which characterizes the "violence" of the collision, is somehow related to the initial geometry of the collision. At impact parameter zero, where the overlap of two nuclei and hence the number of nucleons participating in the collision are maximal, it is natural to expect that the dissipation of the beam energy in the transverse direction will be highest as well. At maximum impact parameter the overlap of two nucleus and E_T deposition are minimal. In order to obtain a more quantitative relationship between E_T and the impact parameter one needs guidance from a model. Figure 10.5 shows a clear correlation between E_T and impact parameter in the transport model RQMD.

10.3.1 Centrality Definition

As we described in Chapter 3, E_T deposition in the calorimeters was used as a tag of collision centrality. E_T is defined as an energy deposition in a given calorimeter cell weighted with the sine of the angle θ_i at which center of the i-th cell is seen from the target

$$E_T = \sum_{allcells} E_i \sin\theta_i \quad . \tag{10.2}$$

For every run used in this analysis a look-up table was created. It gave a relation between the E_T interval (measured from a given E_T to a maximum E_T in the run) and a corresponding fraction of the geometrical cross section. The relationship was based on the following formula:

$$\frac{d\sigma}{dE_t} = \frac{s}{n_t \cdot B}\frac{dN}{dE_t} \tag{10.3}$$

where s is the trigger down-scaling factor for a given E_T, n_t is the number of target atoms per unit cross sectional area, and B is the number of incident beam particles.

This approach to the centrality definition automatically takes into account run by run fluctuations in the PCAL calibrations as well as drifts in the trigger thresholds. It gives a more consistent centrality definition than a cut on measured E_T for a large, multi-run data set. More details about the centrality determination in E877 and can be found in Reference [50]. Figure 10.6 shows the PCAL E_T distribution[1] and cuts on centrality (hatched) which were used

[1] The steps in the E_T distribution are determined by a trigger down-scaling, which we discussed in Chapter 3. Because the main goal of the 1994 run was to study the

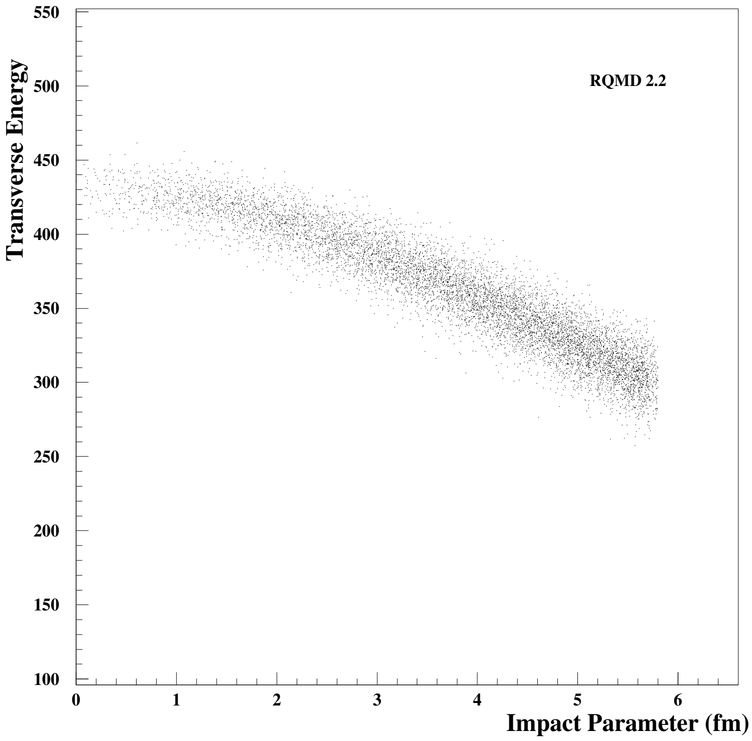

Figure 10.5: The total transverse energy E_T as a function of impact parameter in RQMD. E_T was defined according to formula 10.1.

in the centrality dependence study.

10.4 9% to 6% Centrality Data Set

The analysis structure was unchanged for this data set. All cuts on single tracks and proton pairs used for the analysis of this centrality interval were identical to the cuts used in studies of the 4% centrality data. Table 10.4 shows the influence of the applied cuts on the number of proton pairs. Table 10.3 shows a summary of the averaged values for the distributions presented in Figure 10.7. From comparison with Table 10.1 one can conclude that the average momentum of proton pairs in the less central data set is about 600 MeV higher than the average momentum of pairs in the most central 4% sample. The average transverse momentum is the same in both subsets.

10.5 Results for Different Centralities

Figure 10.8 shows the correlation function for different centrality intervals. One trend can be observed here: in the peak region the correlation function for the most central data set (4%) is somewhat lower than the correlation function from the less central (9% to 6% centrality) data set.

The change in the height of the correlation function may be determined

most central collisions, events with low energy deposition (lower than about 5% centrality) were down-scaled.

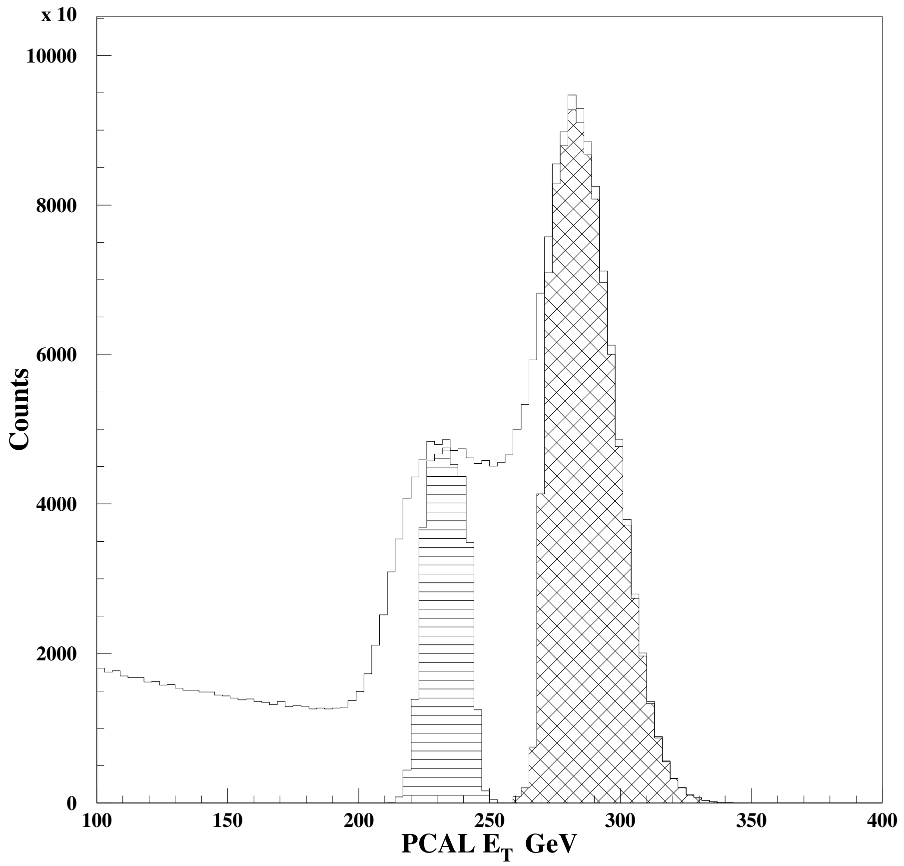

Figure 10.6: Uncorrected PCAL E_T spectrum in Au+Au collisions at 11.5 AGeV/c, cross-hatched region shows events with 4% centrality cut; horizontally hatched region shows events with centrality from 9 to 6 percent of the geometrical cross section. See description in the text.

Parameter	q_{inv} $\leq$0.05 GeV/c	q_{inv} $\leq$0.1 GeV/c	q_{inv} $\leq$1.0 GeV/c
$< P >$, GeV/c	7.3	7.7	7.4
$< P_z >$, GeV/c	7.3	7.7	7.3
$< P_t >$, GeV/c	0.28	0.30	0.34
$< y >$	2.6	2.7	2.5

Table 10.3: Mean values (from top to bottom) of the momentum, longitudinal momentum, transverse momentum and rapidity distributions of the proton pairs measured in 11.5 A·GeV/c Au+Au collisions within a 9% to 6% centrality interval.

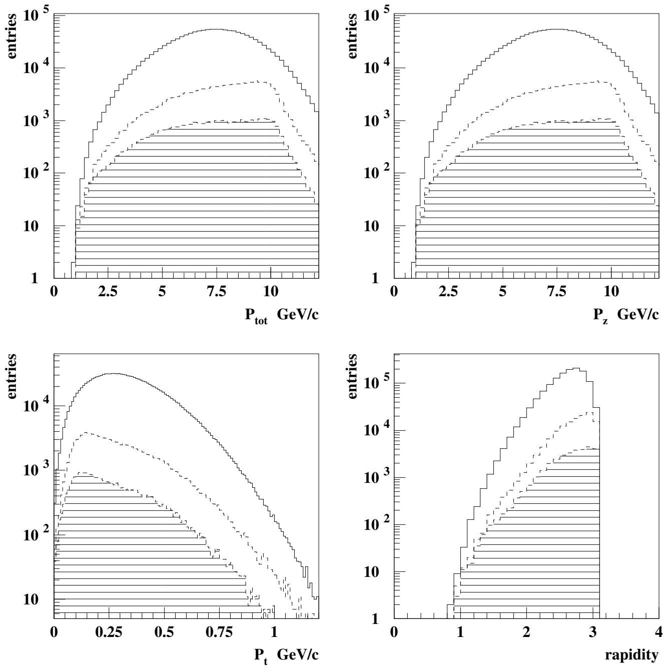

Figure 10.7: Some kinematic characteristics of the proton pairs in the 1994 data set with a 9% to 6% centrality cut . Top-left: total momentum; top-right: longitudinal momentum; bottom-left: transverse momentum; bottom-right: rapidity. The solid and dashed histograms represent the distributions for pair with q_{inv} $\leq$1.0 GeV/c and q_{inv} $\leq$ 0.1 GeV/c respectively. Distributions for pairs with q_{inv} $\leq$0.05 GeV/c are hatched.

Cut	Number of pairs
No cuts	2536961
$y \leq 3.1$	1521998
$y \leq 3.1 + \Delta$X cuts	1481763

Table 10.4: Number of proton pairs after cuts for Au+Au collisions at 11.5 AGeV/c with 9% to 6% centrality cut. See description in the text.

by the interplay of the changes of the nuclei overlap volume and momentum distributions, which affect the height of the correlation function in opposite ways. Note that in a framework of the model discussed in Chapter 2, the higher average momentum of the proton pairs in the $9-6\%$ centrality data should diminish the height of the correlation function, whereas if the source size is smaller in the less central collisions, this would tend to increase the height of the peak of the correlation function.

10.6 Reaction Plane Dependence

Flow in relativistic nucleus-nucleus collision was discovered and studied at Bevalac [65]. It was of great interest to see whether this phenomenon persists at higher energies. Almost 4π coverage and high segmentation of the E814/E877

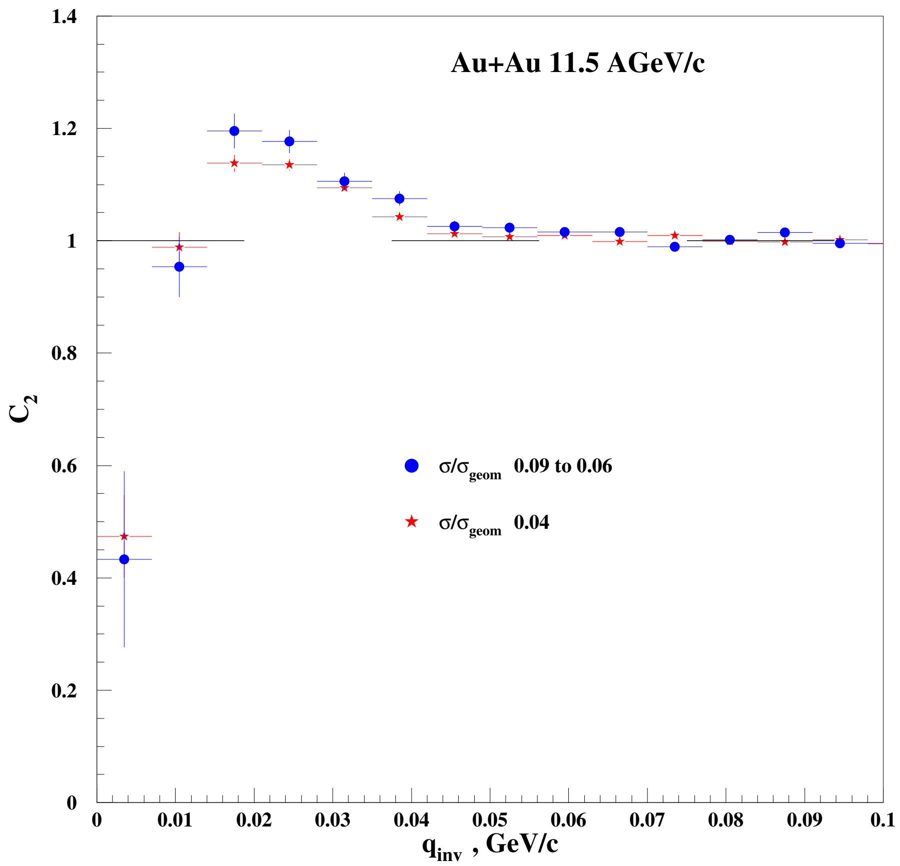

Figure 10.8: Two-proton correlation functions for the different centralities.

calorimeters provided the experiment with the possibility of studying flow phenomena. The initial E814 studies yielded negative results [49], after the technique of the event by event determination of the reaction plane using only calorimeters was pioneered [50] by E877, the existence of the collective nuclear flow component at AGS [66] energies was observed in azimuthal energy distributions by E877.

The method of event by event reaction plane determination without particle identification is based on the idea of performing a Fourier analysis on the transverse energy deposited in a fixed pseudo-rapidity window. The Fourier coefficients of the expansion are given by:

$$a_n = \frac{\sum_i \epsilon_i cos(n\phi_i)}{\sum_i \epsilon_i}, \quad b_n = \frac{\sum_i \epsilon_i sin(n\phi_i)}{\sum_i \epsilon_i} \tag{10.4}$$

where ϕ_i is the azimuthal angle of the i-th detector cell and ϵ_i is the energy deposited in that cell. The n=1 Fourier coefficients hold the information regarding the azimuthal orientation of the energy flow in the collision. The vector $\overrightarrow{flow} = (a_1, b_1)$ points in the direction where the most transverse energy is carried by the particles emmited from the collision zone. To put it another way, this vector is related to the azimuthal orientation of the impact parameter. Therefore, the azimuthal angle of the reaction plane may be determined as:

$$\psi_{reac} = tan^{-1}\left(\frac{b_1}{a_1}\right) \tag{10.5}$$

Since the discovery of flow at AGS energies, the determination of the event's reaction plane orientation became a standard part of the E877 off-line analysis. The value of each event's reaction plane angle is incorporated into the common data structures of the off-line analysis.

It was reported in Reference [28] that the parameters of the pion source created in Au+Au collisions at 10.8 AGeV/c appear to be different for pions emitted at different angles relative to the reaction plane. Since protons are the main carriers of the directed flow in nucleus nucleus collisions [50], it is interesting to check whether the parameters of the proton source, probed with the help of two-proton correlations, exhibit any asymmetries related to the reaction plane orientation. In this section we present the results of the first study of the proton correlation function dependence on the orientation of the reaction plane.

10.6.1 Details of the Analysis

Centrality selection:

Events with centrality within the interval from 9% to 6% of total geometrical cross section were selected for this analysis. The properties of this particular data set and parameters of the proton pairs were discussed in Section 10.4. From the naive geometrical considerations one would expect that the proton source will be at its most symmetric configuration at impact parameter zero and maximum asymmetry will be at maximal impact parameter. So in order to study the reaction plane dependence one would need to use the most peripheral event sample. The interval of centralities chosen for our analysis represents a compromise between the necessity to work with a high statistics sample and the desire to utilize the less central collisions.

Pair Selection

In addition to cuts described in Section 10.2.1 more selection criteria were introduced. Proton pairs were subdivided into several groups depending on the azimuthal angle of emission relative to the reaction plane angle. For true pairs, both protons in a pair were required to have an angle of emission relative to the reaction plane of this event to be within a certain interval. Figure 10.10 presents a visualization of the cuts on the angles relative to the reaction plane.

In the mixed events pool, every particle had its angle relative to the reaction plane stored as a part of its data structure. Subsequently, during the event mixing procedure, particles that make false pairs were required to satisfy the same cuts on the angle relative to the reaction plane as were imposed on the true pairs. Figure 10.9 shows the distributions of cosines of the particles' angles relative to the reaction plane for true and false pairs.

10.6.2 Results

Opposite Side vs Same Side

Pairs were divided into two subsets depending on the direction of their emission relative to the reaction plane. The "same side" subset was defined in the following way: each proton of a pair was required to have a positive cosine of the angle relative to the direction of the reaction plane. The "same side" subset yielded 753k proton pairs. The "opposite side" subset was comprised of pairs with a negative cosine of the angle relative to the reaction plane. It had 568k pairs. Figure 10.11 shows the two-proton correlation functions for these

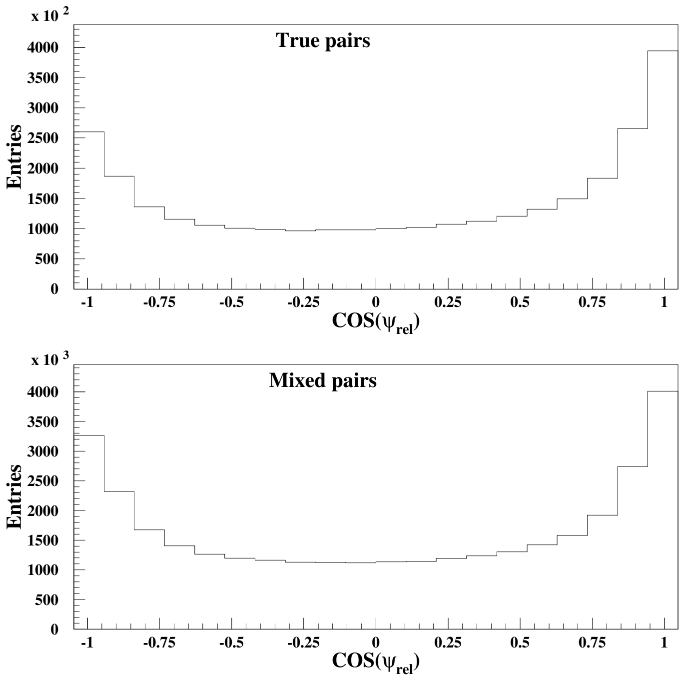

Figure 10.9: Distributions of cosines of angles relative to the reaction plane for protons from true and mixed pairs. See description in the text.

two subsets. One can conclude from the figure that there is no significant differences between the "same side" and "opposite side" correlation functions.

In-Plane vs Out-of-Plane

Another set of cuts was intended to probe the differences between particles emitted close to the reaction plane and particles emitted out of the reaction plane. The "in-plane" subset was defined as having the absolute value of the angle between the particle and the reaction plane direction smaller then $\pi/4$. When the angle was greater then $\pi/4$ pairs were labeled as emitted "out of plane". The same selection rules were applied to the mixed pairs. The "in-plane" sample yielded 596k events, the "out-of-plane", 582k pairs. Table 10.5 shows a summary of the mean values of the distributions of some kinematic varibles of the proton pairs selected by these cuts. Definition of the variables in the Table 10.5 are identical to the definitions of Table 8.1. From a comparison between Table 10.5 and Table 10.3 we concluded that the kinematical distributions of proton pairs after the cuts were similar to the parameters of the distributions of the data set before the cuts. The relative invariant momentum distributions are presented in Figure 10.12. One can see that no significant differences are observed between parameters of the q_{inv} distributions.

Figure 10.13 shows the two-proton correlation functions for these "in-plane" and "out-of-plane" subsamples. It can be seen from the Figure 10.13 that there are no statistically significant differences between "in-plane" and "out-of-plane" correlation functions.

However, both subsamples yielded correlation functions with peaks which

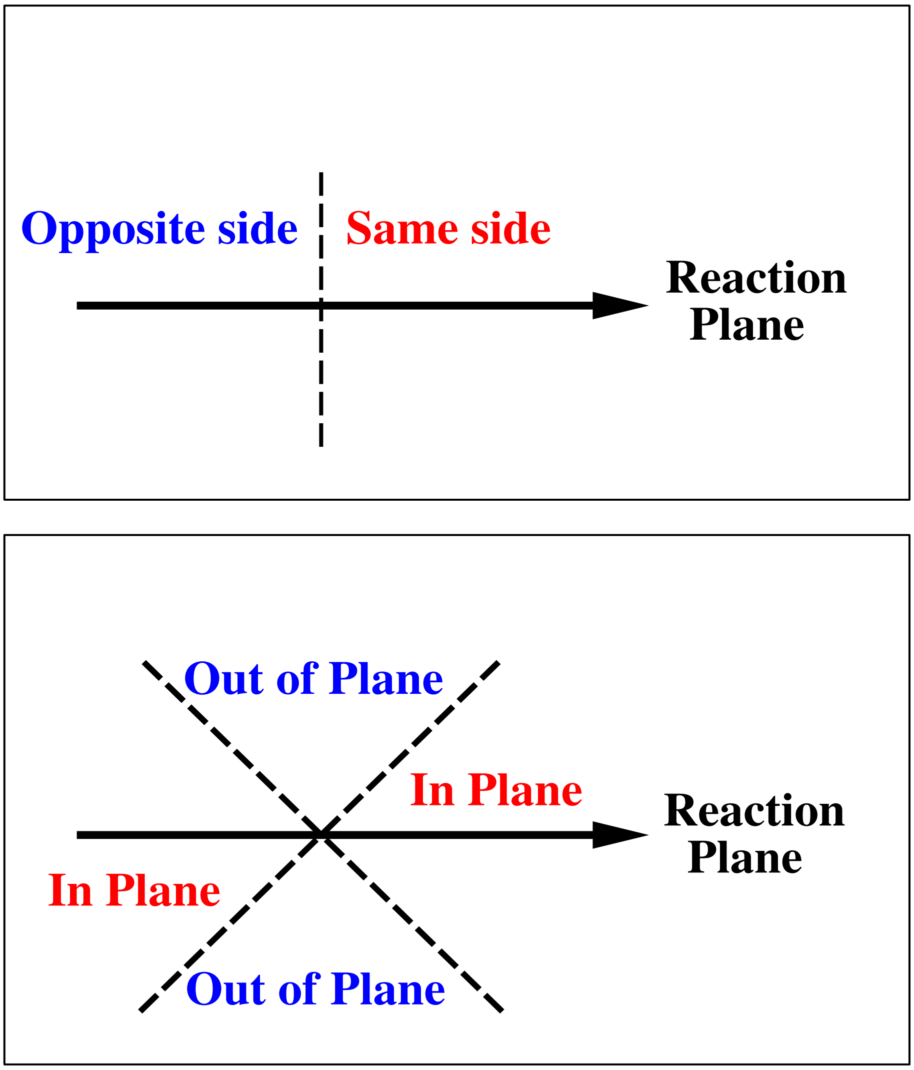

Figure 10.10: Schematic diagrams of the applied cuts on the orientation relative to the reaction plane. Upper panel: the "same" and "opposite" orientations relative to the reaction plane; Lower panel: "in-plane" and "out-of-plane" cuts.

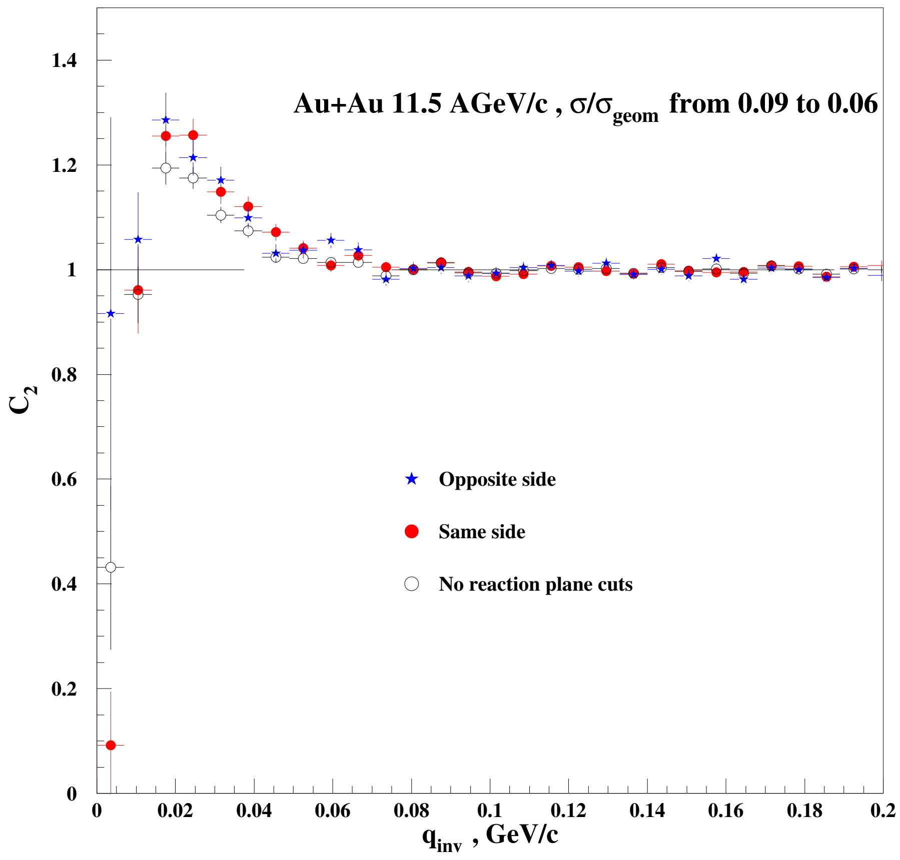

Figure 10.11: Two-proton correlation functions for the “same” and “opposite” orientations relative to the reaction plane.

Parameter	q_{inv} ≤0.05 GeV/c		q_{inv} ≤0.1 GeV/c		q_{inv} ≤1.0 GeV/c	
	In	Out	In	Out	In	Out
$< P >$, GeV/c	7.4	7.3	7.7	7.7	7.4	7.4
$< P_z >$, GeV/c	7.4	7.3	7.7	7.7	7.4	7.4
$< P_t >$, GeV/c	0.30	0.29	0.33	0.32	0.36	0.36
$< y >$	2.6	2.6	2.7	2.7	2.6	2.6

Table 10.5: Mean values (from top to bottom) of the momentum, longitudinal momentum, transverse momentum and rapidity distributions of the proton pairs measured in 11.5 A·GeV/c Au+Au collisions in the 9% to 6% centrality interval with reaction plane cuts. Columns labeled "In" give values for the "in-plane" cut, columns labeled "Out" give values of the "out-of-plane" cut.

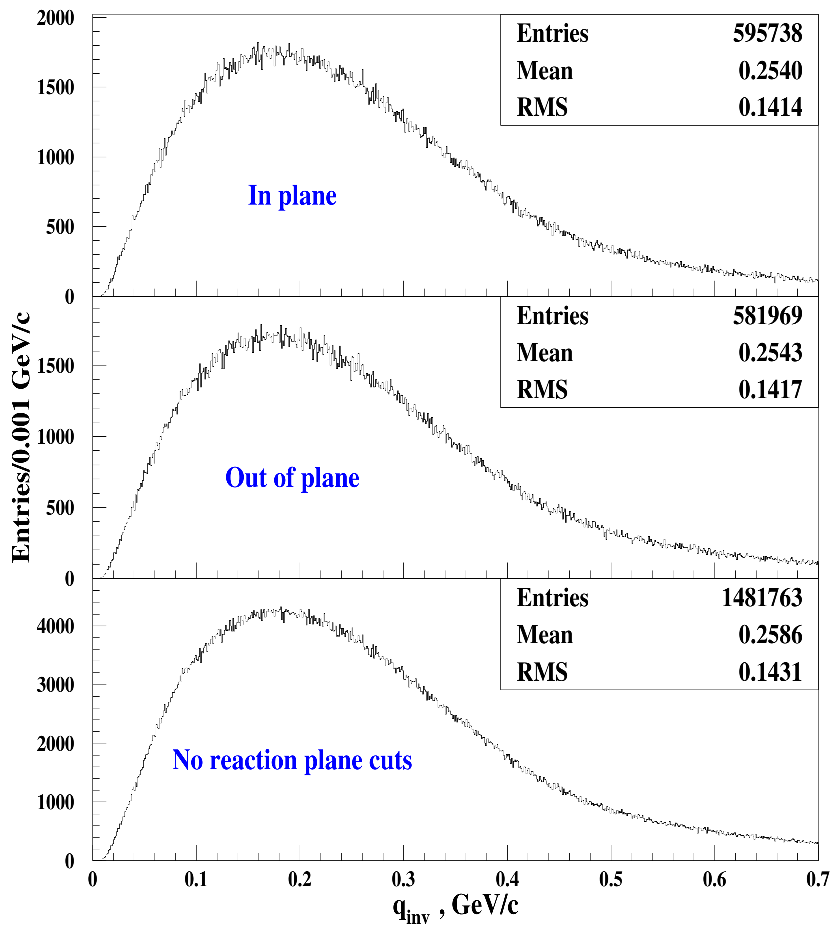

Figure 10.12: The q_{inv} distributions for the "in-plane" and "out-of-plane" orientations of proton pairs relative to the reaction plane. The correlation function obtained without reaction plane cuts is also shown.

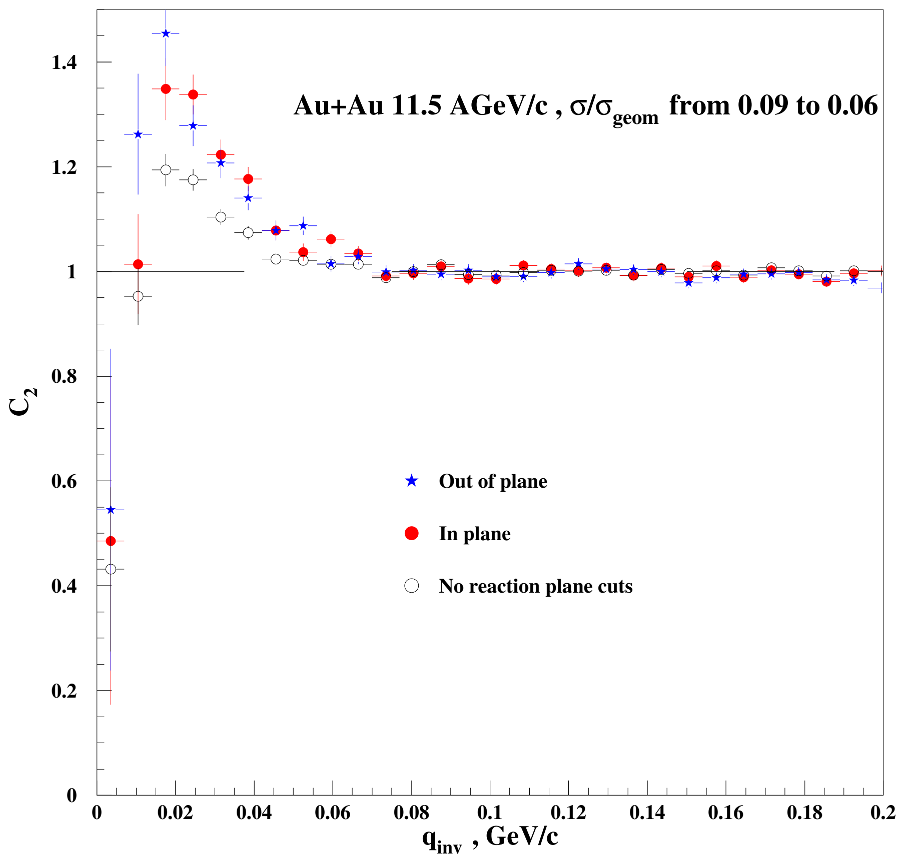

Figure 10.13: Two-proton correlation functions for the "in-plane" and "out-of-plane" orientations of proton pairs relative to the reaction plane. The correlation function obtained without reaction plane cuts is also shown.

are somewhat higher than the correlation function for the case when no cut on the angle relative to reaction plane was imposed. This may be explained by a correlation between position and direction of emission of the particles participating in directed flow. Reaction plane angle cuts select particles emmited in the same direction in the azimuthal plane which are likely to be on the same "side" of the flowing system and have a small relative separation. Another possibility is because particles emmitted at the same azimuthal direction relative to the reaction plane are "co-moving" and hence may interact with each other longer.

In order to check that the effect seen in Figure 10.13 is related to the pair orientation relative to the reaction plane and is not induced by some possible dynamical constraints imposed by the cuts themselves we performed several tests.

Test1. Random Reaction Planes. Protons from the same event were assigned random angles relative to the reaction plane. In short, each proton has its own reaction plane which was randomly oriented. In this way any reaction plane dependencies (whatever their physical origin might be) of proton pairs are destroyed; but all effects introduced by the selection criteria remain. Figure 10.14 shows the result of this test. It can be seen from the figure that in the case of a random reaction plane assignment, the correlation functions obtained with "in-plane" and "out-of-plane" cuts have peak heights similar to that of the correlation function without any reaction plane cuts.

Test2. Absolute Angle of the Reaction Plane. We performed another test in order to check whether the origin of the difference in the height

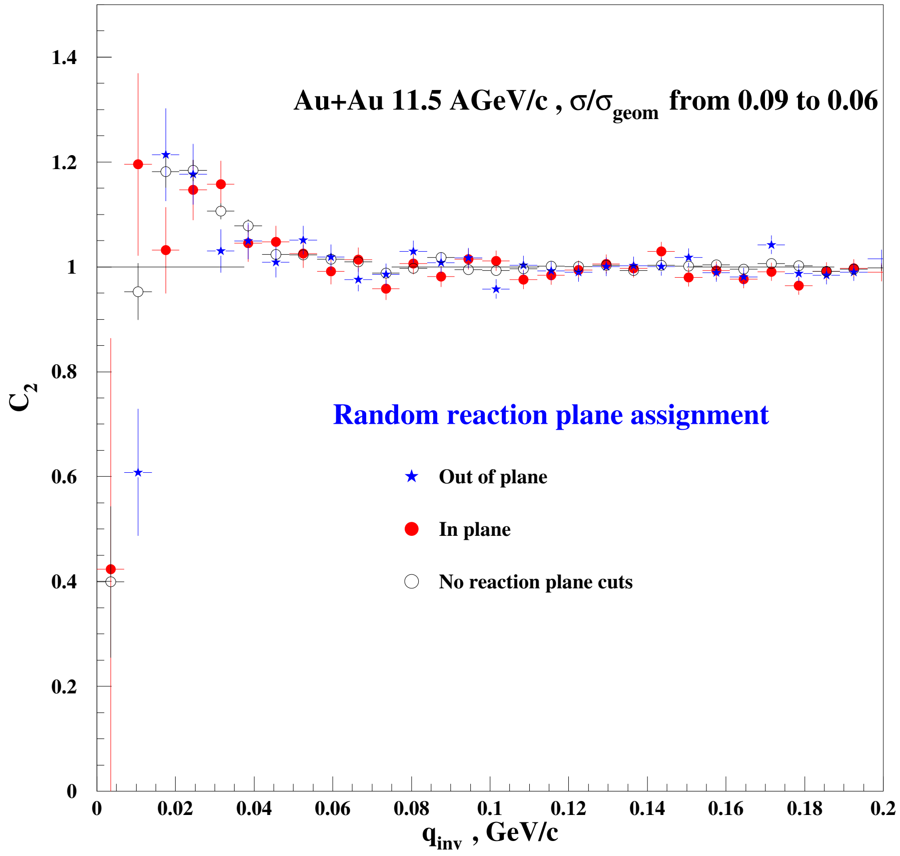

Figure 10.14: Two-proton correlation functions for the "in-plane" and "out-of-plane" orientations of proton pairs relative to the reaction plane. The direction of the reaction plane has been randomized. See description in the text.

of the correlation functions with and without cuts on the angle of emission relative to the reaction plane comes from some methodical reasons. The value of the proton's angle relative to the reaction plane was substituted by the reaction plane angle itself. In this configuration "in-plane" and "out-of-plane" plane cuts that we described earlier became cuts on the orientation (horizontal and vertical respectively) of the reaction plane relative to the coordinate system of the E877 spectrometer (see Chapter 3). This test probes possible forward spectrometer acceptance effects induced by different orientations of the reaction plane relative to the collimator. The resulting correlation functions are shown in Figure 10.15. On this Figure stars denote vertical orientations of the reaction planes (within 90 degree cone around y-axis), filled circles denote horizontal orientations of the reaction plane (within the 90 degree cone around x-axis).

Test3. "Same" Reaction Plane in the Mixed Pairs. In this test, during event the mixing procedure, "false" protons pairs were taken from the events with similar orientation of the reaction plane in the E877 coordinate frame. Similar means that reaction plane directions differ by no more than 45 degrees. No reaction plane cuts were imposed on "true" pairs. Open circles in Figure 10.15 denote the correlation function which was a result of the third test.

It can be seen from Figures 10.14 and 10.15 that tests 1, 2 and 3 yield correlation functions with peak heights similar to the case where no cuts on the azimuthal angle of emission were applied on protons. We conclude that the difference in the correlation functions with and without cuts on the orientation

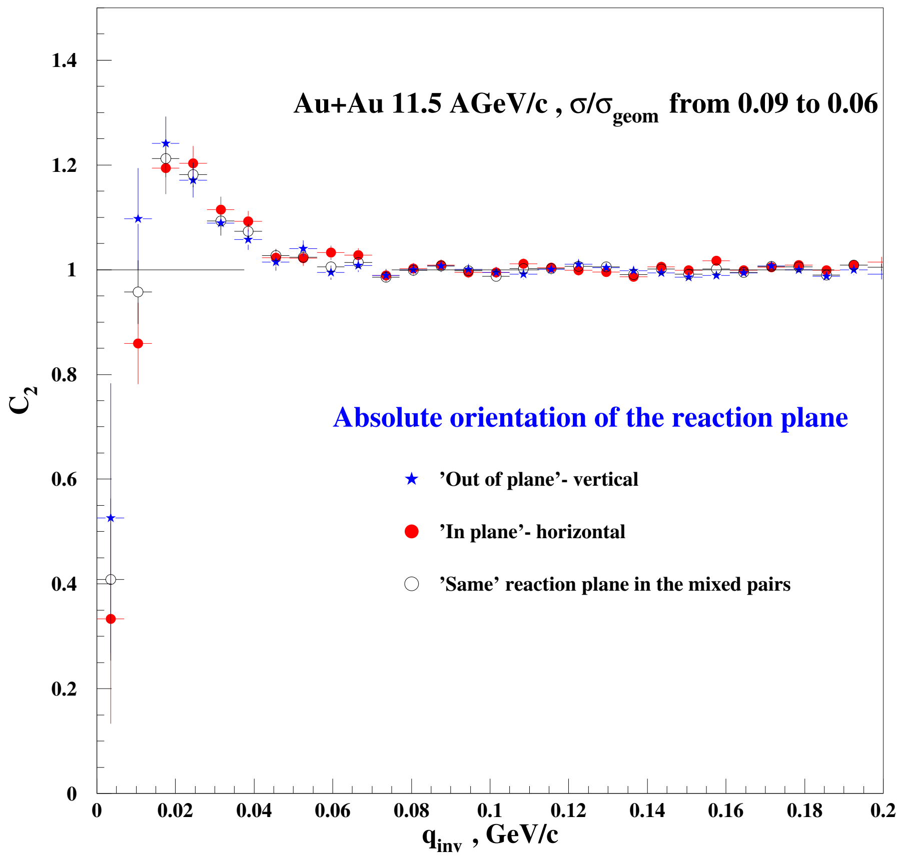

Figure 10.15: Two-proton correlation functions for the horizontal and vertical orientations of the reaction planes in the lab frame. See description in the text.

of pairs relative to the reaction plane, shown on Figure 10.13, is not induced by artifacts of the analysis but is likely to be linked, via angle of emission relative to the reaction plane, to the momentum-space correlations of the flowing nuclear matter. We also conclude that the two-proton correlation function does not exhibit significant differences when a proton source is viewed from different sides of the reaction plane, which may indicate azimuthal symmetry of the source.

Chapter 11

Proton-Deuteron Correlations

In this Chapter we will discuss the analysis of the proton-deuteron correlations measured by the E877 Collaboration in 10.8 A·GeV/c Au+Au collisions at AGS BNL during the Fall run of 1993. The details of the event selections were discussed in Chapter 4 and track selection procedures and details of particle identification were presented in Chapter 5. Proton-deuteron correlations are believed to provide additional information about baryon freeze-out and light nuclei production [27, 67, 68] in a collision. It can also be seen as a natural bridge between proton-proton correlations and techniques involving measurements of the relative yields of deuterons and protons. This type of measurement has very little to do with "interferometry"- the quantum interference effects of traditional HBT measurements are absent here. Nevertheless, information about the geometrical structure of the source is encoded via final state interactions in the correlation function. This type of correlation is due to Coulomb and strong interactions between the proton and deuteron and, hence, is also sensitive to the space-time dimensions of the source [27, 26].

Methodologically, from the point of view of the analysis (and interpretation) procedure, p-d correlations are very similar to p-p correlations. Because the two particles are non-identical and generally have very different lab momenta while having a low relative momentum in the pair's center of mass, proton-deuteron correlations are less affected by the two-track reconstruction inefficiency(see Chapter 6). More details of the deuteron identification and analysis of deuteron single particle distributions performed by the E877 Collaboration can be found elsewhere [69].

11.1 Description of the Data Set

The definitions of the used variables and cuts were identical to the definitions utilized in 1993 and 1994 proton pairs analysis which was described in Chapter 8. Note that instead of q_{inv}, the momentum of a particle in the pair center of mass frame; denoted as p_{cm}, was used. Recalling the definition given by Equation 6.3, $p_{cm} = P_{cm}/2$.

The 1993 data set yielded about 65k pairs. Figure 11.1 shows the distribution of some kinematic variables of the proton-deuteron pairs for the different ranges of p_{cm}. Table 11.1 shows a summary of the averaged values for the distributions presented on Figure 11.1. Figure 11.2 shows the measured correlation function.

Parameter	$p_{cm} \leq$0.05 GeV/c	$p_{cm} \leq$0.1 GeV/c	$p_{cm} \leq$1.0 GeV/c
$< P >$, GeV/c	6.9	7.3	8.6
$< P_z >$, GeV/c	6.9	7.3	8.6
$< P_t >$, GeV/c	0.34	0.36	0.40
$< y >$	2.3	2.4	2.4

Table 11.1: Mean values (from top to bottom) of the momentum, longitudinal momentum, transverse momentum and rapidity distributions of the proton-deuteron pairs measured in 10.8 A·GeV/c Au+Au collisions at 10% centrality.

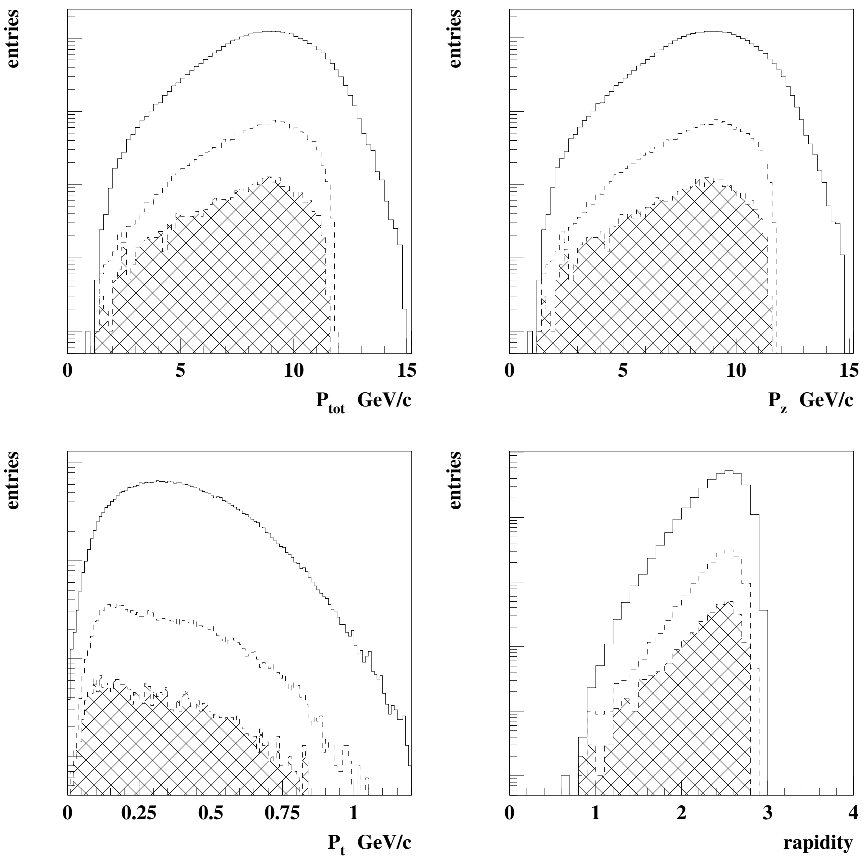

Figure 11.1: Some kinematic characteristics of the proton-deuteron pairs in the 1993 data set with a 10% centrality cut . Top-left: total momentum; top-right: longitudinal momentum; bottom-left: transverse momentum; bottom-right: rapidity. The solid and dashed histograms represent the distributions for pairs with p_{cm} $\leq$1.0 GeV/c and p_{cm} $\leq$ 0.1 GeV/c respectively. Distributions for pairs with p_{cm} $\leq$0.05 GeV/c are hatched.

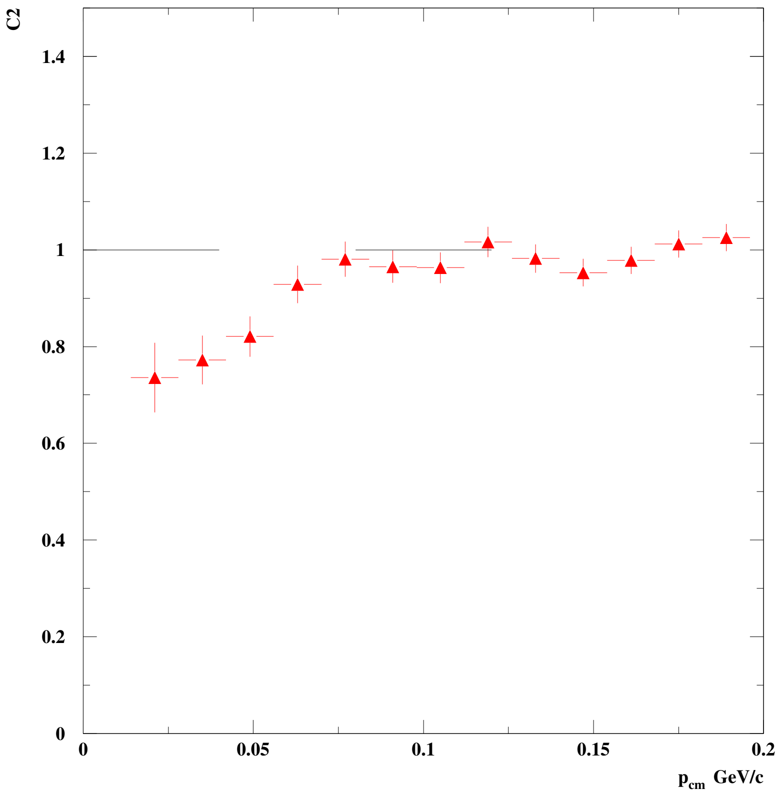

Figure 11.2: Measured proton-deuteron correlation function for Au+Au central collisions. See description in the text.

11.2 Model Calculations

11.2.1 Static Thermal Source

In order to gain some basic insight into the generic dependences of the proton-deuteron correlation function we have performed calculations using a model similar to the one described in Chapter 2. The source was assumed to have some fixed radius and lifetime. It was emitting protons and deuterons with some arbitrary, and in general different, temperatures. Actual temperatures for protons and deuterons for our calculations were chosen to be close to the experimentally measured values [69]. The simplest prescription was to take some measured proton temperature and to assign a twice higher temperature for deuterons. This factor of two comes from the simple minded coalescence picture of deuteron formation and momentum conservation. Note that no particular mechanism of deuteron formation was assumed. Deuterons were just "produced" by the source.

Figure 11.3 shows an example of the proton-deuteron correlation function for two different source sizes. The response of the correlation function on the radius parameter to the change of the source radius is evident. Keep in mind, though, that no experimental effects like momentum resolution or acceptance were introduced into this calculation. The sensitivity of the proton-deuteron correlation function to the temperature of the source is illustrated by Figure 11.4.

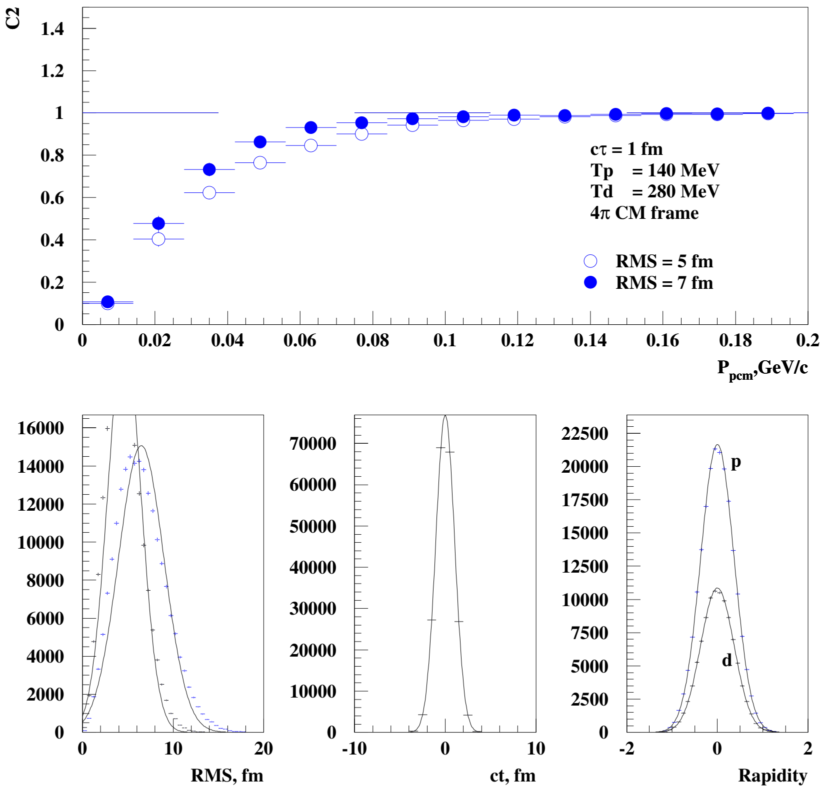

Figure 11.3: Upper panel: Proton-deuteron correlation function for different radius Gaussian sources. Lower panels: Source parameter distributions: (from left to right) three-dimensional rms radii of the sources, emission time, rapidity of the particles.

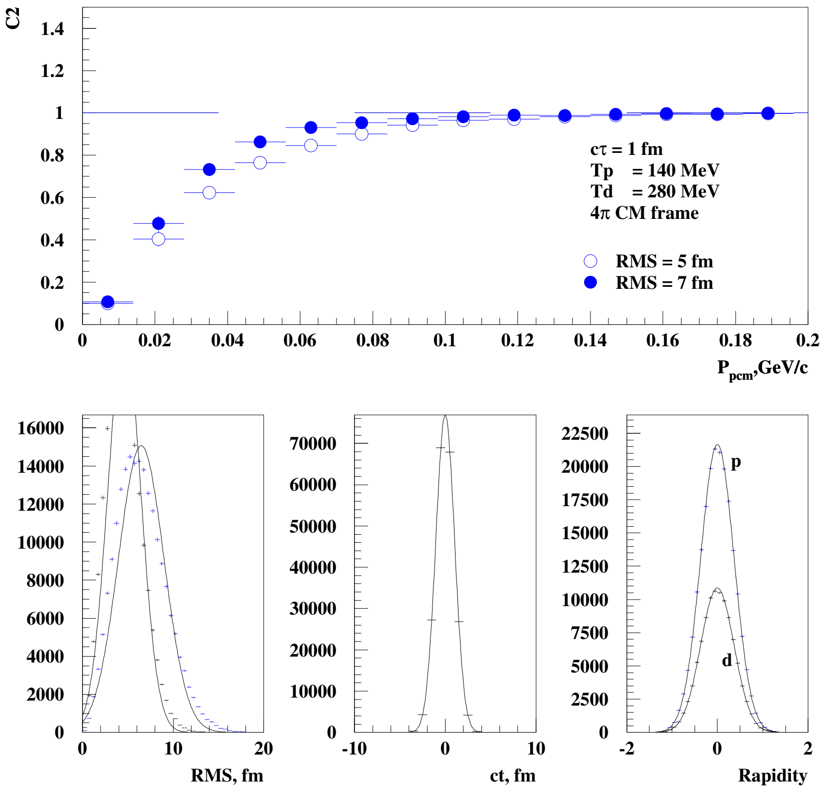

Figure 11.4: Upper panel:Proton-deuteron correlation function for Gaussian sources with different temperatures. Lower panels: Source parameters distributions: (From left to right) three-dimensional rms radii of the sources, emission time, rapidity of the particles.

11.3 RQMD + Coalescence

Interpretation of proton-deuteron correlations with the help of the cascade models is even more complicated because none of them takes into account nuclear bound states (e.g. deuterons) dynamically. To overcome this problem we used a "coalescence after-burner" based on a formalism developed by R. Mattiello [70] to generate deuterons. In this approach the formation probability of light baryon clusters was calculated by projecting a nucleon phase-space distribution at freeze-out on cluster wave functions using the Wigner function formalism. Therefore, the space-time distributions of deuterons formed as a results of this procedure are very similar to the freeze-out space-time distributions of nucleons.

In order to take into account final state interactions between the proton and deuteron and calculate the correlation function we have used a code based on the Lednicky-Lyuboshitz formalism [24]. The calculations included a complete description of the geometry of the E877 spectrometer and the single bend model of particle propagation through the magnet. Fiducial volume cuts imposed on pairs were exactly the same as in the analysis of the real data. Deadened regions of the spectrometer and granularity of the TOFU (see Chapter 3) were taken into account. Momentum resolution, following the prescriptions of Reference [56], was incorporated into calculations. The requirement of the non-sharing of the same TOFU slat and track separation cuts were imposed on pairs of simulated particles.

Figure 11.5 shows the measured correlation function along with a model correlation function.

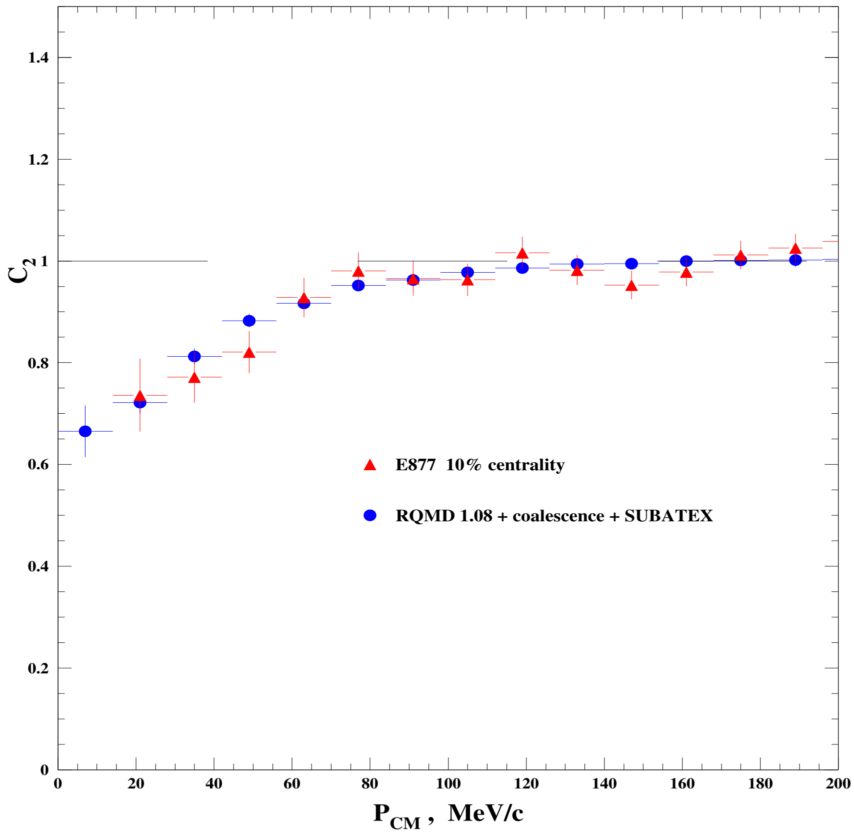

Figure 11.5: Measured (triangles) one-dimensional correlation function for p-d pairs and coalescence model results based on RQMD input (circles). See description in the text.

Chapter 12

Conclusions

12.1 Summary

The E814/E877 Collaborations at the Alternating Gradient Synchrotron at Brookhaven National Laboratory performed experiments for measuring two-particle correlation functions in the forward rapidity region utilizing 14.6 AGeV/c Si and, 10.8 AGeV/c and 11.5 AGeV/c Au beams.

In this thesis we present our analysis of two-proton correlation functions measured in Si+Pb collisions and Au+Au collisions. Also measurements of the proton-deuteron correlation function in Au+Au collisions are presented.

Proton Correlations in Si+Pb Collisions The position and height of the peak the two-proton correlation function at 20 MeV/c is consistent with the preliminary analysis of the correlation function [37] measured by the E802 Collaboration in 14.6 A·GeV/c Si+Au collisions at $\sigma_{trig}/\sigma_{geom} \approx 12\%$, though the E802 measurement was performed at mid-rapidity and our measurement is at forward rapidity. The shape of the correlation function is in good agreement with model calculations based on the event generator RQMD(v1.08) [38, 39].

Proton Correlations in Au-Au Collisions. We have performed the first measurements of the proton-proton correlation function for this system at AGS energies; no data for comparison is presently available. The height of the peak of the two-proton correlation function in Au+Au collisions is lower that that of the Si+Pb collisions, indicating a larger source size for the heavier colliding system, probably a natural consequence of utilizing of a heavier projectile. Calculations based on RQMD are in qualitative agreement with the measurement even though some tendency for under-prediction of the peak height by the model is observed.

Study of the centrality dependence of the proton correlation function indicates that the source size in the most central collision, 4% of the geometrical cross section, is larger then the source size found in the more peripheral collisions of 9 to 6% centrality.

Study of the dependence of the two-proton correlation function on the orientation of the proton pair relative to the reaction plane was also performed. There is a difference between the correlation functions with and without cuts on the orientation of the pairs relative to the reaction plane. It likely that the difference is related to the momentum-space correlations induced by the flow phenomenon. We also conclude that the two-proton correlation function does not exhibit significant differences when the proton source is viewed from different sides of the reaction plane, which may indicate azimuthal symmetry of the source.

Proton-Deuteron Correlations in Au+Au Collisions The first measurements , in relativistic heavy-ion collisions, of the proton-deuteron correlation function was performed. The new approach for model calculations of the deuteron-proton correlation function was suggested during this analysis. The shape of the experimental correlation function is well reproduced by the model calculations.

12.2 Outlook

It is clear that the new, upcoming dataset from the 1995 run will open new possibilities into the two-particle correlations studies in general and two-proton correlations in particular. The available statistics will be increased by an order of magnitude compared to the 1994 run. Also the quality of the dataset is expected to be further improved. It will allow correlation analyses of rare particles like kaons. High statistics measurements of the correlation function of positive and negative kaons will be of great interest.

The dependence of the proton (and other particles) correlation function on the reaction plane needs to be studied in more detail. It is clearly a unique feature of the E877 correlation analysis and so far has not been utilized in, or even available for, studies of the correlation functions by any other experiments. Because the reaction plane is a natural plane of symmetry in the collision it is self-evident that the ability to determine it is of major importance for the analysis aimed to explore the geometrical properties of the colliding zone.

A multi-dimensional approach to the analysis of the two proton correlation function in a spirit similar to the multi-dimensional analysis of meson correlations is presently missing. To the best of our knowledge there have been no theoretical studies of even the feasibility of such measurements. It might happen that most of the experimentally accessible information on baryon freeze-out correlations may be hidden from current studies because of inadequate variables used in analysis. Clearly, more effort is needed in this direction.

The complexity of heavy-ion collisions requires utilization of different particles as probes of the reaction zone. Simultaneous measurements of the correlation functions of different particles are required to obtain a more complete picture of the reaction zone. Study of unlike particles correlations has to be performed more systematically. This type of measurement has very little to do with "interferometry", the information about geometrical structure of the source is encoded via final state interactions. It may seem difficult to decode but it is definitely worth trying and deserves a more systematic study. It is also useful in understanding the role of the final state interactions, Coulomb for example, in the physics of heavy-ion collisions.

As was recently pointed out in Reference [27] the correlations of non-identical particles, in principle, are sensitive to the time order of the system freeze-out. Some particles like, for example, kaons can decouple earlier than others, for example protons. Correlations of unlike particles may carry information about this sequence. The importance of this idea was immediately realized by the low energy nuclear physics community and applied to heavy ion reactions at GANIL. Preliminary results obtained by INDRA and ORION collaborations indicates that the method works at GANIL energies. However it is not clear yet to what extent this method is applicable at relativistic energies and more theoretical studies are required.

Simultaneous extraction of the source parameters such as temperature, chemical potential, source size, etc. at freeze-out was suggested recently [71, 72]. This approach requires unification of single-particle measurements and correlations in one analysis framework may yield a more comprehensive insight and provide more constraints on the models.

Bibliography

[1] T.D. Lee and G.C. Wick, Phys. Rev. D 9 (1974) 2291; T.D. Lee, "A possible New Form of Matter", in Report of the workshop on BeV/Nucleon Collisions of Heavy Ions-How and Why, Bear Mountain 1974 (BNL No 50445),1.

[2] B. Mueller, Nucl. Phys. A 590 (1995) 3c.

[3] T.J. Hallman and J. Thomas, Nucl. Phys. A 590 (1995) 399c.

[4] G.E. Brown and M. Rho, Phys. Rev. Lett. 66 (1991) 2720; G.Q. Li, C.M. Ko and G.E. Brown, Phys. Lett. B 363 (1995) 35.

[5] Proc. of the Twelfth Int. Conference on Ultra-Relativistic Nucleus-Nucleus Collisions, eds. P. Braun-Munzinger et al, Nucl. Phys. A 610 (1996).

[6] J.W. Harris, B. Muller, "The search for the Quark-Gluon Plasma", Annu. Rev. Nucl. Part. Sci. 46 (1996) 71.

[7] W. Bauer,C.-K. Gelbke,S. Pratt., Ann. Rev. Mod. Phys. 42 (1992).

[8] D.H. Boal, C.-K. Gelbke, B.K. Jennings., Rev. Mod. Phys. 62 (1990) 553.

[9] W. A. Zajc, “Two pion Correlations in Heavy Ion Collisions” PhD thesis, U. of California, (1982) LBL-14864.

[10] W.A. Zajc et al.,Phys Rev C 29 (1984) 2173.

[11] T. Abbot et al.,Phys. Lett. 69 (1992) 1030,

[12] Y. Akiba et al., Phys. Rev. Lett. 70 (1993) 1057.

[13] J. Barrette et. al, Phys. Lett. B 333 (1994) 33.

[14] T. Alber, NA35 and NA49 Collaborations, Nucl. Phys. A 590 (1995) 453c; T. Alber et al., Phys Rev Lett. 75 (1995) 3814.

[15] H. Beker et al., Z. Phys., C 64 (1994) 209.

[16] Y. Pang, T.J. Shlagel, S.H. Kahana, Phys. Rev. Lett. 68 (1992) 2743.

[17] X.N. Wang, M. Gyulassy, Phys. Rev D 44 (1991) 3501.

[18] B. Anderson, et al., Nucl. Phys. B 281 (1987) 289.

[19] K. Werner, Phys. Rep. 232 (1993) 87.

[20] H. Sorge et al., Phys. Lett. B 289 (1992) 6.

[21] E. Fermi, Progress Theor. Phys. 5 (1950) 570.

[22] E. Fermi, Phys. Rev. 81(1951) 683.

[23] S. Koonin, Phys. Lett. B 70 (1977) 43.

[24] R. Lednicky, V.L. Lyuboshits, Sov. J. Nucl. Phys. 35 (1982) 770.

[25] A. Mekijan, Phys. Rev. Lett. 38 (1977) 640.

[26] B. Jennings, D. Boal, J. Shillcock, Phys. Rev. C 33 (1986) 1303.

[27] R. Lednicky, V.L. Lyuboshits, B. Erazmus, D. Nouais, Phys. Lett. B 373 (1996) 30.

[28] D. Miskowiec et al., E877 Coll., Nucl. Phys. A 590 (1995) 473c.

[29] D. Miskowiec et al., E877 Coll., Nucl. Phys. A 610 (1996) 227c.

[30] J. Barrette et. al, submitted to Phys. Rev. Lett.

[31] P. Braun-Munzinger, J. Stachel, J.P. Wessels, N. Xu, Phys. Lett. B 344 (1995) 43.

[32] I. G. Bearden et al. submitted to Phys. Rev. Lett., Nov. 5, 1996; CERN Preprint CERN-PPE/96-163.

[33] O. Vossnack, E802 Coll., Proc. Int. Workshop Heavy Ion Physics at the AGS 93, eds. G.F.S. Stephans, S.G. Steadman and W.L. Kehoe, MITLNS-2158, p. 380.

[34] T.C. Awes et al., Z.Phys. C 65 (1995) 207.

[35] J. Barrette et al., Phys. Rev. Lett. 64 (1990) 1219.

[36] J. Barrette et al., Phys. Rev. C 64 (1992) 819.

[37] G.S.F. Stephans, E802 Coll., Proc. Int. Workshop Heavy Ion Physics at the AGS 93, eds. G.F.S. Stephans, S.G. Steadman and W.L. Kehoe, MITLNS-2158, p. 371.

[38] H. Sorge, H. Stöcker, and W. Greiner, Nucl. Phys. A 498 (1989) 567c; H. Sorge, R. Mattiello, H. Stöcker, and W. Greiner, Phys. Rev. Lett. 68 (1992) 286.

[39] H. Sorge, A. von Keitz, R. Mattiello, H. Stöcker, and W. Greiner, Phys. Lett. B 243 (1990) 7.

[40] S. Pratt, Phys. Rev. Lett. 53 (1984) 1219.

[41] S. Pratt et al., Phys. Rev. C 36 (1990) 2646.

[42] M.L. Allaberdin,R. Lednicky,V.L. Lyuboshits,B.S. Yuldashev., Sov.J.Nucl.Phys. 46(6) (1987) 1068.

[43] J. Barrette *et al* , Z. Phys. C 59 (1993) 211.

[44] D.G.Cassel *et al* , Nucl. Instr. Methods, A 185 (1981) 235.

[45] GEANT Detector Description and simulation, Application software group, Computing and Network Division, CERN Geneva, Switzerland.

[46] W.G. Gong, W. Bauer, C.-K. Gelbke, S. Pratt., Phys. Rev. C43(2) (1991) 781.

[47] B.V. Jacak(for NA44 collaboration)., Nucl. Phys. A590 (1995) 215c.

[48] G.J. Kunde et al., Phys. Rev. Lett. 70(17) (1993) 2545.

[49] G. David, 'Global Variables, Flow and Inclusive Spectra in Relativistic Heavy Ion Collisions', PhD thesis, SUNY Stony Brook, (1991).

[50] Y. Zhang, 'Transverse Energy Distributions, Global Event Shapes, and Flow Study in Ultra-relativistic Heavy Ion Collisions', PhD thesis, SUNY Stony Brook, (1995).

[51] B. Hong, 'Kaon Production near Zero Transverse Momentum in Relativistic Heavy Ion Collisions', PhD thesis, SUNY Stony Brook, (1995).

[52] Y. Kwon, private communications; Y.Kwon, 'Momentum Resolution', E877 memo (1996), unpublished.

[53] M. Trzaska, private communications

[54] '1994 Research instrumentation catalog', LeCroy Corporation.

[55] M. Pentia, G. Iorgovan, A. Mihul, 'Multiple scattering error propagation in particle track reconstraction',IFA-HE-124-1994, LANL preprint number HEP-EX-9406006

[56] D. Miskowiec, 'Momentum Resolution of the E877 Spectrometer - Calculation', E877 memo (1996), (unpublished).

[57] T.W. Piazza, 'Proton and pion distributions from Au+Au Collisions at 10.8 AGeV/c', PhD thesis, SUNY Stony Brook, (1997).

[58] W.C. Chang and S. Voloshin,'Proton and Pion Production Relative to the Reaction Plane in Au+Au Collisions at 10.8 AGeV/c', E877 Collaboration note, SUNYSB-96-003, (unpublished).

[59] S. Pratt, T. Csorgo and J. Zimanyi., Phys. Rev. C42 (1990) 2646.

[60] S. Pratt et al., Nucl. Phys. A566 (1994) 103c.

[61] S.A. Voloshin, W.E. Cleland, Phys. Rev. C 54 (1996) 3212.

[62] J. Dee, 'Baryon distributions in high-energy nuclear collisions', PhD thesis, SUNY Stony Brook, (1995).

[63] N. Xu, E814 Coll.,Proc. Int. Workshop Heavy Ion Physics at the AGS 93, eds. G.F.S. Stephans, S.G. Steadman and W.L. Kehoe, MITLNS-2158, 362.

[64] T.K. Hemmick, E814 Coll.,Proc. Int. Workshop Heavy Ion Physics at the AGS 93, eds. G.F.S. Stephans, S.G. Steadman and W.L. Kehoe, MITLNS-2158, 204.

[65] H-A. Gustafsson et al., Phys. Rev. Lett. 52 (1984) 1984.

[66] J. Barrette et. al, Phys. Rev. Lett. 73 (1994) 2532.

[67] B. Erazmus et al., Internal Report Nantes/SUBATEX 96-03.

[68] S.Y. Panitkin, E877 Coll, Proc. Int. Conf. Heavy Ion Physics at the AGS 96, eds. C.A. Pruneau et al., WSU-NP-96-16, 1996, 147.

[69] S. Johnson, E877 Coll, Proc. Int. Conf. Heavy Ion Physics at the AGS 96, eds. C.A. Pruneau et al., WSU-NP-96-16, (1996) 112.

[70] R. Mattiello et al., preprint nucl-th/9607003, accepted for publication at Phys. Rev. C; R. Mattiello et al., Proc. Int. Conf. Heavy Ion Physics at the AGS 96,eds. C.A. Pruneau et al., WSU-NP-96-16, (1996) 88.

[71] S. Chapman, J.R. Nix, Phys. Rev. C54 (1996) 866.

[72] J. Helgesson, T. Csorgo, M. Asakawa, B. Lorstad, preprint nucl-th/9506006.

Appendix A

Beam Momentum Measurements

A direct, absolute measurement of the AGS gold beam momentum was performed by the E877 collaboration during the heavy ion run of 1993. Results obtained by the simple method of charge summation of pad cells are in good agreement with the results obtained by tracking analysis. The charge sum method gives an accuracy of about 0.5% and is limited by the accuracy of the determination of hit position and beam pitch angle. On the other hand, this method can be used on-line and it does not heavily rely on the survey data [1]. In this Appendix we will describe the details of this method.

A.1 Relevant Details of the Experimental Setup

The experiment 877 setup for measuring the beam momentum is shown in figure 3.6. Incident beam trajectories before the target are measured by silicon

[1] In fact the only survey constant needed is the distance between $DCII$ and $DCIII$ which can be easily measured with sufficient accuracy ($\sim 1mm$).

microstrip Beam Vertex detectors($BVER's$) with 50 μm spatial resolution. These provide the incident angle of beam particles with an angular resolution of about 20 μrad in the xz -plane. Beam particles bent by a dipole magnet ($D10$) are detected by two drift chambers($DCII$ and $DCIII$) with x position resolutions of 400 and 800μm respectively[2]. Each drift chamber consists of six wire planes for x and one pad plane for y position measurement. A more detailed description of the E877 setup can be found in Chapter 3.

A.2 Calculating the Beam Momentum

During the Fall 93 run of the E877 experiment, the following simple method was used for determination of the beam momentum. The hit pattern of beam particles was detected by using the charge sum of pads of both drift chambers. The measured pulse height sum as a function of wire number is presented in figure A.1.

Data were taken first with $D10$ turned off, then with the $D10$ current set to 1750 and 2650 Amperes. These current settings have been used during magnetic field measurements in $D10$ previously so field profiles are well known[3]. A detailed description of the magnetic field measurement is in Appendix B. One example of the field profile for $I = 2650A$ is shown in figure A.2.

---

[2]The position resolutions for the minimum ionizing particles are 250 and 350μm respectively.

[3]A current value of 2650A is very close to the maximum current in $D10$. The 1750A setting was used to check the systematics.

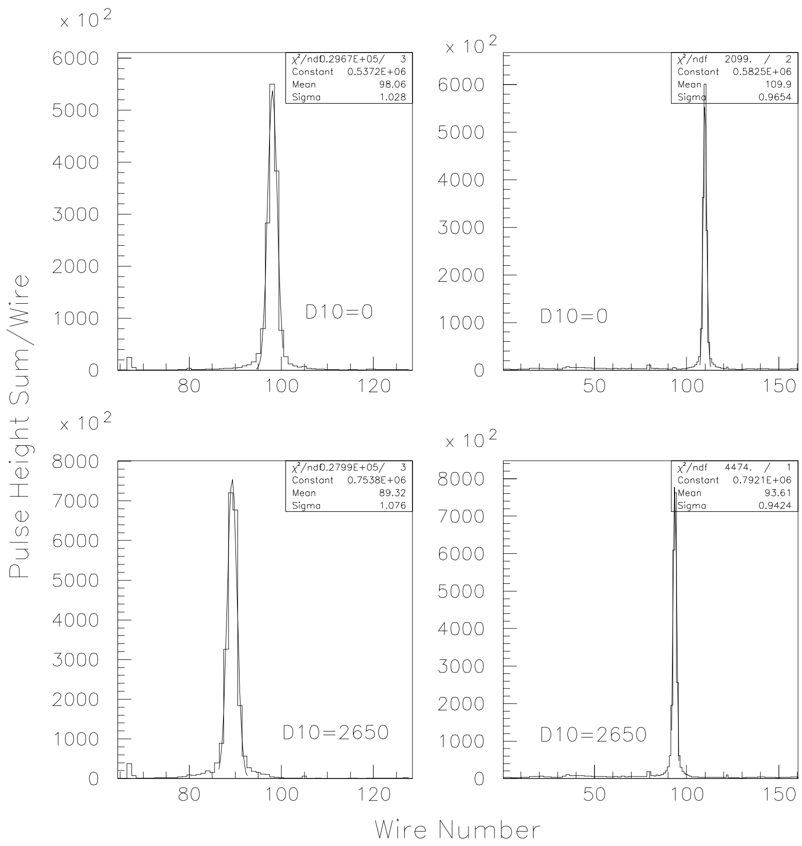

Figure A.1: Hit pattern of beam in $DCII$(left) and $DCIII$(right) obtained by the charge sum of pad cells for the currents 0 and 2650 A in $D10$.

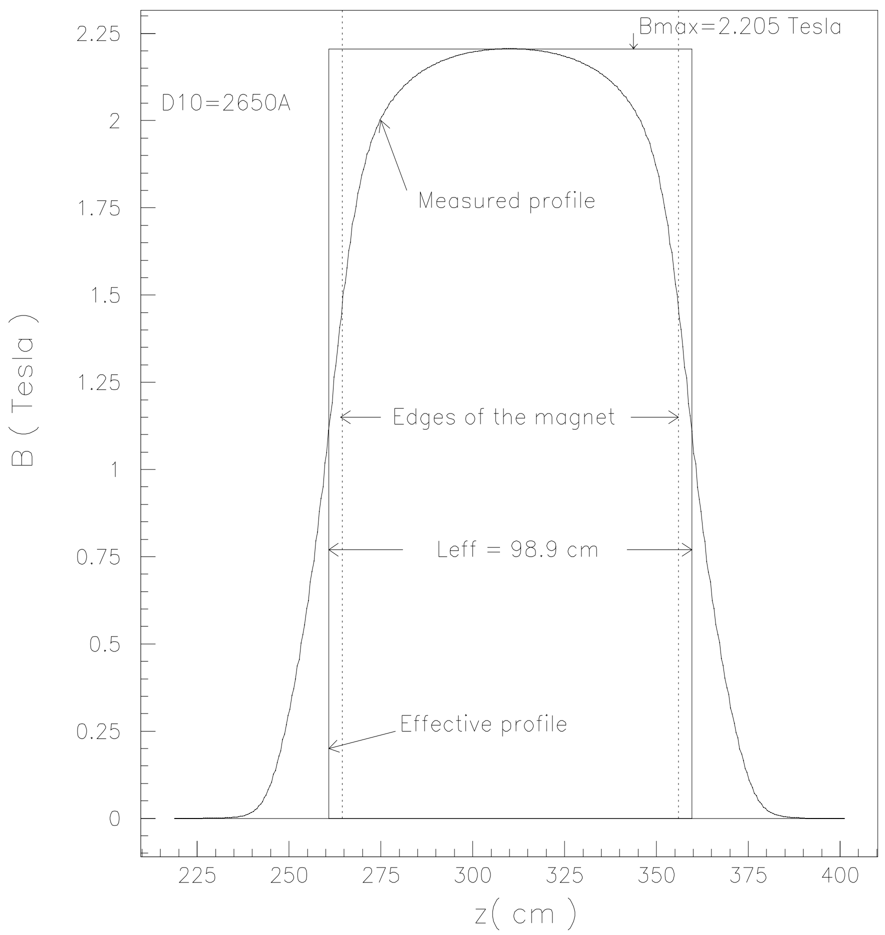

Figure A.2: Measured magnetic field profile and corresponding effective profile for I=2650A.

The shift of the peak in $DCIII$ shown in figure A.1 as a function of wire number with $1.27cm$ spacing corresponds to about $15.14cm$ in the $-x$ direction of the E877 reference frame (figure 3.6). The shift in $DCII$ with $0.64cm$ wire spacing is about $5.40cm$. Knowledge of the beam position for the given field and the distance between drift chambers [4] ($625.70cm$), is sufficient for calculating the deflection angle($\sim 2.0mrad$) . On the other hand, knowledge of the field effective length allows us to calculate the radius of curvature of the beam particle trajectory inside the magnet as

$$R = \frac{L_{eff}}{(sin\theta_{out} - sin\theta_{in})} \tag{A.1}$$

where L_{eff} is the effective length of field, θ_{out} is deflection angle and θ_{in} is the beam incoming angle (measured by $BVER's$) in $x - z$ plane of the beam. Here the effective length L_{eff} is defined by

$$\int_{-\infty}^{\infty} B \cdot dz \equiv B_{max} \cdot L_{eff} \tag{A.2}$$

where B_{max} is a maximum value of magnetic field (see Figure A.2). Finally one can determine the beam momentum using the formula:

$$P \cos\lambda \equiv 0.29979 \cdot \frac{Z}{A_B} \cdot B_{max} \cdot R \tag{A.3}$$

where P is the beam momentum measured in GeV/c, λ is the pitch angle(in $y - z$ plane) of the beam, Z and A_B are the charge and mass numbers of the beam particles respectively, B_{max} is in Tesla and the radius of curvature R is

[4]The measurements of positions for the E877 setup are summarized in Appendix C.

D10 Current(Amperes)	*Beam momentum(GeV/c)*
1750	10.75 ± 0.05
2650	10.84 ± 0.05

Table A.1: Summary of the results obtained by the charge sum of pad cell measurements.

in meters. We assumed that beam particles were fully stripped gold ions with charge number $Z = 79$ and $A_B = 197$; pitch angle λ was considered to be zero. The exact value of λ can be obtained in the current set up only with the help of tracking code. Calculated beam momentum values are summarized in the Table A.2.

The full implementation of E877 tracking code gives results[5] with a better accuracy in momentum determination due to better position resolution. Beam momentum measurements in this case can be done offline during the course of fine tuning the tracking geometrical constants. We obtained values of 10.78 ± 0.3 and 10.74 ± 0.4 GeV/c for $I = 2650$ and $1750A$ respectively. This method depends on the quality of the overall survey. Both methods could not be used without accurate knowledge of the magnetic field strength in $D10$. We prefer the higher field ($I = 2650A$) measurement, because of higher

[5]**This part of the beam momentum determination was performed by B. Hong**

momentum resolution and better quality of the magnetic field measurement. Figure A.3 shows the summary of our results with other known measurements of the AGS gold beam momentum. We conclude that the momentum of the ^{197}Au beam during the 93 AGS heavy ion run was 10.78 ± 0.03 GeV/c per nucleon. This value was about 1 GeV lower than initially advertised by the AGS beam momentum.

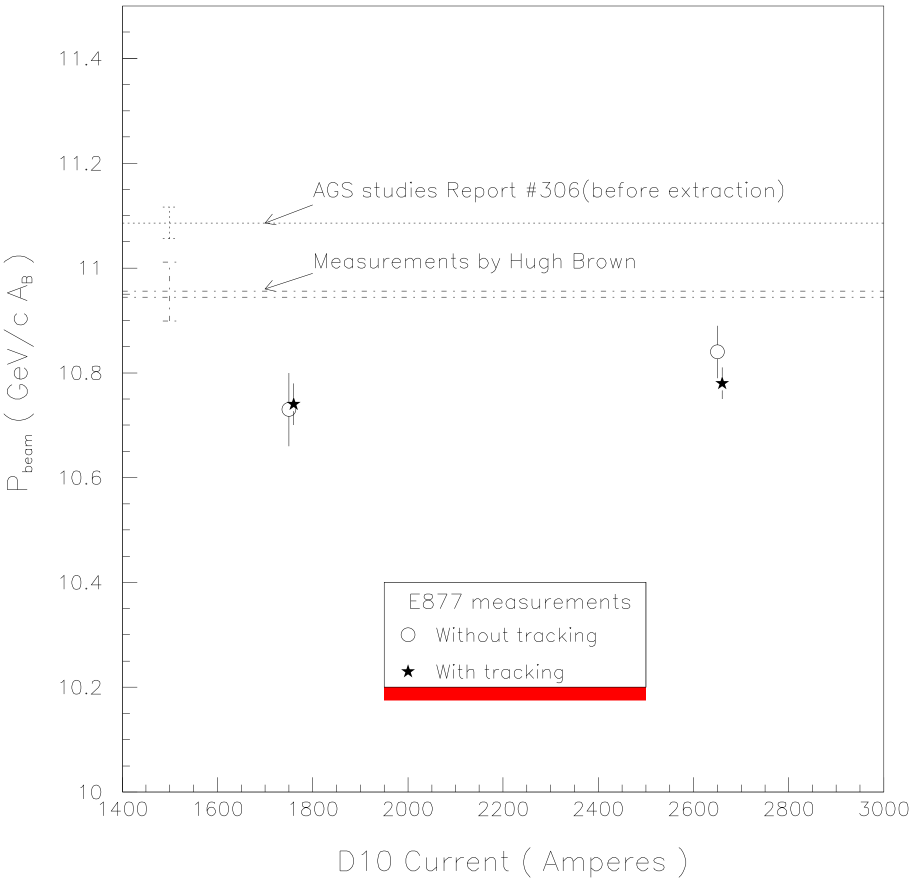

Figure A.3: Known measurements of the AGS gold beam momentum for 1993 run.

Appendix B

Magnet Field Mapping

We[1] performed detailed measurements of the E877 Forward Spectrometer's dipole magnet (also known as $D10$) field in January and February of 1993.

B.1 Setup

A three dimensional magnetic field map was measured with a 3-D teslameter provided by the AGS magnetic field measurement group. Three Hall probes of the order of a millimeter in size were mounted, with a high precision, perpendicular to one another on a movable cart with a level sensor in it. The cart can be moved along a rigid, non-magnetic, rectangular trail by a plastic chain driven by a step motor. The step motor can be remotely controlled via an IBM PC XT. The same PC served as a data acquisition computer, which can read out the three components of the field and the position along the trail

[1] This measurement has been performed together with Y. Zhang.

as well as the pitch and roll angles from the level censor. These angles were used to correct the field components due to the small non-flatness of the trail. Running the data collection program with a given number of steps and step length, a sequence of data points can be written out as the cart moves along the trail. We installed the trail into the opening of $D10$ along the beam direction (z-direction in our convention), and manually set the x, y position of the trail by moving the trail vertically (y-direction) and horizontally (x-direction). By doing so, we obtained the 3-D field measured in the whole inner space of $D10$ as well as the extension outside the magnet in the z-direction.

B.2 Measurement

Limited by the time of the measurement, we choose a set of current setting (including settings utilized in previous heavy-ion runs as well as the maximum current setting) and a proper 3-D grid in mapping. The dimension of the rectangular opening in the magnet was 45.72 $cm\times$ 15.24 $cm\times$ 91.44 cm (18 $inch\times$ 6 $inch\times$ 36 $inch$) in (x, y, z). We measured about 183 cm (72 inch) in the z direction in 1.27 cm (0.5 inch) steps to get the full profile of the field. In x and y direction, however, the acceptance due to the size of the trail limited us to measure only a certain region. Table B.2 shows a list of magnetic fields and positions at which measurements have been performed. Note that we chose the center of the field as zero of the coordinates $(0, 0, 0)$ for the purpose of mapping. The accuracy of our position measurement is about 2 mm. We also measured a hysteresis curve of the magnet. The field was measured at a fixed position

Current(Amperes)	*(x, y) positions (inch)*
B 160	(-3.0,0.0) (-3.0,0.5) (-3.0,1.0) (-3.0,1.5) (-3.0,2.0) (0.0,0.0) (0.0,0.5) (0.0,1.0) (0.0,1.5) (0.0,2.0) (3.0,0.0) (3.0,0.5) (3.0,1.0) (3.0,1.5) (3.0,2.0) (5.0,0.0) (5.0,0.5) (5.0,1.0) (5.0,1.5) (5.0,2.0) (6.0,0.0) (6.0,0.5) (6.0,1.0) (6.0,1.5) (6.0,2.0) (7.0,0.0) (7.0,0.5) (7.0,1.0) (7.0,1.5) (7.0,2.0)
A 285	(-3.0,0.0) (-3.0,0.5) (-3.0,1.0) (0.0,0.0) (0.0,0.5) (0.0,1.0) (0.0,1.5) (0.0,2.0) (1.0,0.0) (1.0,2.0) (2.0,0.0) (2.0,2.0) (3.0,0.0) (3.0,2.0) (4.0,0.0) (4.0,2.0) (5.0,0.0) (5.0,2.0) (6.0,0.0) (6.0,2.0) (7.0,0.0) (7.0,0.5) (7.0,1.0) (7.0,1.5) (7.0,2.0)
B 365	(-3.0,0.0) (-3.0,0.5) (-3.0,1.0) (-3.0,1.5) (-3.0,2.0) (0.0,0.0) (0.0,0.5) (0.0,1.0) (0.0,1.5) (0.0,2.0)
A 475	(-3.0,0.0) (-3.0,2.0) (-2.0,0.0) (-2.0,2.0) (-1.0,0.0) (-1.0,2.0) (0.0,0.0) (0.0,0.5) (0.0,1.0) (0.0,1.5) (0.0,2.0) (1.0,0.0) (1.0,2.0) (2.0,0.0) (2.0,2.0) (3.0,0.0) (3.0,2.0) (4.0,0.0) (4.0,2.0) (5.0,0.0) (5.0,2.0) (6.0,0.0) (6.0,2.0) (7.0,0.0) (7.0,0.5) (7.0,1.0) (7.0,1.5) (7.0,2.0)
B 475	(-3.0,0.0) (-3.0,0.5) (-3.0,1.0) (-3.0,1.5) (-3.0,2.0) (0.0,0.0) (0.0,0.5) (0.0,1.0) (0.0,1.5) (0.0,2.0) (3.0,0.0) (3.0,0.5) (3.0,1.0) (3.0,1.5) (3.0,2.0) (5.0,0.0) (5.0,0.5) (5.0,1.0) (5.0,1.5) (5.0,2.0) (6.0,0.0) (6.0,0.5) (6.0,1.0) (6.0,1.5) (6.0,2.0) (7.0,0.0) (7.0,0.5) (7.0,1.0) (7.0,1.5) (7.0,2.0)
B 800	(0.0,0.0) (0.0,0.5) (0.0,1.0) (0.0,1.5) (0.0,2.0) (7.0,0.0) (7.0,0.5) (7.0,1.0) (7.0,1.5) (7.0,2.0)
B1750	(6.0,0.0) (6.0,0.5) (6.0,1.0) (6.0,1.5) (6.0,2.0) (7.0,0.0) (7.0,0.5) (7.0,1.0) (7.0,1.5) (7.0,2.0)
B2650	(-3.0,0.0) (-3.0,0.5) (-3.0,1.0) (-3.0,1.5) (-3.0,2.0) (0.0,0.0) (0.0,0.5) (0.0,1.0) (0.0,1.5) (0.0,2.0) (3.0,0.0) (3.0,0.5) (3.0,1.0) (3.0,1.5) (3.0,2.0) (5.0,0.0) (5.0,0.5) (5.0,1.0) (5.0,1.5) (5.0,2.0) (6.0,0.0) (6.0,0.5) (6.0,1.0) (6.0,1.5) (6.0,2.0) (7.0,0.0) (7.0,0.5) (7.0,1.0) (7.0,1.5) (7.0,2.0)

Table B.1: Summary of Magnetic Field Measurements for Different Current Setting and (x, y) Positions.

$(7,0,0)$, while the current was changing from zero to the maximum value and back. The measurements corresponding to a decreasing current served as the reference. Whenever we changed the current, we would wait at least 3 minutes for the field to be stabilized. No statistically significant difference between the two polarities of the field has been observed. Table B.2 presents the results of the hysteresis measurements. To get an idea of the accuracy of our field strength measurement and the systematic uncertainty, we measured the field strength at position $(7,0,0)$ for current $I = 475A$ at the beginning and the end of each day (we called it calibration runs) which, averaged over about two weeks period, gave B $= 4360.0 \pm 4.0$ Gauss. The relative error of 0.1% reflects the systematic uncertainty that should be applicable to other field settings, note the accuracy of the Hall probe itself is much better then that, only about 0.02%.

B.3 Results

The raw data were corrected for the pitch and roll angles, and are also corrected with the calibration mentioned above. Data in the regions unaccessible for the direct measurements were obtained by either mirroring of, or extrapolating from, the measured region.

From the measurement of the hysteresis curve, we find that the difference between increasing or decreasing the current does not yield a significant difference in field strength. The $B\ vs\ I$ curve starts to deviate from the straight line at about $I = 1500A$, which is the starting point of the saturation of the mag-

$I(Amperes)$	$B_y^{increasing}(Gauss)$	$B_y^{decreasing}(Gauss)$
100	926.0	932.5
200	1837.0	1846.5
300	2751.0	2764.0
400	3665.0	3679.0
500	4584.0	4598.0
600	5498.0	5512.0
700	6414.5	6428.0
800	7328.0	7344.0
900	8240.5	8259.0
1000	9152.0	9176.0
1100	10065.5	10087.5
1200	10974.5	10999.0
1300	11877.5	11906.0
1400	12777.5	12812.5
1500	13676.5	13711.5
1600	14562.5	14602.0
1700	15440.0	15480.0
1800	16286.0	16328.5
1900	17105.0	17143.5
2000	17890.5	17925.5
2100	18637.5	18671.0
2200	19352.0	19379.5
2300	20032.0	20054.5
2400	20674.5	20690.0
2500	21273.0	21283.0
2600	21807.5	21810.5
2650	22051.0	22051.0

Table B.2: Current(I) and Field(B_y) at Position $(7, 0, 0)$.

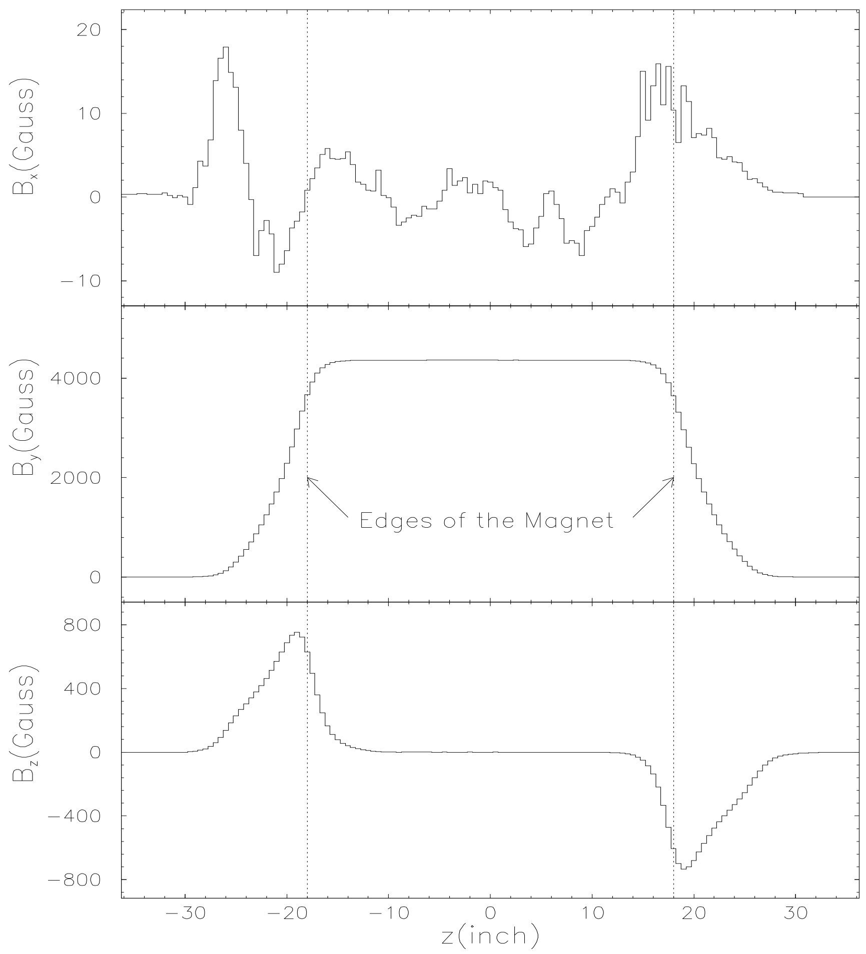

Figure B.1: B_x, B_y and B_z of magnetic field strength for $I = 475A$ as a function of z at $(x, y) = (7, 1)$.

net. Figure B.1 shows x, y, z components of the field strength for $I = 475A$ as a function of z at $(x, y) = (7, 1)$. $\boldsymbol{B_x}$ and $\boldsymbol{B_z}$ are small compared to $\boldsymbol{B_y}$, which is the main component of the field. $\boldsymbol{B_y}$ is quite flat in the middle of the field over a large range for $I \leq 1500A$. Figure A.2 presents $\boldsymbol{B_y}$ vs z for the full field setting ($I = 2650A$). Now $\boldsymbol{B_y}$ is flat only over a small range, in the middle of the magnet. This implies that we may scale the 3-D field profiles for $I \leq 1500A$, while for higher field it is not justified , and each current setting has to be measured individually.

Appendix C

The E877 geometry

In this section we present the survey of the E877 geometry. It was done by the Stony Brook group during the run of 1993.

Upstream Group of Deterctors			
Detector	$z(mm)$	$x(mm)$	$y(mm)$
$S2$	-6274.	–	–
$BVER1$	-5856.	–	–
$BVER2$	-2799.	–	–
$S4$	-2003.	–	–
$Target$	0.	–	–

$PCAL$ – Collimator (closed)			
Detector	$z(mm)$	$x(mm)$	$y(mm)$
$USLL$	733.7	11.6	-7.2
$USLU$	733.7	11.6	8.9
$USRL$	733.7	-97.7	-6.8
$USLL$	733.7	-97.7	9.2
$DSLL$	825.0	196.9	-16.5
$DSLU$	825.0	196.9	16.8
$DSRL$	825.0	-23.3	-15.4
$DSLL$	825.0	-23.3	17.8

- first two letters - US: upstream, DS: downstream
- third letter - L: beamleft, R: beamright
- fourth letter - L: lower edge, U: upper edge with respect to the beam.

Forward Spectrometer			
Detector	$z(mm)$	$x(mm)$	$y(mm)$
$D8(center)$	3098.8	-177.8	–
$DCII$	5400.0	–	–
$MWPC1$	6632.6	-807.7	–
$MWPC2$	7840.6	-960.1	–
$MWPC3$	9086.9	-1112.5	–
$MWPC4$	10317.2	-1264.9	–
$DCIII$	11545.9	–	–

- The z position of $DCII$ is from the target to the downstream face of detector while that of the $MWPC's$ and $DCIII$ is from the target to the upstream face of detector.
- The x positions of the $MWPC's$ refer to the position of the first wire in the chamber. The wire-spacing is 5.08 mm.

Appendix D

Beam Scintillators Slewing Correction

We will discuss the approach to slewing correction of the beam scintillators used by Stony Brook group during analysis of Au+Au data obtained by E877 collaboration in 1994. The procedure of obtaining slewing correction for *all* BSCI phototubes is described. It is shown that this method allows us to obtain the intrinsic resolution between any pair of phototubes of the order of 50 *ps* or better.

D.1 BSCI setup for the 93 and 94 runs

Details of hardware and the usage of BSCI information for event selection were described earlier in chapter, 4. In this section we will concentrate on the discussion of the procedure of obtaining a proper start time reference for the rest of the detector subsystems. The structural scheme of the E877 experiment time of flight system is presented in Figure D.1. T21,T22,T41 and T42 represent signals coming from phototubes attached to BSCI2 and BSCI4.

The Beam logic module generates the beam particle definition signal, using information from all BSCI detectors (including BSCI1 and BSCI3). The CAMAC TDC is model 2228A with a time resolution of 50 ps. Five FASTBUS LeCroy TDC modules 1875A are used to digitize signals from the Time of Flight Upstream (TOFU) System, which consists of 160 scintillator (Bicron BC404) slats, each equipped with two Hamamatsu R3478 phototubes. Each TDC module has 64 channels with a resolution of 25 ps. More detailed description of the LeCroy TDC modules can be found in [54]. In the 1994 setup the signals from BSCI41 were used as a start signal of TDC.

D.2 Slewing Correction. The General Approach

In order to provide a proper time signal one should perform a so called slewing correction for each time channel. In brief, slewing is a correlation between the amplitude of the signal and time. A typical picture of the slewing effect is depicted on Figure D.2. We show there a measurement made by a CAMAC TDC module which was used during the run for the on-line monitoring of the BSCI system performance. One can see that the phototube BSCI41 does not show any slewing dependence. This is is due to the fact that a signal from this tube was used as a start up signal for all TDC modules in E877 time of flight system during 1994 run.

We would like to spent some time on a brief discussion of this evidently simple but often overlooked fact: What a common start TDC module is actually measuring is a time interval between the start signal (BSCI41 in our case)

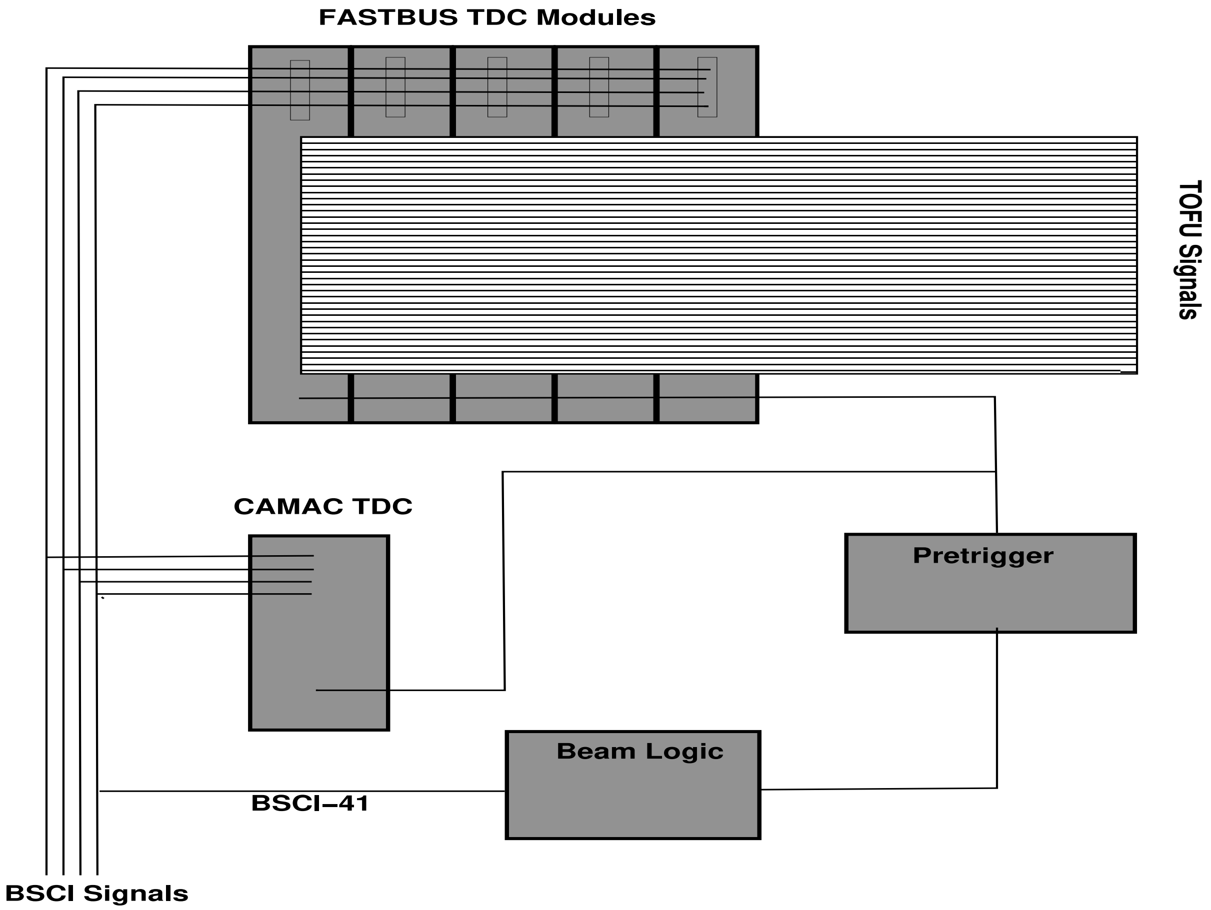

Figure D.1: Structural scheme of the BSCI timing setup. See description in the text.

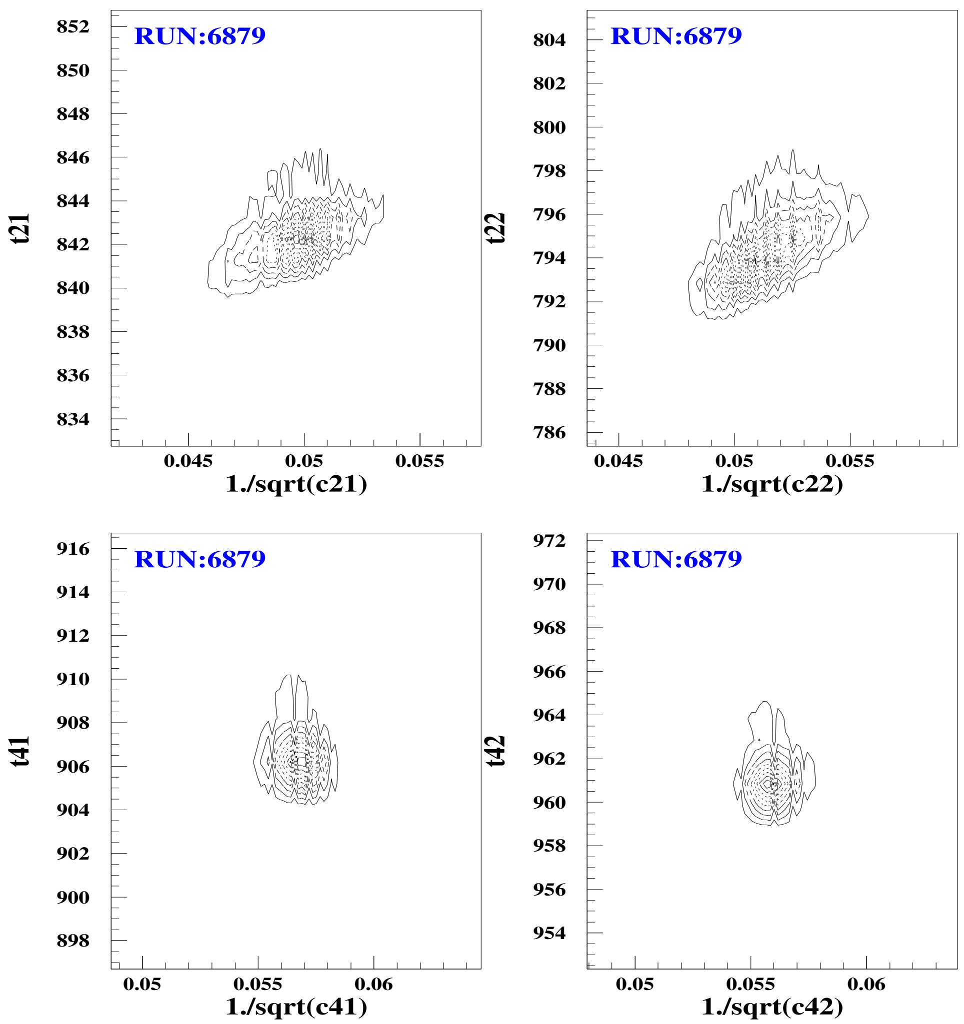

Figure D.2: Example of the slewing effect in the BSCI phototubes. CAMAC TDC measurement is shown. See description in the text.

and the arrival of the properly delayed input(stop) signals (from all BSCIs). It is clear that any slew dependence of the BSCI41 signal should be invisible in the described setup. That does not mean, of course, that this particular tube has no slewing, it just can not be measured this way.

Figure D.3 shows the correlation between position[1] of the beam particle hit and time of the detected signal from BSCI. Again, one can see there that BSCI41 signal doesn't exhibit any hit position dependence. An additional disadvantage is that slewing and position (and any other) dependencies of the start up signal enter, in an indirect way, into the time measurement of all other TDC input signals.

We will describe in a following sections a routine that involves a simultaneous slewing correction of any pair of BSCI phototubes. We will show that this method allows to obtain slewing constants for all tubes *including BSCI41* and eliminates a need for an additional position dependence correction of BSCI signals.

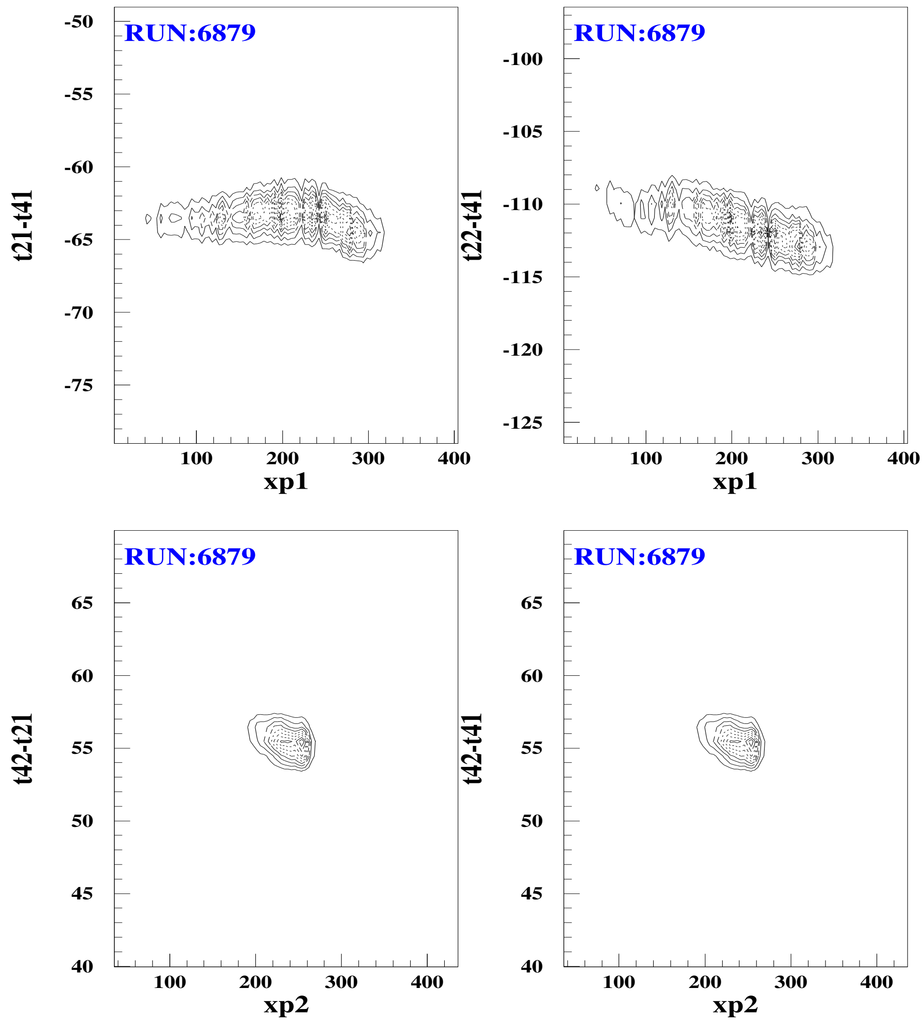

Figure D.3: X-dependence of the BSCI time. xp1 and xp2 mean an x position of the beam particle hit in BSCI2 and BSCI4 respectively. CAMAC TDC measurement is shown. See description in the text.

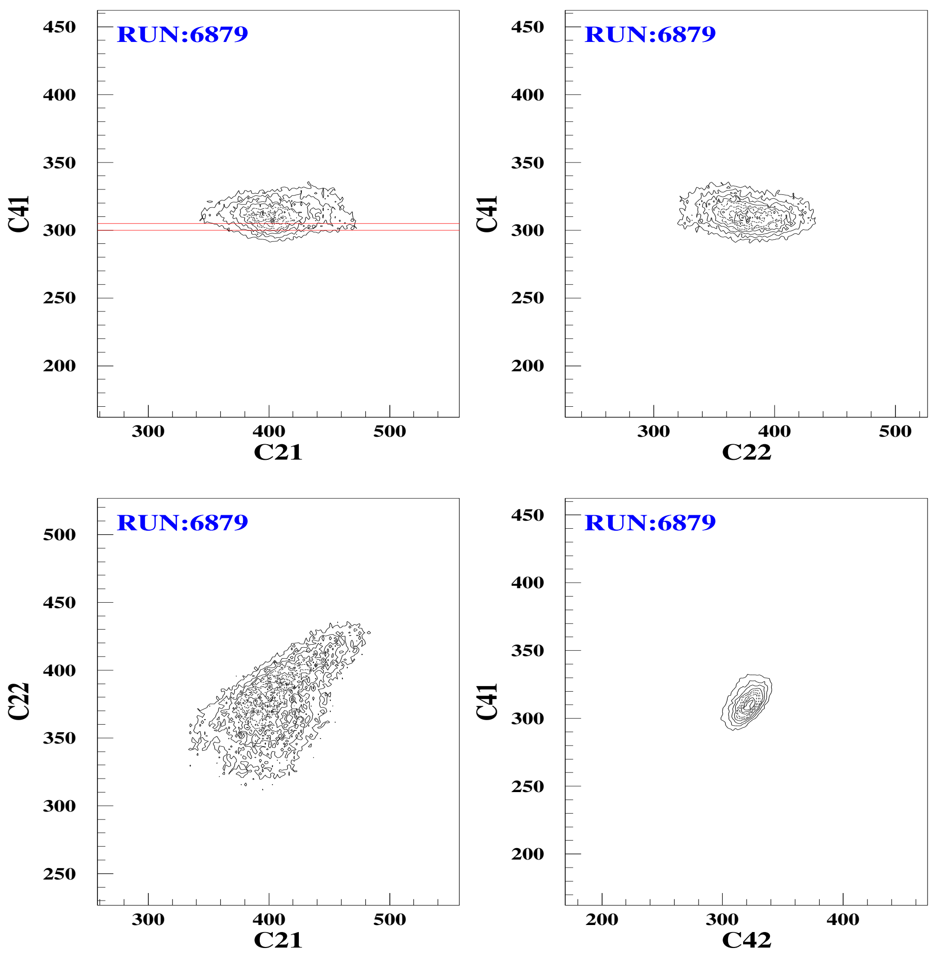

Figure D.4: Correlation between amplitudes of the signals from different phototubes.

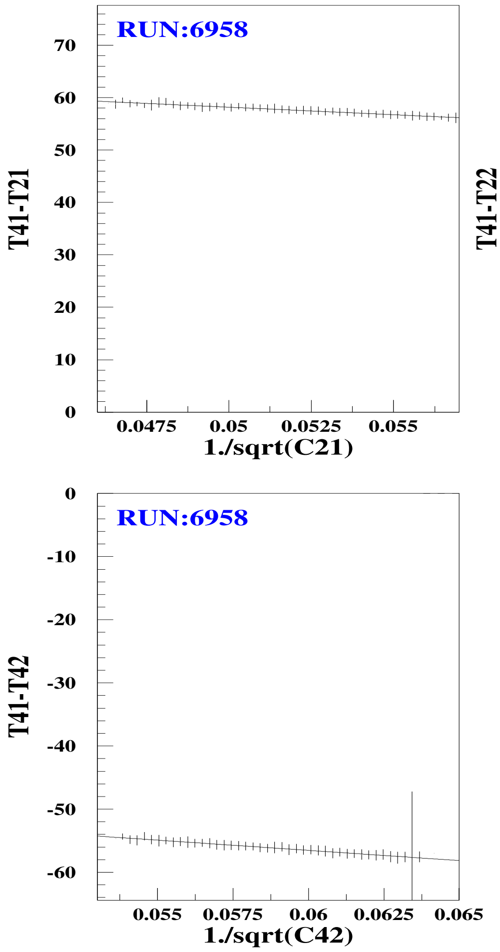

Figure D.5: Slewing dependence in a time difference between two tubes, with BSCI41 as a reference tube.

D.3 Analysis Procedure for Slewing Correction

As we said before, the described procedure involves a pair of phototubes. By taking a difference of two tube time signals one obviously eliminates the influence of the TDC start signal variations. Electronics jitters and slewing dependencies of each signal will contribute to the width of the time difference variable. One can suppress or diminish the influence of one of the tube's slewing by making a cut on the amplitude of that tube. As an example we will demonstrate here a procedure which involved BSCI41 as a reference tube. Figure D.4 shows a cut used during correction of the BSCI41 and BSCI21 pair. One can see that cutting on a narrow BSCI41 pulse amplitude covers a sufficiently large interval of the BSCI21 dynamic range. After fixing the amplitude of the "reference" tube one can clearly see , for example on the upper left panel of the Figure D.5, a characteristic linear dependence of the BSCI41-BSCI21 variable as a function of the $1./\sqrt{C21}$. This is due to the slewing effect of BSCI21. Other tubes show a similar behavior. Fitting of this linear dependence gives slewing constants for these tubes. This correction can be used now in determination of the BSCI41 slewing dependence. Figure D.6 shows the difference between BSCI41 and BSCI21, after BSCI21 was slewing

---

[1] X-position of the hit can be determined from the information provided by beam vertex detectors (BVER). See description earlier in this chapter

corrected, as a function of the $1./\sqrt{C41}$ [2] of BSCI41. Again, one can see a clear linear slewing dependence as in Figure D.5. We would like to repeat that this slewing dependence of the signal from BSCI41 is masked in a single tube approach because of the fact that BSCI41 was used as a start up signal for the TDC. The linear fit of the dependence on Figure D.6 gives slewing constants for BSCI41. Note that by performing the procedure outlined above for all combinations with BSCI41 as a reference tube one will obtain 3 independent sets of slewing constants for BSCI41. Table D.3 shows slewing constants for BSCI phototubes determined for the run number 6879. This run was chosen because it was taped a few hours after new beam scintillators were installed [3] and high voltages on the phototubes were adjusted. All three set of constants for BSCI41 agree within errors.

Figure D.7 presents a time resolution between some combination of pairs of phototubes for the CAMAC TDC module. As we mentioned before the resolution of this TDC is 50 ps. One can see that our method provides resolution on the order of 50 ps (one channel of the histograms on Figure D.7) or better. An additional benefit of the described procedure is shown on Figure D.8. One can see, on the upper panel, a dependence of the difference of the

---

[2] Note that there is no narrow cut on BSCI41 amplitude, shown on Figure D.4, in this case. Both tubes were subjected to the cuts aimed to suppress noise and double beam events which are not relevant to the topic of this note.

[3] Hence we can avoid,while dealing with this run, complications related to radiation damages of the scintillators, which we will discuss later.

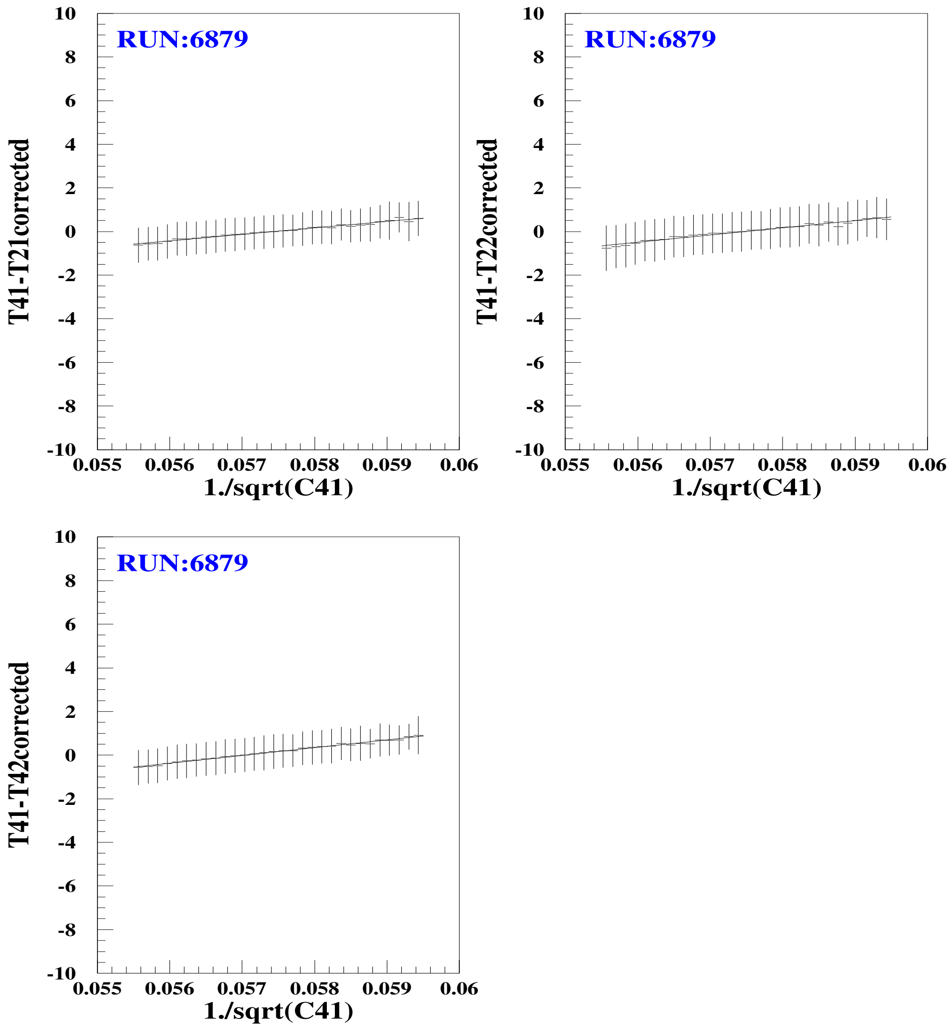

Figure D.6: Slewing dependence in BSCI41 after all other tubes were slewing corrected.

Table D.1: Slewing constants for different phototubes. Linear dependence y=ax+b was assumed. Note that the difference in signs of the slewing coefficients **a** of BSCI41 from the others is a trivial artifact of the presented method, due to the choice of the correction function and can be safely disregarded. All coefficients **a** should have the same sign.

Phototube	*a*	*b*
BSCI21	-404±31	84.4±1.6
BSCI22	-497±29	137.5±1.5
BSCI42	-401±36	-32.4±2.1
BSCI41 from BSCI21	301.7±38.6	-17.3±2.2
BSCI41 from BSCI22	353.2±47.0	-20.2±2.3
BSCI41 from BSCI42	356.8±39.1	-20.3±2.2

time signals on the x-position of the beam particle in BSCI2 scintillator. This dependence is totally absent on the lower panel, in which both time signals were slew corrected.

D.4 Stability of the Slewing Constants

It is important to show that the slewing correction consistently provides two tube resolution over the time interval relevant to our discussion. Figure D.9 shows time difference between slewing corrected BSCI21 and BSCI41 for several runs, which cover a period of about four weeks. Note the shift in the absolute values of the time differences between two tubes. This is mostly due to the changes in high voltages of the phototubes applied during the run in order to compensate for a gradual degradation of the beam scintillator's light output caused by radiation damages. As one can see despite these shifts the two tube resolution remains fairly stable.

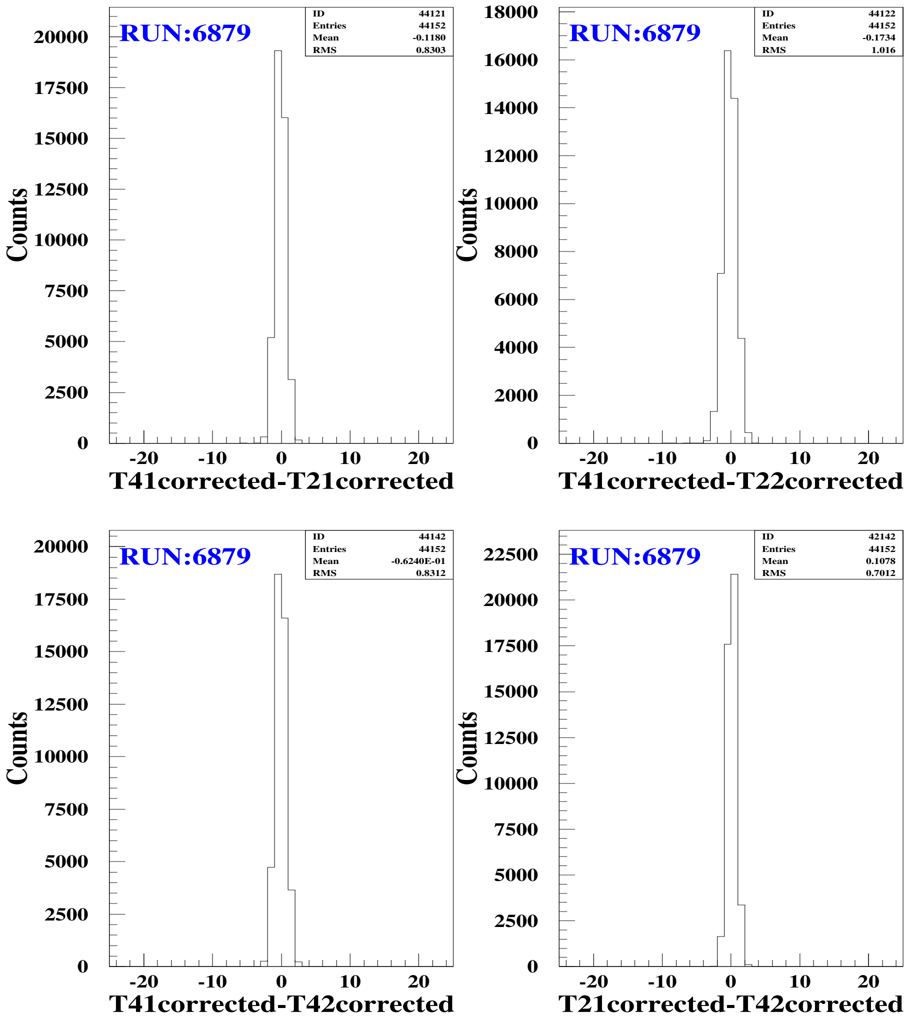

Figure D.7: Time resolution between pairs of phototubes after both tubes were slewing corrected.

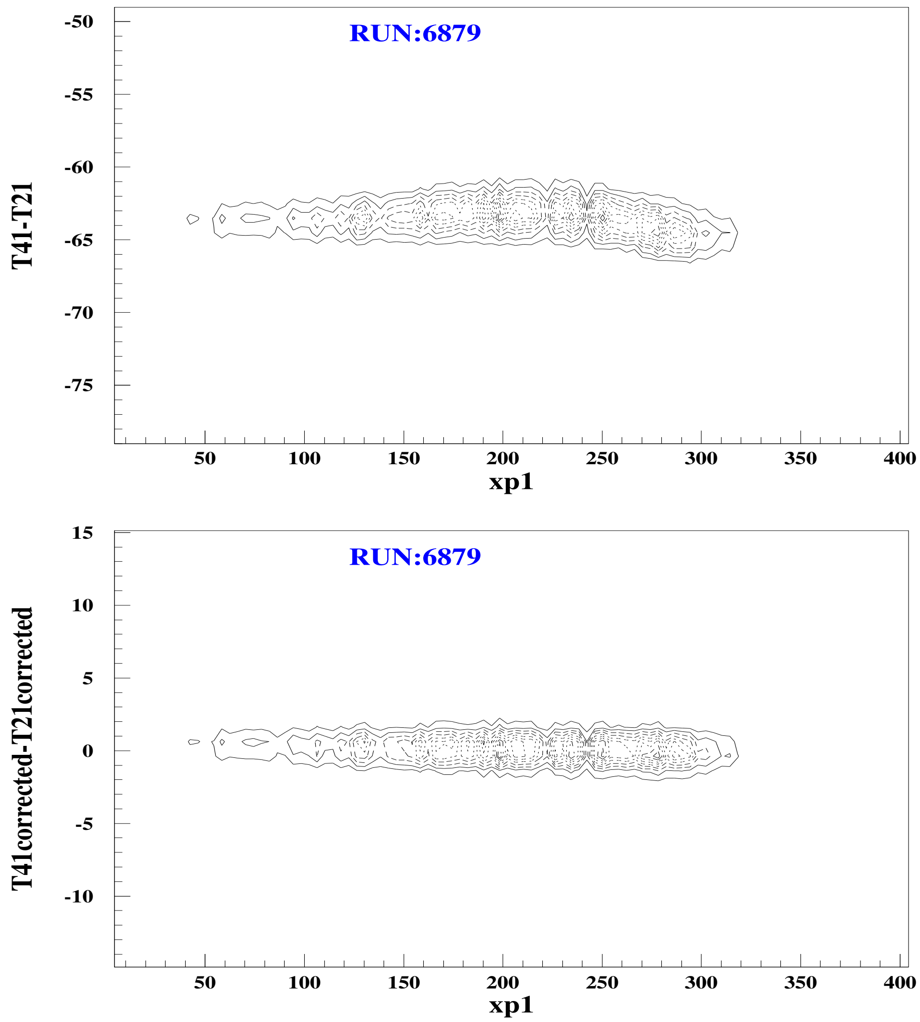

Figure D.8: Position dependence of the time difference of the tubes before (upper panel) and after (lower panel) tubes were slewing corrected.See description in the text.

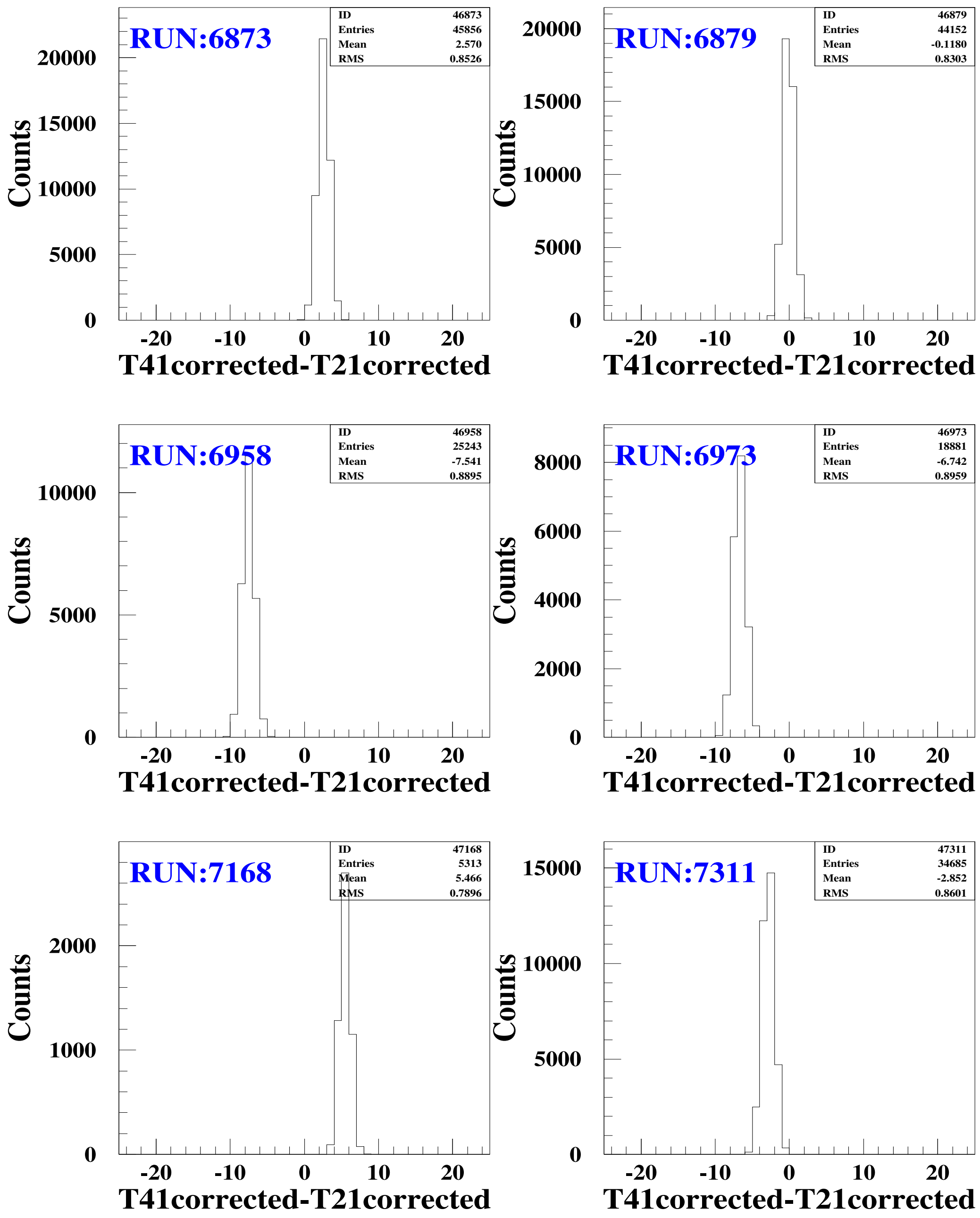

Figure D.9: Two tube resolution between BSCI21 and BSCI41 for different runs.

Appendix E

Invariant Relative Momentum Resolution

A straightforward algebraic exercise has been performed in order to determine the analytical form of the two-particle relative momentum resolution. The expression for resolution in q_{inv} as a function of particle momenta and opening angle was obtained using a linear approximation. A similar approach was applied to the case of nonidentical particles. Calculations were carried out with the help of the MAPLE Symbolic Mathematical Package.

E.1 Identical particles

Let's first take a case of identical particles. We will use the following set of variables: $p1, p2$ -momenta of pair's particle, m - particle mass, θ -angle between two particles' momenta. Let q_{inv} be an absolute value of 4-momentum difference of the pair[1]. With the convention for 4-momentum vector $P = (E, \vec{p})$ we have for identical particles,

$$q_{inv}^2 = (P1 - P2)^2 = 2\,\left(m^2 - \sqrt{m^2 + p1^2}\,\sqrt{m^2 + p2^2} + p1\,p2\,\cos\theta\right) \quad \text{(E.1)}$$

$$q_{inv} = \sqrt{|q_{inv}^2|}. \quad \text{(E.2)}$$

It's clear that

$$\frac{\partial q_{inv}}{\partial x_i} = \frac{1}{2}\frac{1}{\sqrt{q_{inv}^2}}\frac{\partial q_{inv}^2}{\partial x_i} = \frac{1}{2q_{inv}}\frac{\partial q_{inv}^2}{\partial x_i} \quad \text{(E.3)}$$

where x_i is $p1, p2$ or θ .

It's trivial to get partial derivatives for q_{inv}^2:

$$\frac{\partial q_{inv}^2}{\partial p1} = 2\,\left(-\frac{p1\,\sqrt{m^2 + p2^2}}{\sqrt{m^2 + p1^2}} + p2\,\cos(\theta)\right) \quad \text{(E.4)}$$

$$\frac{\partial q_{inv}^2}{\partial p2} = 2\,\left(-\frac{p2\,\sqrt{m^2 + p1^2}}{\sqrt{m^2 + p2^2}} + p1\,\cos(\theta)\right) \quad \text{(E.5)}$$

$$\frac{\partial q_{inv}^2}{\partial \theta} = -2\,p1\,p2\,\sin(\theta). \quad \text{(E.6)}$$

---

[1]Note that for purely historical reasons usual E814/E877 variable used in two-proton analysis is $q_{inv}^{pp} = q_{inv}/2$

Hence

$$\frac{\partial q_{inv}}{\partial p1} = \frac{1}{q_{inv}} \left(-\frac{p1\, \sqrt{m^2 + p2^2}}{\sqrt{m^2 + p1^2}} + p2\, \cos(\theta) \right) \tag{E.7}$$

$$\frac{\partial q_{inv}}{\partial p2} = \frac{1}{q_{inv}} \left(-\frac{p2\, \sqrt{m^2 + p1^2}}{\sqrt{m^2 + p2^2}} + p1\, \cos(\theta) \right) \tag{E.8}$$

$$\frac{\partial q_{inv}}{\partial \theta} = -\frac{1}{q_{inv}}\, p1\, p2\, \sin(\theta). \tag{E.9}$$

In a linear approximation the dispersion of q_{inv} can be defined as

$$D(q_{inv}) \approx \sum_{i=1}^{3} \left(\frac{\partial q_{inv}}{\partial x_i} \right)^2 \sigma^2(x_i) + 2 \sum_{i<j} \left(\frac{\partial q_{inv}}{\partial x_i} \right) \left(\frac{\partial q_{inv}}{\partial x_j} \right) \rho_{ij} \sigma(x_i) \sigma(x_j) \tag{E.10}$$

where $\sigma(x_i)$ is a standard deviation of a respective variable (momentum or angle in this case) and ρ_{ij} - is the correlation coefficient between variables x_i and x_j . Standard deviation of q_{inv} by definition is

$$\sigma(q_{inv}) = \sqrt{D(q_{inv})}. \tag{E.11}$$

E.2 Non-identical particles

One can easily expand this formalism to the case of non-identical particles. Lets assume that we know 4-momenta of both particles: $P1 = (E1, \vec{p1})$,

$P2 = (E2, \vec{p2})$. Also $E = \sqrt{P^2 + m^2}$. We will use notation $\vec{p1} = (p1x, p1y, p1z)$ and $\vec{p2} = (p2x, p2y, p2z)$ Then q_{inv} can be expressed as:

$$q_{inv} = \Big(m1^2 - 2\sqrt{p1x^2 + p1y^2 + p1z^2 + m1^2}\sqrt{p2x^2 + p2y^2 + p2z^2 + m2^2} + m2^2 \\ + 2\,p1x\,p2x + 2\,p1y\,p2y + 2\,p1z\,p2z\Big)^{1/2}$$

Partial derivatives are:

$$\frac{\partial q_{inv}}{\partial p1x} = -\sqrt{p2x^2 + p2y^2 + p2z^2 + m2^2}\,p1x \Big/ \Big(\Big(m1^2 \\ - 2\sqrt{p1x^2 + p1y^2 + p1z^2 + m1^2}\sqrt{p2x^2 + p2y^2 + p2z^2 + m2^2} + m2^2 \\ + 2\,p1x\,p2x + 2\,p1y\,p2y + 2\,p1z\,p2z\Big)^{1/2} \\ \sqrt{p1x^2 + p1y^2 + p1z^2 + m1^2}\Big) + p2x \Big/ \Big(m1^2 \\ - 2\sqrt{p1x^2 + p1y^2 + p1z^2 + m1^2}\sqrt{p2x^2 + p2y^2 + p2z^2 + m2^2} + m2^2 \\ + 2\,p1x\,p2x + 2\,p1y\,p2y + 2\,p1z\,p2z\Big)^{1/2}$$

$$\frac{\partial q_{inv}}{\partial p1y} = -\sqrt{p2x^2 + p2y^2 + p2z^2 + m2^2}\,p1y \Big/ \Big(\Big(m1^2 \\ - 2\sqrt{p1x^2 + p1y^2 + p1z^2 + m1^2}\sqrt{p2x^2 + p2y^2 + p2z^2 + m2^2} + m2^2 \\ + 2\,p1x\,p2x + 2\,p1y\,p2y + 2\,p1z\,p2z\Big)^{1/2} \\ \sqrt{p1x^2 + p1y^2 + p1z^2 + m1^2}\Big) + p2y \Big/ \Big(m1^2 \\ - 2\sqrt{p1x^2 + p1y^2 + p1z^2 + m1^2}\sqrt{p2x^2 + p2y^2 + p2z^2 + m2^2} + m2^2 \\ + 2\,p1x\,p2x + 2\,p1y\,p2y + 2\,p1z\,p2z\Big)^{1/2}$$

$$
\begin{aligned}
\frac{\partial q_{inv}}{\partial p1z} = {} & -\sqrt{p2x^2 + p2y^2 + p2z^2 + m2^2}\, p1z \Big/ \Big(\Big(m1^2 \\
& - 2\sqrt{p1x^2 + p1y^2 + p1z^2 + m1^2}\sqrt{p2x^2 + p2y^2 + p2z^2 + m2^2} + m2^2 \\
& + 2\, p1x\, p2x + 2\, p1y\, p2y + 2\, p1z\, p2z\Big)^{1/2} \\
& \sqrt{p1x^2 + p1y^2 + p1z^2 + m1^2}\Big) + p2z \Big/ \Big(m1^2 \\
& - 2\sqrt{p1x^2 + p1y^2 + p1z^2 + m1^2}\sqrt{p2x^2 + p2y^2 + p2z^2 + m2^2} + m2^2 \\
& + 2\, p1x\, p2x + 2\, p1y\, p2y + 2\, p1z\, p2z\Big)^{1/2}
\end{aligned}
$$

$$
\begin{aligned}
\frac{\partial q_{inv}}{\partial p2x} = {} & -\sqrt{p1x^2 + p1y^2 + p1z^2 + m1^2}\, p2x \Big/ \Big(\Big(m1^2 \\
& - 2\sqrt{p1x^2 + p1y^2 + p1z^2 + m1^2}\sqrt{p2x^2 + p2y^2 + p2z^2 + m2^2} + m2^2 \\
& + 2\, p1x\, p2x + 2\, p1y\, p2y + 2\, p1z\, p2z\Big)^{1/2} \\
& \sqrt{p2x^2 + p2y^2 + p2z^2 + m2^2}\Big) + p1x \Big/ \Big(m1^2 \\
& - 2\sqrt{p1x^2 + p1y^2 + p1z^2 + m1^2}\sqrt{p2x^2 + p2y^2 + p2z^2 + m2^2} + m2^2 \\
& + 2\, p1x\, p2x + 2\, p1y\, p2y + 2\, p1z\, p2z\Big)^{1/2}
\end{aligned}
$$

$$
\begin{aligned}
\frac{\partial q_{inv}}{\partial p2y} = {} & -\sqrt{p1x^2 + p1y^2 + p1z^2 + m1^2}\, p2y \Big/ \Big(\Big(m1^2 \\
& - 2\sqrt{p1x^2 + p1y^2 + p1z^2 + m1^2}\sqrt{p2x^2 + p2y^2 + p2z^2 + m2^2} + m2^2 \\
& + 2\, p1x\, p2x + 2\, p1y\, p2y + 2\, p1z\, p2z\Big)^{1/2} \\
& \sqrt{p2x^2 + p2y^2 + p2z^2 + m2^2}\Big) + p1y \Big/ \Big(m1^2 \\
& - 2\sqrt{p1x^2 + p1y^2 + p1z^2 + m1^2}\sqrt{p2x^2 + p2y^2 + p2z^2 + m2^2} + m2^2
\end{aligned}
$$

$$+ 2\, p1x\, p2x + 2\, p1y\, p2y + 2\, p1z\, p2z\Big)^{1/2}$$

$$\frac{\partial q_{inv}}{\partial p2z} = -\sqrt{p1x^2 + p1y^2 + p1z^2 + m1^2}\, p2z \Big/ \Big(\Big(m1^2 - 2\sqrt{p1x^2 + p1y^2 + p1z^2 + m1^2}\sqrt{p2x^2 + p2y^2 + p2z^2 + m2^2} + m2^2 + 2\, p1x\, p2x + 2\, p1y\, p2y + 2\, p1z\, p2z\Big)^{1/2} \sqrt{p2x^2 + p2y^2 + p2z^2 + m2^2}\Big) + p1z \Big/ \Big(m1^2 - 2\sqrt{p1x^2 + p1y^2 + p1z^2 + m1^2}\sqrt{p2x^2 + p2y^2 + p2z^2 + m2^2} + m2^2 + 2\, p1x\, p2x + 2\, p1y\, p2y + 2\, p1z\, p2z\Big)^{1/2}$$

At this point we are ready to use formula E.11 provided that we know the covariance matrix of $\vec{p1}$ and $\vec{p2}$.

Appendix F

The Contribution from Hyperons

Weak decays of strange baryons can, in principle, lead to distortions in the proton correlation function. Because of the long lifetimes and significant fraction of their decays into the proton channel the lightest hyperons (Λs, Σ^+s) can contribute to the so called "core-halo" structure of the proton source. Subsequently, the two scales in the source function may lead to distortions of the correlation function and should be taken into account during interpretation of the data. Hence it is interesting to estimate the fraction of protons from the hyperons and the possible influence of hyperon decays on our measured correlation function. Table F shows some parameters of hyperon decays which can potentially contribute to the overall number of detected protons. Also the average yields per event, according to RQMD-1.08, is shown in the table. It can be seen from the table that feeding from all possible hyperon channels (we actually neglected Ω^- because of it's small production cross section at the AGS energies) gives about 20 Λs per event, which will decay into about 12.8 protons; Σ^+-hyperon decays will contribute about 2 protons. Based on

Particle	Num./event	Decay properties			
		Mode	Fraction	Momentum, MeV/c	$c\tau$ cm
Λ	14.0	$\Lambda \rightarrow p + \pi^-$	64.2%	100	7.89
Σ^+	4.1	$\Sigma^+ \rightarrow p + \pi^0$	51.64%	189	2.40
Σ^0	4.1	$\Sigma^0 \rightarrow \Lambda + \gamma$	100%	74	1.7×10^{-9}
Ξ^-	1.1	$\Xi^- \rightarrow \Lambda + \pi^-$	100%	139	4.92
Ξ^0	1.1	$\Xi^0 \rightarrow \Lambda + \pi^0$	100%	135	8.69
p	170.7	-	-	-	-

Table F.1: Some of the decay properties of hyperons (data from PDG 1994) and average number per event for Au+Au events with centrality less then 10%, at P=10.8 AGeV/c as predicted by RQMD 1.08. The total number of protons at freeze-out is listed at the bottom.

the RQMD numbers, one would expect 15 protons to be produced from all relevant hyperon channels (what one might call "halo" protons) and about 171 protons from the "core" of the collision.

F.0.1 Back of the Envelope Estimate

We will try to calculate the efficiency for detection of protons originating from hyperon decays by the E877 spectrometer in Au+Au central collisions at about 11 AGeV/c. The average number of reconstructed protons in the E877 spectrometer after all cuts is about 1.6 for centralities less then 10%. Which, given the total number of protons after the freeze-out $171 + 15 = 186$, yields the efficiency for proton detection of about 0.0086.

We will assume that, to first order, rapidity and transverse momentum distributions of Λ-hyperons are similar to the direct proton distributions. Due to the small decay momentum of the Λ-hyperon ($\sim$100 MeV/c) the rapidity distribution of protons originating from the decays will be similar to the rapidity distribution of mother particles. Thus we can approximate the shape of the rapidity distribution of protons from lambda decay as the same as that of direct protons such that the efficiency of detection is the same. This leads us to the average number of protons from Λ-hyperon decay, detected in the E877 acceptance, reconstructed and passed all track cuts, to be approximately $15\times 8.6\times 10^{-3} = 0.13$ per event. Which gives us an estimate of the fraction of the "halo" protons in the total number of the detected protons to be of the order of 8%. Note that the assumption of the similarity of the rapidity distribution of “core” and “halo” protons, as well as the assumption of similar detection efficiency, gives the upper limit for this estimate. One would expect that the real rapidity distribution of Λs is somewhat narrower that of the protons, suggesting that we can neglect hyperons’ contribution to to the total yield of protons and their influence on the correlation function.

The GEANT calculation [53] using the phase space distribution of Λ s from RQMD1.08 gave the fraction of reconstructed protons from Λ decays from 3% to 1% for different rapidity intervals. Which does not contradict our upper limit estimate.